

INFORMATION TO USERS

This manuscript has been reproduced from the microfilm master. UMI films the text directly from the original or copy submitted. Thus, some thesis and dissertation copies are in typewriter face, while others may be from any type of computer printer.

The quality of this reproduction is dependent upon the quality of the copy submitted. Broken or indistinct print, colored or poor quality illustrations and photographs, print bleedthrough, substandard margins, and improper alignment can adversely affect reproduction.

In the unlikely event that the author did not send UMI a complete manuscript and there are missing pages, these will be noted. Also, if unauthorized copyright material had to be removed, a note will indicate the deletion.

Oversize materials (e.g., maps, drawings, charts) are reproduced by sectioning the original, beginning at the upper left-hand corner and continuing from left to right in equal sections with small overlaps. Each original is also photographed in one exposure and is included in reduced form at the back of the book.

Photographs included in the original manuscript have been reproduced xerographically in this copy. Higher quality 6" x 9" black and white photographic prints are available for any photographs or illustrations appearing in this copy for an additional charge. Contact UMI directly to order.

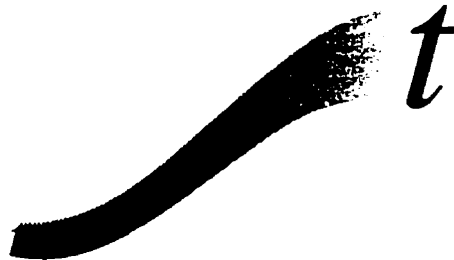
UMI

A Bell & Howell Information Company
300 North Zeeb Road, Ann Arbor MI 48106-1346 USA
313/761-4700 800/521-0600

Formation and Stability of $\text{Sm}_2\text{Fe}_{17}$ Carbides

Ou Mao

Centre for the Physics of Materials
Department of Physics, McGill University
Montréal, Québec, Canada



A Thesis submitted to the
Faculty of Graduate Studies and Research
in partial fulfillment of the requirements for the degree of
Doctor of Philosophy

© Ou Mao, 1997



National Library
of Canada

Acquisitions and
Bibliographic Services

395 Wellington Street
Ottawa ON K1A 0N4
Canada

Bibliothèque nationale
du Canada

Acquisitions et
services bibliographiques

395, rue Wellington
Ottawa ON K1A 0N4
Canada

Your file Votre référence

Our file Notre référence

The author has granted a non-exclusive licence allowing the National Library of Canada to reproduce, loan, distribute or sell copies of this thesis in microform, paper or electronic formats.

The author retains ownership of the copyright in this thesis. Neither the thesis nor substantial extracts from it may be printed or otherwise reproduced without the author's permission.

L'auteur a accordé une licence non exclusive permettant à la Bibliothèque nationale du Canada de reproduire, prêter, distribuer ou vendre des copies de cette thèse sous la forme de microfiche/film, de reproduction sur papier ou sur format électronique.

L'auteur conserve la propriété du droit d'auteur qui protège cette thèse. Ni la thèse ni des extraits substantiels de celle-ci ne doivent être imprimés ou autrement reproduits sans son autorisation.

0-612-30331-4

To Yali, Ruiqi and George

CONTENTS

1	INTRODUCTION	1
1.1	An Overview of Permanent Magnets	1
1.2	Theme of the Thesis	4
2	BACKGROUND	11
2.1	Crystalline Structures	
	— CaCu ₅ -type structure and its derivatives	11
2.1.1	The R ₂ T ₁₇ structure	
	— Dumb-bell pairs of the transition-metal atoms	12
2.1.2	The interstitial compound	14
2.1.3	Disorder in R ₂ T ₁₇	16
2.1.4	The RT ₃ compounds	16
2.1.5	Nd ₂ Fe ₁₄ B-type structure	18
2.2	Magnetic Properties of R-T Compounds	21
2.2.1	The intrinsic properties	21
2.2.2	Interstitial modification of R ₂ Fe ₁₇ properties	26
2.2.3	The extrinsic properties	28
3	EXPERIMENTAL METHODS	33
3.1	A overview of Material Processing by Ball Milling	33
	3.1.1 The process of ball milling	34
	3.1.2 Mechanical alloying	35
3.2	Sample Preparation and Processing	37
	3.2.1 Ingot preparation	37
	3.2.2 Ball milling procedure	38
	3.2.3 Melt spinning	40
	3.2.4 Heat treatments	40
3.3	A simple, high purity glove box	42
3.4	Powder X-Ray Diffraction (XRD)	44
	3.4.1 Profile of XRD peaks	47
	3.4.2 Analysis of grain sizes and strains	48
3.5	Thermomagnetometry (TMA)	50
3.6	Differential Scanning Calorimetry (DSC)	52
4	MECHANICAL ALLOYING OF R₂FE₁₇	55
4.1	Mechanical Alloying	55
4.2	Post-Annealing of Mechanically Alloyed Sm ₂ Fe ₁₇	62
4.3	Post-Annealing of Mechanically Alloyed R ₂ Fe ₁₇	71
4.4	Analysis and Discussion	73
	4.4.1 High pressure phases of rare earth metals	73
	4.4.2 Schematic free energy diagrams for R-Fe	77
4.5	Summary	83

5	PHASE FORMATION IN IRON-RICH SM-Fe-C	85
5.1	Mechanical Alloying	85
5.2	Annealing of Mechanically Alloyed $\text{Sm}_2\text{Fe}_{17}\text{C}_{1.0}$	89
5.2.1	Phase formation during heating at 40 C/min	89
5.2.2	The phase formation under different annealing conditions	98
5.2.3	Summary of the phase formation study	101
5.3	Critical Carbon Contents in $\text{Sm}_2\text{Fe}_{17}\text{C}_x$	102
5.4	Thermodynamic Relation Between the 2-14-1 and 2-17 Carbide	107
5.5	Phase Transformation from $\text{Sm}_2\text{Fe}_{17}\text{C}_{1.0}$ to $\text{Sm}_2\text{Fe}_{14}\text{C}$	110
5.5.1	Grain Refinement Processes	111
5.5.2	Grain Size Dependence of Volume Fraction Kinetics	113
5.5.3	Discussion	120
6	CONCLUSION	124
	APPENDICES	128
A.1	Carbon solubility in $\text{Sm}_2\text{Fe}_{17}\text{C}_x$	128
	REFERENCES	129

FIGURES AND TABLES

FIGURES

1.1	Increase of the energy product during this century	2
2.1	Hexagonal unit cell of RT_5 with the $CaCu_5$ -type structure.	11
2.2	A R-containing layer and a T layer in the RT_5 structure.	12
2.3	An R-containing layer in the R_2T_{17} structure.	13
2.4	An illustration of the different stacking sequence of the Th_2Ni_{17} -type and the Th_2Zn_{17} -type structure.	14
2.5	Hexagonal unit cell of the rhombohedral R_2Fe_{17}	15
2.6	A R-containing layer in the RT_3 structure.	17
2.7	Hexagonal unit cell of the rhombohedral RT_3	17
2.8	Tetragonal unit cell of the $Nd_2Fe_{14}B$ -type structure.	18
2.9	Projections of A and C layers of the $Nd_2Fe_{14}B$	19
2.10	Projections of B and C layers of the $Nd_2Fe_{14}B$	20
2.11	Projections of the C layer.	21
2.12	Molecular-field analysis by a two-sublattice model for $Nd_2Fe_{14}B$	25
2.13	Néel-Slater curve.	27
2.14	A typical hysteresis loop for a hard magnetic material.	29
2.15	A bar magnet.	30
3.1	A scanning electron micrograph of a Sm_2Fe_{17} powder.	39
3.2	A schematic diagram of the melt spinning apparatus.	41
3.3	A schematic Diagram of the in-house constructed glove box system.	43
3.4	Diagram of the electronic logic for recording the lifetime of filament.	44
3.5	Dependence of lifetime of filament on impurity concentrations.	45
3.6	A schematic diagram of the x-ray diffractometer.	46
3.7	An example of a fit for x-ray pattern.	48
3.8	A schematic diagram of the thermomagnetometer.	51
3.9	An example of a TMA scan of a $Sm_2Fe_{17}C_{1.0}$ powder.	52
3.10	A schematic diagram of the DSC apparatus.	53
3.11	An example of DSC scans of a mechanically alloyed Dy_2Fe_{17} powder.	54
4.1	X-ray diffraction scans of Sm_2Fe_{17} ball milled for various time periods.	56
4.2	An enlarged X-ray diffraction scan for Sm_2Fe_{17} ball milled for 15 h.	57
4.3	X-ray diffraction scans of various R_2Fe_{17} powders ball-milled for 20 hours: R = (1) Pr, (2) Nd, (3) Sm and (4) Dy.	59
4.4	Fitting of XRD scan for Pr_2Fe_{17} ball milled for 20 hours.	60
4.5	DSC and TMA heating scans at 40 C/min for the mechanically alloyed Sm_2Fe_{17} powder.	63

4.6	XRD scans for the as-milled and post-annealed $\text{Sm}_2\text{Fe}_{17}$ powders heated to various temperatures.	64
4.7	XRD scans for the mechanically alloyed $\text{Sm}_2\text{Fe}_{17}$ powders heated to the corresponding temperatures as marked in Fig. 4.5.	65
4.8	XRD scans showing the evolution of the superlattice reflection (204).	66
4.9	The dumb-bell Fe pair considered as a rod.	69
4.10	Relationships between S , T_c and c/a	70
4.11	DSC scans at 40 C/min for R_2Fe_{17} (R=Pr, Nd, Sm, Dy) powders mechanically alloyed for 20 h.	72
4.12	DSC scans at 20 C/min and 40 C/min for mechanically alloyed $\text{Sm}_2\text{Fe}_{17}$ and $\text{Dy}_2\text{Fe}_{17}$ respectively.	74
4.13	XRD scans for the ordered- and disordered- R_2Fe_{17} phases.	75
4.14	Schematic free energy diagram for the R-interstitial system.	76
4.15	Schematic free energy diagram of the R-Fe system for R heavier than Sm.	78
4.16	Schematic free energy diagram for Sm-Fe system.	81
4.17	Schematic free energy diagram of the R-Fe system for R=Pr or Nd.	82
5.1	XRD scans of mechanically alloyed (15 h) $\text{Sm}_2\text{Fe}_{17}\text{C}_x$ for (a) $x=0$, (b) $x=0.45$ and (c) $x=1.0$	86
5.2	XRD scans for melt spun $\text{Sm}_2\text{Fe}_{17}$ and $\text{Sm}_2\text{Fe}_{17}\text{C}_{1.0}$ ribbons.	89
5.3	DSC and TMA scans at 40 C/min for the mechanically alloyed $\text{Sm}_2\text{Fe}_{17}\text{C}$ powder.	90
5.4	XRD scans for the as-milled and post-heated $\text{Sm}_2\text{Fe}_{17}\text{C}$ powder to various temperatures.	91
5.5	XRD scans for a mechanically alloyed powder heated to 727 C (pattern II) and an as-cast ingot of $\text{Sm}_2\text{Fe}_{17}\text{C}_{1.0}$ (pattern I).	93
5.6	XRD scans of mechanically alloyed $\text{Sm}_2\text{Fe}_{17}\text{C}_{1.0}$ powder heated to temperatures higher than 727 C at ~ 40 C/min.	95
5.7	XRD patterns for single phase 2-17 and 2-14-1 compound.	96
5.8	TMA scans of samples corresponding to the XRD scans in Fig. 5.6.	97
5.9	TMA scans of mechanically alloyed $\text{Sm}_2\text{Fe}_{17}\text{C}_{1.0}$ powder heated to 960 C at various heating rates. There is a higher α -Fe amount in the 80 C/min powder due to the presence of a large amount of $\text{SmC}_{0.06}$ (refer to Eq. 5.4) as detected by x-ray diffraction.	99
5.10	DSC heating scan at 40 C/min of the melt-spun $\text{Sm}_2\text{Fe}_{17}\text{C}_{1.0}$ ribbon shown in Fig. 5.2	101
5.11	TMA cooling scans of mechanically alloyed $\text{Sm}_2\text{Fe}_{17}\text{C}_x$ ($x=0, 0.3, 0.45, 0.85$ and 1.0) and $\text{Sm}_2\text{Fe}_{14}\text{C}$ powders after annealing at 800 C for 2 h.	104
5.12	Carbon solubility (the critical carbon content), x_c , in $\text{Sm}_2\text{Fe}_{17}$ structure as a function of temperature.	107
5.13	Schematic free energy for $\text{Sm}_2\text{Fe}_{17}\text{-C}$ pseudo-binary system.	108
5.14	A plot of $\chi = (x_m \ln \frac{x_m}{x_m - x_c} + \ln \frac{x_m - x_c}{x_c})$ as a function of T^{-1}	109
5.15	The variation of the sample temperature during the heating up in a furnace at temperature T_f (C).	114

5.16	The TMA scans of a $\text{Sm}_2\text{Fe}_{17}\text{C}_{1.0}$ carbide after annealed at 800 C for various times.	115
5.17	Evolution of transformed $\text{Sm}_2\text{Fe}_{14}\text{C}$ volume fraction with annealing time for various $\text{Sm}_2\text{Fe}_{17}\text{C}_{1.0}$ carbides.	116
5.18	Annealing time required to reach $X=0.5$ as a function of the grain sizes.	117
5.19	Avrami plots for samples of various grain sizes.	118

TABLES

4.1	Compositions of amorphous R-Fe in mechanically alloyed R_2Fe_{17}	62
4.2	The ordering in $\text{Sm}_2\text{Fe}_{17}$	68
4.3	List of DSC results for R_2Fe_{17} (R=Pr, Nd, Sm, Dy and Er) powders mechanically alloyed for 20 h.	73
5.1	Quantitative analysis of x-ray measurements on mechanically alloyed Sm-Fe(-C)powders.	87
5.2	Equilibrium balance between the 2-17 carbide and 2-14-1.	106
5.3	A list of the average grain sizes in the various $\text{Sm}_2\text{Fe}_{17}\text{C}_{1.0}$ samples that have been prepared.	112
5.4	A list of the Avrami exponent.	119

INTRODUCTION

High-performance permanent magnets based on R-Fe (R=rare earths) compounds are the state-of-the-art material for electrical-engineering designs & devices. This thesis is devoted to the study of the formation and the structural stability of the $\text{Sm}_2\text{Fe}_{17}\text{C}_x$ intermetallic compound, an important hard magnetic phase for permanent magnet application.

1.1 An Overview of Permanent Magnets

Permanent magnets are made from hard magnetic materials. A hard magnetic material is so-called because, once magnetized, it is “hard” to be demagnetized. Permanent magnets are widely used in electrical devices to generate static magnetic fields. The largest application of permanent magnets is in motors, generators and acoustic devices. They are concealed in many products. For example, an average car contains about 20 devices based on permanent magnets, a number which strongly increases with extras, like electrically operated windows or sun roofs. There is a constant demand for permanent magnets of better performance in order to reduce the size of devices and to make them more efficient. Better magnets will, in turn, open new opportunities for novel designs. The annual commercial production of magnets is currently valued in excess of US\$2 billion and is predicted to rise to US\$4 billion by year 2000[1].

The relentless development of permanent magnets during this century is well illustrated in Fig. 1.1 by the nearly exponential increase of the energy product, $(\text{BH})_{\text{max}}$. $(\text{BH})_{\text{max}}$, usually expressed as kJ/m^3 or MGOe , provides a measure of the energy density of field that can be produced outside a unit volume of magnet material. In broad terms, the larger the $(\text{BH})_{\text{max}}$, the greater the potential for reducing the size

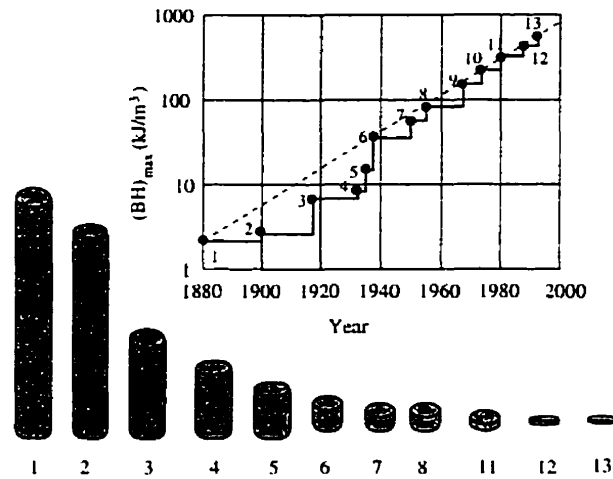


Figure 1.1: Increase of the energy product, $(BH)_{max}$, during this century (from [2]) and the corresponding reduction in magnet size (from [3]). The size has been chosen so that each of them represents the same total magnetic energy. The precise size extent of such reduction depends upon the specific application. The numbers are for (1) carbon steel, (2) tungsten steel, (3) Fe-Co-W-C steel, (4) Fe-Ni-Co-Al, (5) Ticonal II, (6) Ticonal G, (7) Ticonal GG, (8) Ticonal XX, (9) SmCo_5 , (10) $(\text{Sm,Pr})\text{Co}_5$, (11) SmCo_7 , (12) $\text{Nd}_2\text{Fe}_{14}\text{B}$, (13) $(\text{Nd,Dy})_2(\text{Fe,Co})_{14}\text{B}$. (4)-(8) are commonly referred as Alnico magnets.

and weight of a device by replacing either electromagnets or permanent magnets having a lower energy product. The reduction of magnet size with increasingly better performance is illustrated in Fig. 1.1 by a number of permanent magnet bodies, the volume of which has been chosen so that each of them represents the same total magnetic energy.

As illustrated in Fig. 1.1, the most recent advances (from 9 to 13) have occurred when rare earth elements, such as Sm or Nd, were incorporated into the material. These new types of permanent magnets are based on rare earth-transition metal (R-T) intermetallic compounds. In these intermetallic compounds, the rare earth atoms provide magnetic hardening so that the materials are highly coercive against demagnetization, while the transition metal atoms of Fe, Co and Ni are responsible for the high magnetization of the material. The combination of high coercivity and magnetization makes good permanent magnets.

Of the R-T intermetallic compounds, those based on iron-rich R-Fe have the greatest potential for permanent magnet application. Iron has a large magnetic moment ($2.1\mu_B$ per atom) and is of low cost. Neodymium-iron-boron permanent magnets,

currently the highest-performance magnets available, are based on $\text{Nd}_2\text{Fe}_{14}\text{B}$ (for review see [3, 4, 5]). They have become a big commercial success. The manufacture of sintered Nd-Fe-B magnets has increased enormously in the last decade, and now comprises over 20% of the total global permanent magnet market[6].

One weakness of the Nd-Fe-B magnet is its relatively low operating temperature caused by the low Curie temperature, ~ 310 C, of the base $\text{Nd}_2\text{Fe}_{14}\text{B}$, the principal phase in the magnet (Curie temperature, T_c , is the highest temperature at which a spontaneous magnetic moment can exist in a magnetic material). In addition, the Nd-Fe-B magnet has a high temperature-coefficient of coercivity leading to irreversible loss of magnetization. Therefore, the use of 2-14-1 is restricted to below 100 C — a real drawback for high efficiency electric motors. Consequently there is ongoing research for both an improvement to the Nd-Fe-B system and for new hard magnetic phases.

Of the various alternatives, interstitial nitrides and carbides of $\text{Sm}_2\text{Fe}_{17}$ are perhaps the most promising candidates. The compound R_2Fe_{17} is the most iron-rich phase in the binary R-Fe alloy system and consequently has the highest magnetization. Unfortunately its Curie temperature is typically low (around room temperature) and its easy magnetization direction, EMD, lies in the basal plane of the hexagonal unit cell[7], unfavorable for permanent magnets (EMD is the direction in a magnetic crystal along which the spontaneous magnetization is aligned). For a high coercivity, an EMD along the c axis of the hexagonal structure, known as uniaxial anisotropy, is desired. When the EMD is in the basal plane, demagnetization can be realized by the rotation of the magnetic moments by 60° as a result of the six-fold symmetry, a process requiring a relatively small demagnetizing field. A breakthrough was reported in 1990 by Coey *et al* [8, 9] after a series of interstitial nitrides $\text{R}_2\text{Fe}_{17}\text{N}_x$ were prepared by a novel low-temperature gas-solid reaction with a N-containing gas at temperatures of up to 500 C. The gas-solid reaction method was also extended to prepare the interstitial carbides $\text{R}_2\text{Fe}_{17}\text{C}_x$ by reaction with a hydrocarbon gas[10]. The interstitial nitride or carbide is so-called because N and C occupies the interstitial sites of the 2-17 structure. Crystallographically the stoichiometric composition for N or C is 3 atoms per formula, corresponding to full occupation of the octahedral interstitial sites

(the largest interstitial sites) in the 2-17 structure. However the maximum reported value of x at full nitriding or carbiding varies between 2 and 3 according to different researchers[8, 10, 11].

The introduction of interstitial N and C into the 2-17 structure results in a dramatic enhancement in the magnetic properties of the compound. After full nitriding or carbiding, the Curie temperature is increased by up to 400 C and, in case of $\text{Sm}_2\text{Fe}_{17}$, the easy magnetization direction is changed from lying in the basal plane to lying along the c -axis. The large increase in the Curie temperature is mainly due to the expansion of the lattice by interstitial insertion. As a result of these changes, $\text{Sm}_2\text{Fe}_{17}(\text{N,C})_x$ has excellent hard magnetic properties. It has a higher Curie temperature and a larger magnetocrystalline anisotropy than $\text{Nd}_2\text{Fe}_{14}\text{B}$, and its saturation magnetization exceeds that of the $\text{Nd}_2\text{Fe}_{14}\text{B}$ at temperatures above 70 C. $\text{Sm}_2\text{Fe}_{17}(\text{N,C})_x$ probably has the best potential to replace Nd-Fe-B magnets¹ in applications where the operating temperature exceeds 100 C.

1.2 Theme of the Thesis

Even though the $\text{Sm}_2\text{Fe}_{17}(\text{N,C})_x$ has excellent intrinsic magnetic properties, there are difficulties in making good magnets from it (intrinsic properties are those associated with the chemical composition and the crystal structure of a magnetic phase, such as the Curie temperature). While the intrinsic magnetic properties of the phase is vital for a good permanent magnet, the quality of the magnet also critically depends on extrinsic properties, such as the microstructure of the material. A favorable microstructure typically has the feature that grains in the material are very small and aligned along the easy magnetization direction. Alignment is desired for a large remanence (remanence is the magnetization of a magnetized material at zero applied field). Small grain size is required for high coercivity. Generally, the smaller the grains, the higher the coercivity. For example, nanocrystalline $\text{Sm}_2\text{Fe}_{17}\text{N}_x$ with grains of about 100 nm has shown a coercivity as high as $H_c=44$ kOe (35 kA/cm)[12], which is the

¹ $\text{Sm}_2\text{Fe}_{17}(\text{N,C})_x$ is used to denote $\text{Sm}_2\text{Fe}_{17}\text{N}_x$ or $\text{Sm}_2\text{Fe}_{17}\text{C}_x$. In fact $\text{Sm}_2\text{Fe}_{17}\text{N}_x$ has slightly better magnetic properties than $\text{Sm}_2\text{Fe}_{17}\text{C}_x$ and the combination of the two, carbo-nitride $\text{Sm}_2\text{Fe}_{17}(\text{CN})_x$, has the same or even better magnetic properties than $\text{Sm}_2\text{Fe}_{17}\text{N}_x$. $\text{Sm}_2\text{Fe}_{17}\text{N}_x$ and $\text{Sm}_2\text{Fe}_{17}(\text{CN})_x$ are therefore the most promising candidates for permanent magnets.

highest value ever achieved for a R-Fe based compound.

A serious problem facing microstructural processing is that $\text{Sm}_2\text{Fe}_{17}$ carbo-nitrides are metastable. The compound, which is typically synthesized at low temperature by gas-solid reaction, decomposes into a mixture of Sm nitride or carbide and α -Fe when heated above about 550 C[13, 14, 15]. High temperature processing, such as sintering and die-upsetting, that is used for other magnet system like $\text{Nd}_2\text{Fe}_{14}\text{B}$, cannot be applied directly to this metastable phase.

$\text{Sm}_2\text{Fe}_{17}$ carbides are more stable than $\text{Sm}_2\text{Fe}_{17}$ nitrides. For the nitride, the high affinity of Sm with N (the formation enthalpy for the SmN is 150 kJ/g-atom, but only 23 kJ/g-atom for SmC_2 [16]) tends to cause separation of SmN from the $\text{Sm}_2\text{Fe}_{17}$ phase above the decomposition temperature, even at very low N content. In fact the nitride can only be prepared by a gas-solid reaction below the decomposition temperature. In contrast, as a metalloid element, C can be alloyed into the Sm-Fe melt by conventional casting. The interstitial carbide $\text{Sm}_2\text{Fe}_{17}\text{C}_x$ can be formed by annealing of the cast alloy at high temperature, typically between 1100 C and 1150 C[17]. It has the same crystal structure as that prepared by gas-solid reaction. In fact the conventional $\text{Sm}_2\text{Fe}_{17}$ carbide made by this means had been known before the announcement for that synthesized by gas-solid reaction. The maximum C content for the conventional carbide however is only $x=1.0$ [17], lower than values obtained in fully carbided $\text{Sm}_2\text{Fe}_{17}$, which is close to $x=3$. Enhancement in the magnetic properties of $\text{Sm}_2\text{Fe}_{17}$ increases with the interstitial C content. As a consequent the $\text{Sm}_2\text{Fe}_{17}\text{C}_x$ with low C content (for example $\text{Sm}_2\text{Fe}_{17}\text{C}$) has only moderate hard-magnetic-properties compared to the fully carbided ones. For this reason, the potential of the $\text{Sm}_2\text{Fe}_{17}$ carbide as a candidate for permanent magnets was not realized until the discovery of the low-temperature gas-solid reaction.

Because they are more stable, the $\text{Sm}_2\text{Fe}_{17}$ carbides are in principle a better starting point for processing than the nitrides. For this reason it was adopted in our laboratory as a precursor for magnet production and, indeed, preliminary work has demonstrated that the $\text{Sm}_2\text{Fe}_{17}\text{C}_x$ of $x=0.5-1.0$ can be sintered in the same way as $\text{Nd}_2\text{Fe}_{14}\text{B}$ in order to produce magnets with good grain alignment. A prototype

magnet¹ has been produced with a better quality than products of Sm-Fe-based magnets produced by other methods, such as melt-spinning, HDDR² and mechanical alloying[19].

In order to fully evaluate the potential of the $\text{Sm}_2\text{Fe}_{17}$ carbide as starting material for the evolution of a high performance magnet we need to have an in-depth understanding of its stability and formation, and this is the topic of the present thesis.

Two questions arise in connection with the stability of $\text{Sm}_2\text{Fe}_{17}$ carbide: the first is over what range of temperature and carbon concentration range is the $\text{Sm}_2\text{Fe}_{17}$ carbide stable, and the second is what are the kinetics and products of the transformation. A related question is whether the thermodynamics or the kinetics are influenced by grain size. For example, if a transformation demands that one of the components be expelled from the bulk, then obviously this will proceed far more readily in a system where the grain size is small. At the same time processing to produce small grains may introduce so much strains and so many defects that the thermodynamics itself may be altered; and in a nanograin material these defects may not necessarily be annealed out easily.

With regard to the thermodynamic stability, it is known that the binary $\text{Sm}_2\text{Fe}_{17}$ is an equilibrium phase, whereas the fully carbided $\text{Sm}_2\text{Fe}_{17}\text{C}_x$ is a metastable phase. Therefore, there must be a critical carbon content, x_c , which divides the stable from the metastable region. It is important to learn whether x_c is larger than 0.5, or in what temperature range x_c is larger than 0.5, because only when $x > 0.5$ $\text{Sm}_2\text{Fe}_{17}\text{C}_x$ has the magnetically uniaxial anisotropy and can be used to align the grains for sintering[20].

Although conventional $\text{Sm}_2\text{Fe}_{17}\text{C}_x$ with $x=0-1.0$ exists, it is always prepared by annealing above 1100 C. We therefore need to know what is (are) the stable phase(s) below 1100 C? There have been too few studies on the phase formation in R-Fe-C ternary systems to determine the critical carbon content, and we have therefore investigated phase formation in the $\text{Sm}_2\text{Fe}_{17}\text{C}_x$ alloys, determined the critical carbon

¹The $\text{Sm}_2\text{Fe}_{17}\text{C}_x$ of $x=0.5-1.0$ is the precursor for processing the favorable microstructure. In order to turn the precursor into a magnet further nitriding of the $\text{Sm}_2\text{Fe}_{17}\text{C}_x$ is required. The carbo-nitride has the superior permanent magnet properties.

²HDDR is short for the hydrogenation \rightarrow disproportionation \rightarrow desorption \rightarrow recombination[18]

content and identified the stable phase(s) below 1100 C.

With regard to the transformation kinetics, there is an unexplained phenomenon associated with phase formation and transformation in the Sm-Fe-C alloy system. It has been reported that annealing below a transition temperature, $T_t=1000$ C, yields $\text{Sm}_2\text{Fe}_{14}\text{C}$, an isostructure of $\text{Nd}_2\text{Fe}_{14}\text{B}$, and subsequent annealing above T_t transforms the $\text{Sm}_2\text{Fe}_{14}\text{C}$ into $\text{Sm}_2\text{Fe}_{17}\text{C}_x$ ¹. However the reverse transformation, $\text{Sm}_2\text{Fe}_{17}\text{C}_x \rightarrow \text{Sm}_2\text{Fe}_{14}\text{C}$, has not been seen[21]. In fact, $\text{Sm}_2\text{Fe}_{17}\text{C}_x$ formed by high temperature annealing is apparently stable over the whole temperature range up to its melting point. The reverse phase transformation is perhaps inhibited by slow transformation kinetics because the transformation demands the expelling of Fe atoms from the bulk, which process requires a long-range diffusion. It is therefore important to know whether the $\text{Sm}_2\text{Fe}_{17}\text{C}_x$ is still stable in its nanocrystalline form. To answer this question we have prepared nanocrystalline $\text{Sm}_2\text{Fe}_{17}\text{C}_x$ and studied its phase transformation and, in particular, have investigated the grain size dependence of this phase transformation. Combining the phase formation and transformation studies, we hope to gain an in-depth understanding, thermodynamically and kinetically, of this phase transformation.

Sample preparation is obviously a crucial part of this study. Ball milling is the major sample preparation method we have used. It is a mechanical process that can be and is used industrially to produce large amount of material, although typically only a few grams are made with laboratory equipment. Ball milling operates by moving hardened balls energetically inside a rotating or vibrating container with thick & hardened walls. The collisions between the balls or the ball and walls transfer the mechanical energy to the powder material trapped in between. Part of the transferred energy is stored in the forms of crystalline defects and atomic disorders. The rest is dissipated as heat.

Ball milling is widely used as a non-equilibrium process for many purposes. In this thesis we will study the mechanical alloying and the grain refinement effects of the ball milling process. In mechanical alloying, a steady-state is reached by an extended

¹The peritectoidal transformation from $\text{Sm}_2\text{Fe}_{14}\text{C}$ to $\text{Sm}_2\text{Fe}_{17}\text{C}_x$ involves other phase(s), such as SmFeC and $\alpha\text{-Fe}$, depending on the composition of the Sm-Fe-C alloy.

ball milling process, where the final product normally depends only on the average chemical composition and milling conditions. The final product is usually metastable containing nanocrystalline and/or amorphous phases. Mechanically alloyed powders are used instead of cast alloys as the precursors for our phase formation study. The nano-scale mixing of the constituent phases in the mechanically alloyed powders enhances the phase formation kinetics so that the phase formation can be realized either in relatively short times or at relatively low temperatures. The grain refinement effect results from the repeated deformation, fracture and coalescence. Ball milling was also used to reduce the grain sizes of both $\text{Sm}_2\text{Fe}_{17}$ and the carbide in order to produce nanocrystalline samples. Rapid solidification was also used in our studies as a comparative non-equilibrium process to the ball milling technique.

The phase formation and transformation was characterized by x-ray diffraction, thermomagnetometry and differential scanning calorimetry. X-ray diffraction is perhaps the most reliable standard means for the determination of the structure and the simplest means for phase analysis; it is also easy to access. For this reason it was used extensively in our studies for phase identification, quantitative phase analysis and determination of grain size & lattice strain. For intermetallic compounds, disorder is used to denote deviation of the structure from stoichiometry. Disorder in the 2-17 structure was also determined by x-ray diffraction. Thermomagnetometry is used to measure the magnetization during heating, cooling or under isothermal conditions and is a powerful tool for the study of magnetic materials. It was typically used to determine the Curie temperature and magnetization of a magnetic phase. In our studies thermomagnetometry was adapted to identify a magnetic phase through its Curie temperature, and also to determine the volume fraction of a magnetic phase with respect to other magnetic phase(s) by its corresponding magnetization. It was also developed to determine the carbon content in the $\text{Sm}_2\text{Fe}_{17}\text{C}_x$ phase from the corresponding change in the Curie temperature. Differential scanning calorimetry (DSC) is very sensitive for structural changes which are mostly accompanied by enthalpy changes. DSC was thus used to follow the phase formation and transformation by monitoring the change in enthalpy flow. For the study of magnetic phase formation and transformation thermomagnetometry is also used in addition to DSC.

Phase formation and transformation in mechanically alloyed iron-rich Sm-Fe-C is the principal subject of this thesis. Ternary Sm-Fe-C is a complicated system. The strategy was therefore to start with a binary system. A series of mechanically alloyed R_2Fe_{17} powders were investigated for a better understanding of both the Sm-Fe alloy system in general and the Sm_2Fe_{17} compound in particular. The objective was to learn (1) what is the steady-state in the mechanically alloyed R_2Fe_{17} , and (2) how the 2-17 structure is formed from the mechanically alloyed precursors. Phase formation and transformation in the mechanically alloyed $Sm_2Fe_{17}C_x$ with various carbon contents was then studied. The objective in this case was to learn (1) how the 2-17 structure with interstitial carbon is formed, (2) what is the maximum C content in the 2-17 structure, the critical content x_c , and (3) what phase(s) is (are) formed with $x > x_c$.

Phase transformation from $Sm_2Fe_{17}C_x$ to $Sm_2Fe_{14}C$ was the second subject for study. As required by this study, the grain refinement process was investigated first. The objective was to prepare the nanocrystalline $Sm_2Fe_{17}C_x$ with various grain sizes. Emphasis was on the ball milling of Sm_2Fe_{17} /graphite mixture in the hope of forming a nano-scale mixing of Sm_2Fe_{17} and graphite by ball milling. Solid-solid reaction between the Sm_2Fe_{17} and graphite leading to the formation of nanocrystalline $Sm_2Fe_{17}C_x$ was then studied. The phase transformation from $Sm_2Fe_{17}C_x$ was carried out with nanocrystalline $Sm_2Fe_{17}C_x$ samples. Samples prepared by other methods were also studied. The objective was to learn (1) what the transformation product is and (2) what the kinetics of the phase transformation and its grain size dependence are.

The following is the layout of this thesis. In Chapter 2, the background for this study is surveyed. The topics include the crystal structures and magnetic properties of R-Fe compounds. In Chapter 3, the experimental methods used in this thesis are described. These are: alloy preparation, sample handling & processing and characterization techniques. The results and discussion of the studies are presented in Chapter 4 and 5. The study of phase formation in mechanically alloyed R_2Fe_{17} is presented in Chapter 4. In Chapter 5, the ternary Sm-Fe-C system is studied. The subjects are: (1) phase formation in mechanically alloyed iron-rich Sm-Fe-C, and (2) effect of grain sizes on phase transformation from $Sm_2Fe_{17}C_{1.0}$ to $Sm_2Fe_{14}C$. Chap-

ter 6 summarizes the thesis.

BACKGROUND

2.1 Crystalline Structures

— CaCu_5 -type structure and its derivatives

Many of the structures of R-T based compounds (R=rare earth and T=transition metals) can be derived from the hexagonal CaCu_5 structure (space group $P6/mmm$)[22, 7], which is illustrated in Fig. 2.1. As seen from Fig. 2.1, one characteristic of the RT_5 structure is alternate layers containing rare earth (but having transition metal atoms as well) and transition metal layers stacking along the c axis. Fig. 2.2 illustrates the R-containing and the Fe layers in this structure.

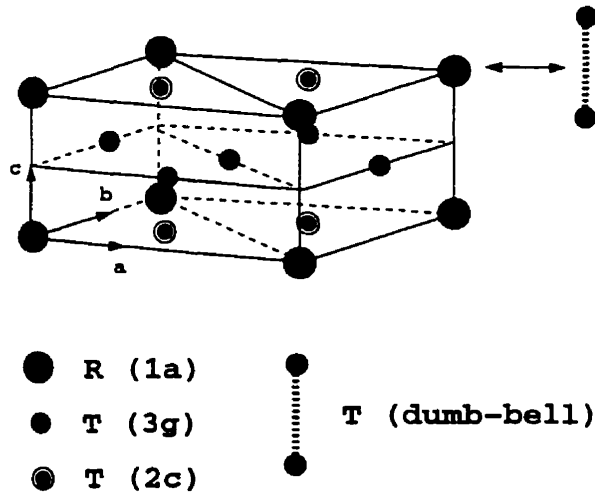


Figure 2.1: Hexagonal unit cell of RT_5 with the CaCu_5 -type structure. The manner of the T dumb-bell substitution is also illustrated.

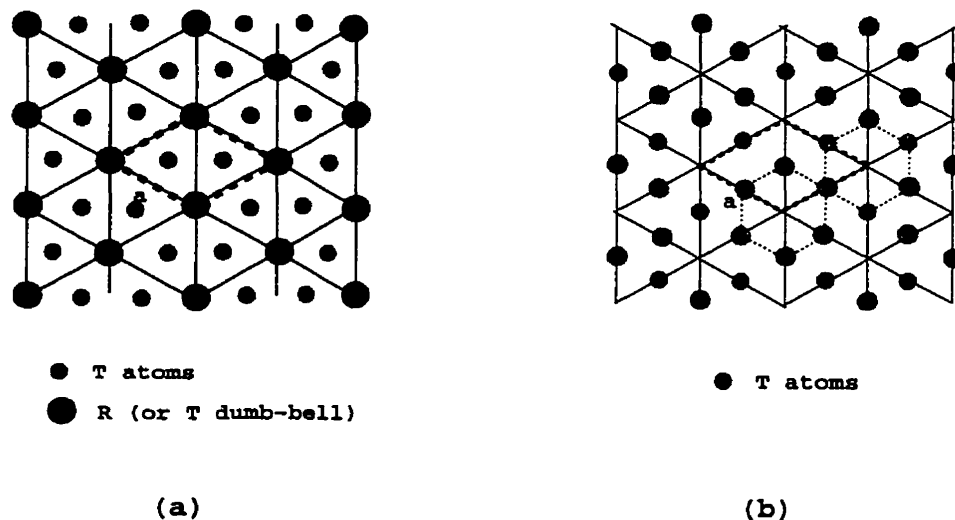


Figure 2.2: A R-containing layer (a) and a T layer (b) in the RT_5 structure. The thick broken lines illustrate the frame of a unit cell in the layers and the thin broken lines illustrate the T atom nets that is usually seen in R-T compounds, such as R_2Fe_{17} and $Nd_2Fe_{14}B$ shown in Fig. 2.5 and 2.8.

2.1.1 The R_2T_{17} structure

— Dumb-bell pairs of the transition-metal atoms

Some of the transition metal rich R-T structures are obtained by replacing an appropriate amount of rare earth atoms by transition metal dumb-bell pairs. The stoichiometry of the compounds of those structures, therefore, is

$$R_{1-\delta}T_{5+2\delta} \quad (2.1)$$

where δ is the fraction of the rare earth atoms being replaced by the dumb-bell pairs. Fig. 2.1 illustrates the manner of the replacement, which, of course, only occurs in the layers with rare earth atoms. The R_2T_{17} structure is derived when 1/3 of the rare earth atoms is replaced in a certain order by the transition metal dumb-bell pairs, $\delta=1/3$ ¹. This ordered replacement (*i.e.* every third rare earth atom, along lines connecting the rare earth atoms, is replaced by a transition metal dumb-bell) in the RT_5 structure leads to a unit cell of the R_2T_{17} which is larger than the original RT_5 unit cell (see Fig. 2.3, 2.5 or 2.4). The R_2T_{17} is therefore considered as a

¹Other examples of R-T compounds containing the T dumb-bell pairs are the $RT_{12}[7]$ ($\delta=1/2$) and $R_3T_{29}[23]$ ($\delta=2/5$).

superstructure of the RT_5 . The lattice constant a for R_2T_{17} , as illustrated in Fig. 2.3, is $\sqrt{3}$ times as large as that for RT_5 . As shown in the figure in replacing rare earth atoms with transition metal dumb-bells there are three equivalent R sites, A, B and C, leading to three types of stacking variations along the c -axis. Because the replacement only occurs in the layers containing rare earth atoms, the atomic arrangement in the transition metal layer remains similar to that shown in Fig. 2.2(b).

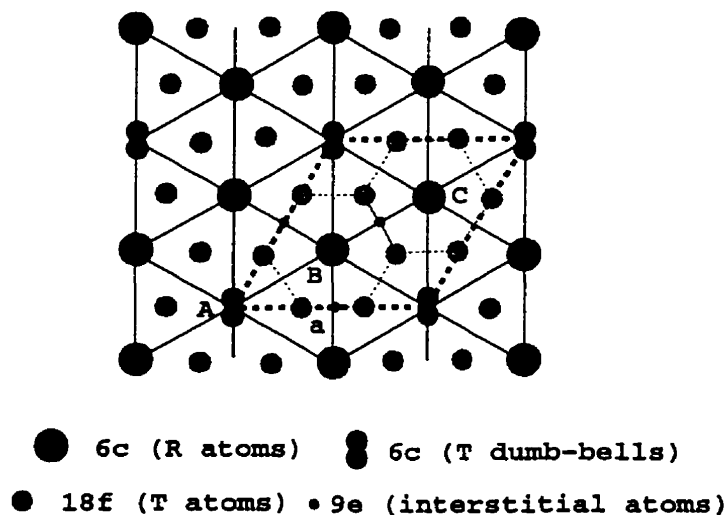
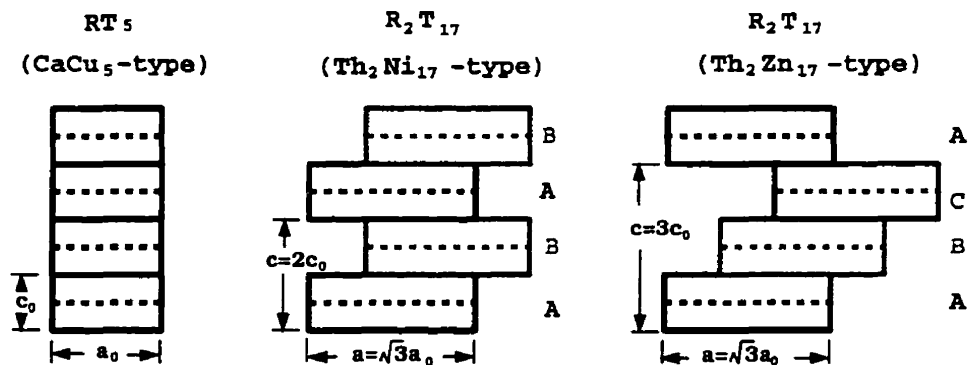


Figure 2.3: An R-containing layer in the R_2T_{17} structure illustrating the manner of dumb-bell substitution and the unit cell in the layer (thick broken lines). a is the lattice constant. The thin broken lines illustrate the T atom (18f) network. A, B and C denote three different positions for the dumb-bell pair in the unit.

The crystal structure of a R_2T_{17} compound is thus constructed by stacking the layers containing rare earth (shown in Fig. 2.3) and transition metals (shown in Fig. 2.2(b)) alternately. The layer containing rare earth, however, has three variations depending on which of the three rare earth sites (A, B and C as shown in Fig. 2.3) are replaced by the dumb-bells. There are two distinct structures, the $\text{Th}_2\text{Zn}_{17}$ -type and the $\text{Th}_2\text{Ni}_{17}$ -type, corresponding to two different stacking orders of the layers containing rare earth. As illustrated in Fig. 2.4, the $\text{Th}_2\text{Ni}_{17}$ -type structure (space group $\text{P6}_3/\text{mmc}$) is derived by stacking the layers containing rare earth in the order of ABABAB... The resulting c axis is, therefore, twice as large as the original 1:5 structure. On the other hand the $\text{Th}_2\text{Zn}_{17}$ -type structure (space group $\text{R}\bar{3}\text{m}$) has the order ABCABCABC...; and its c axis is therefore 3 times as large as the

original 1:5 structure. In the sense of the stacking sequences, the relationship between the $\text{Th}_2\text{Ni}_{17}$ -type and the $\text{Th}_2\text{Zn}_{17}$ -type structure is analogous to that between the hexagonal (*hcp*) and cubic (*fcc*) structures (see, for example, [24], for the relationship between *hcp* and *fcc*).



Replacing $1/3$ R in special orders

Figure 2.4: An illustration of the different stacking sequence of the $\text{Th}_2\text{Ni}_{17}$ -type and the $\text{Th}_2\text{Zn}_{17}$ -type structure and the relationship of the lattice constants with the original CaCu_5 -type structure. The R-containing layers, A, B or C, was illustrated in Fig. 2.3.

The structure of the R_2Fe_{17} compound falls into either of the above two, $\text{Th}_2\text{Zn}_{17}$ -type or $\text{Th}_2\text{Ni}_{17}$ -type. For the light rare earths up to $\text{R}=\text{Sm}$, the structure of the R_2Fe_{17} is the $\text{Th}_2\text{Zn}_{17}$ -type, while for the heavy rare earths with $\text{R} \geq \text{Dy}$, the structure is the $\text{Th}_2\text{Ni}_{17}$ -type. Between Sm and Dy, such as Gd and Tb (and Y as well) both of the structures exist for the same R[25] and they may coexist. This suggests that the energy difference between these two structures is very small for $\text{R}=\text{Gd}$, Tb and Y.

Fig. 2.5 illustrates the crystal structure of R_2Fe_{17} with the $\text{Th}_2\text{Zn}_{17}$ -type structure. The hexagonal unit cell of the structure is a conventional unit cell. The primitive unit cell of the $\text{Th}_2\text{Zn}_{17}$ -type structure is the rhombohedral unit cell, which volume is $1/3$ of the conventional cell. The relationship between the conventional hexagonal cell and the primitive rhombohedral cell is illustrated in the same figure.

2.1.2 The interstitial compound

Large amounts of interstitial atoms, such as H, C and N, can be introduced into the R_2Fe_{17} structures without any change in the space group, *ie.* $\text{R}\bar{3}\text{m}$ or $\text{P6}_3/\text{mmc}$.

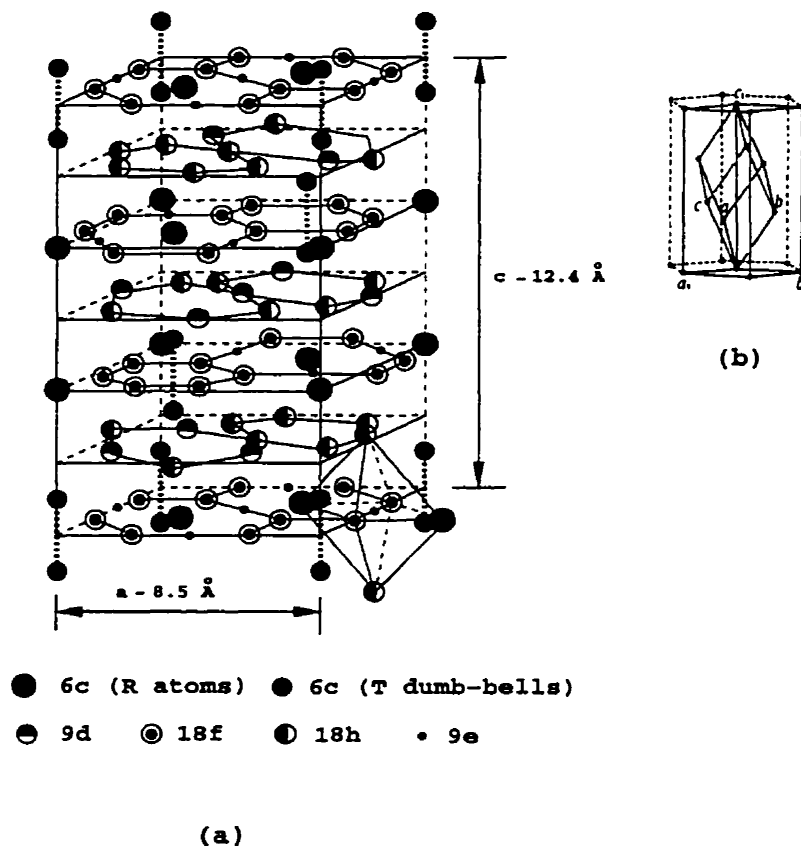


Figure 2.5: (a) Hexagonal unit cell of the rhombohedral R_2Fe_{17} with the $\text{Th}_2\text{Zn}_{17}$ -type structure. Different types of crystallographical sites are indicated using the Wyckoff notation, such 6c, 9d, etc. In this structure, there is only one type of R sites, 6c, but there are 4 inequivalent sites for Fe atoms, namely, 6c, 9d, 18f and 18h. Also illustrated is the largest interstitial sites, 9e, in the structure, the only ones that carbon or nitrogen atoms can be inserted into. (b) An illustration of the relationship between the conventional hexagonal unit cell and the primitive rhombohedral unit cell.

Such compounds formed by the insertion of interstitial atoms are called the interstitial compounds; they are also called the R_2Fe_{17} hydrides, carbides or nitrides according to whether H, C or N is inserted. One type of the interstitial sites in the $\text{Th}_2\text{Zn}_{17}$ -type structure is illustrated in Fig. 2.5. These are the largest interstitial sites in the structure (with a radius of about 0.7\AA [26]) and are the *only* ones that can accommodate interstitial carbon or nitrogen atoms[27, 28, 29, 30]¹. These 9e sites are the so-called octahedral interstitial sites because the site is enclosed in an octahedron constructed by two rare earth atoms and four Fe atoms, as shown in Fig. 2.5. The 9e sites can be partially or fully occupied. Full occupation leads to three interstitial atoms per

¹The smallest interstitial atom, hydrogen, may occupy other interstitial sites[31].

formula unit, corresponding to $R_2Fe_{17}(C,N)_3$.

2.1.3 Disorder in R_2T_{17}

As shown in Fig. 2.3, in the 2-17 structure the replacement of the 1/3 of the R atoms occurs in an ordered manner, leading to a larger unit cell than the original $CaCu_5$. However, the order of the structure is disturbed when the substituted dumb-bell pairs replace the rare earth atoms randomly. Such disorder has been reported in the 2-17 compounds prepared by rapid quenching from the melt[32, 33, 34]. With complete disorder each rare earth site in the RT_5 structure has a probability of 1/3 of being occupied by the transition metal dumb-bells. In this way the superstructure of the R_2T_{17} disappears and the unit cell of the completely disordered R_2T_{17} becomes the same as the RT_5 structure, except that the $1a$ sites (see the indication in Fig. 2.1) are now occupied by either rare earth atoms or transition metal dumb-bells. This type of disorder due to random replacement was first identified in the $TbCu_7$ alloy[35] and hence the disordered 2-17 structure is sometimes referred to as the $TbCu_7$ -type structure. Another type of disordering of R_2T_{17} may occur as a result of random stacking orders of the A, B and C layers, which are illustrated in Fig. 2.4.

2.1.4 The RT_3 compounds

The structure of the rare earth-rich compound, RT_3 , is also a derivative of the RT_5 structure. It is derived by replacing an appropriate amount of transition metal atoms with rare earth atoms. In this case the formula of the compound is given by

$$R_{1+5\Delta}T_{5-5\Delta} \quad (2.2)$$

where Δ is the fraction of the transition metal atoms replaced by the rare earth atoms. For RT_3 , the Δ value is 1/10, corresponding to the replacement of one transition metal atom in every two RT_5 units by a rare earth atom. Fig. 2.6 illustrates the manner of the ordered replacement for the 1-3 structure, which only occurs in one of every two layers containing rare earth, the other layers remaining the same as that in the 1-5 structure. Similar to the R_2T_{17} structure, the RT_3 structure is constructed by stacking R layers and T layers in an ordered way. The crystal structure in a

conventional hexagonal unit cell of the rhombohedral RT_3 (PuNi_3 -type structure, space group $\text{R}\bar{3}\text{m}$) is illustrated in Fig. 2.7.

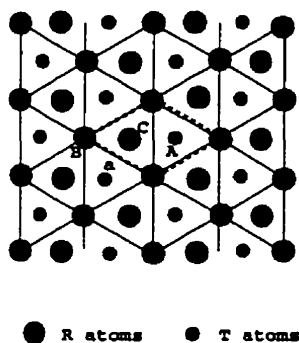


Figure 2.6: A R-containing layer in the RT_3 structure illustrating the manner of dumb-bell substitution and the unit cell in the layer (thick broken lines). a is the lattice constant. A, B and C denote three different positions for the replacement.

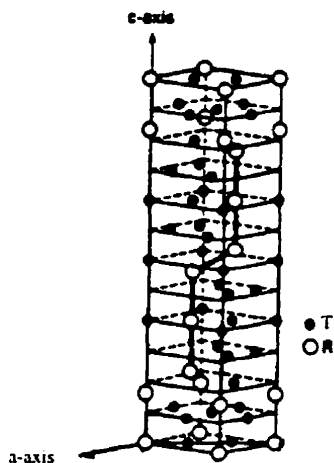


Figure 2.7: Hexagonal unit cell of the rhombohedral RT_3 with the PuNi_3 -type structure (from [36]). The c -axis is 6 times as long as the original RT_5 structure.

Disorder in the 1-3 structure has been observed in Sm-Fe(-Zr) alloys by the crystallization of an amorphous phase at relatively low temperatures, 700–800 C[37, 38]. The relation between the structure of ordered and disordered 1-3 is similar to that between ordered and disordered 2-17. The difference is that in the 2-17 structure some rare earth atoms are randomly replaced by transition metal dumb-bells whereas for the disordered 1-3 some transition metal atoms are replaced randomly by rare earth atoms.

2.1.5 $Nd_2Fe_{14}B$ -type structure

The $Nd_2Fe_{14}B$ -type phase in iron-rich R-Fe-B alloys was found in the early years of 1980s by many researchers (see, for example, [39], [40], [41]). In that early work its chemical formula was tentatively and variously identified, such as $R_3Fe_{16}B$, $R_3Fe_{21}B$ and $R_3Fe_{20}B$. The correct stoichiometry, $R_2Fe_{14}B$, and detailed crystal structure were soon determined [42, 43, 44]. Fig. 2.8 displays the $Nd_2Fe_{14}B$ unit cell. The lattice symmetry is tetragonal (space group $P4_2/mnm$), and each unit cell contains four formula units, or 68 atoms.

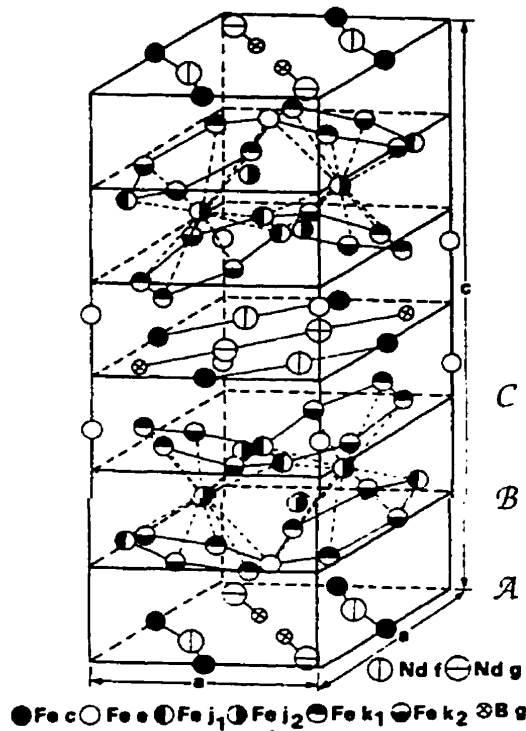


Figure 2.8: Tetragonal unit cell of the $Nd_2Fe_{14}B$ -type structure (from [4]). The c/a ratio in the figure is exaggerated to emphasize the puckering of the hexagonal iron nets. There are six crystallographically distinct iron sites, two different rare earth positions and one boron site, as denoted by the Wyckoff notations. The projections of layers A, B and C are displayed in Fig. 2.9, 2.10 and 2.11, respectively.

The $Nd_2Fe_{14}B$ -type structure has many analogies with the $CaCu_5$ -type structure although there is no explicit transformation from the $CaCu_5$ structure to the $Nd_2Fe_{14}B$ structure as there is for the R_2Fe_{17} and the RT_3 structures. The $Nd_2Fe_{14}B$ -type

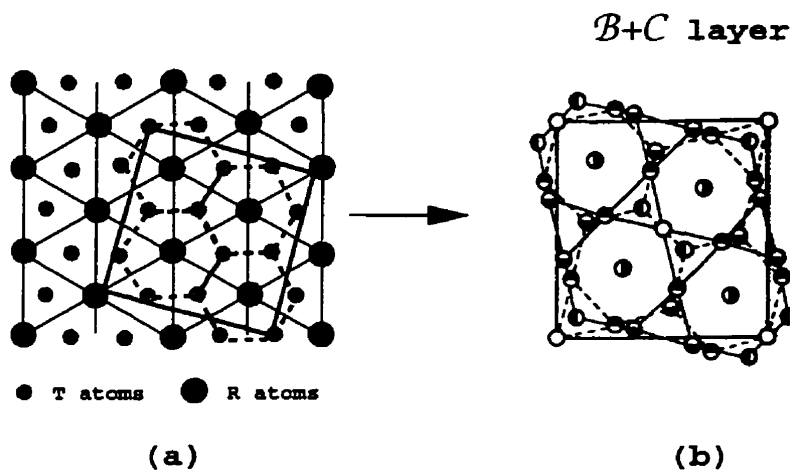


Figure 2.10: (a) An R-containing layer in the RT_5 . The square frame corresponds the tetragonal unit cell of the $Nd_2Fe_{14}B$; the broken lines illustrate the T atom nets which are almost identical to the Fe atom nets in the $Nd_2Fe_{14}B$. (b) Projections of B (the nets indicated with broken lines) and C (nets of solid lines) layers of the $Nd_2Fe_{14}B$ shown in Fig. 2.8; there is a 30° rotation from one type of net to the other; symbols for different atoms were defined in Fig. 2.8; The $Fe(j_2)$ atoms may be considered belonging to the B layer and are at the position of R atoms in the original RT_5 (they are also superimposed to Nd atoms in the A layer).

From these displayed similarities, we therefore conclude that layers A and B in $Nd_2Fe_{14}B$ are very similar to the layer containing rare earth in RT_5 and the C layer in $Nd_2Fe_{14}B$ is cognate to the transition metal layer in RT_5 .

Given the similarities of RT_5 and $Nd_2Fe_{14}B$ on the one hand and of RT_5 and R_2T_{17} on the other, it is not surprising that many parallels also exist between $Nd_2Fe_{14}B$ and R_2T_{17} . The layered arrangement and the presence of hexagonal T nets surrounding R atoms in each structure are apparent from Figs. 2.1 and 2.5. Despite the different symmetries, the lattice parameters of $Nd_2Fe_{14}B$ ($a=8.80 \text{ \AA}$, $c=12.20 \text{ \AA}$) approach those of its nearest R_2T_{17} relative, Nd_2Fe_{17} ($a=8.57 \text{ \AA}$, $c=12.44 \text{ \AA}$). The most significant correlation is perhaps the fact that the $Fe(j_2)$ atoms in $Nd_2Fe_{14}B$ and the $Fe(6c)$ atoms in Nd_2Fe_{17} are cognate magnetically as well as crystallographically[45, 46]. Each site has the largest number of near-neighbor Fe atoms (12) and the largest Fe magnetic moment in its structure.

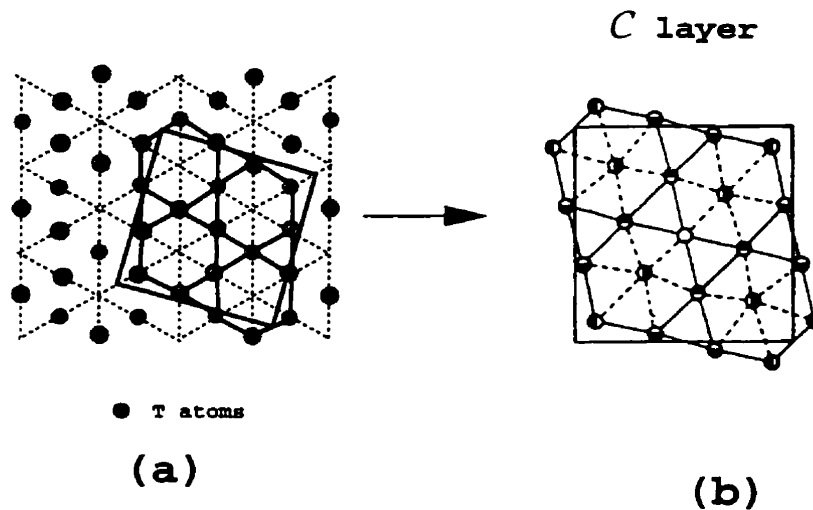


Figure 2.11: (a) A T layer in the RT_5 . The square frame corresponds the tetragonal unit cell of the $Nd_2Fe_{14}B$. (b) Projections of the C layer (notice, however, that the $Fe(j_2)$ atoms in the center of the solid-line nets belongs to the B layer). The two types of T nets in (a) and (b) are almost identical.

2.2 Magnetic Properties of R-T Compounds

The magnetic properties of a magnetic material are generally divided into two types: the intrinsic and the extrinsic properties. Intrinsic properties are those essentially related to the chemical composition and the crystal structure of a magnetic phase, which are independent of the microstructure of the material. The most important intrinsic properties for high performance permanent magnets are the Curie temperature T_c (magnetic ordering temperature), saturation magnetization M_s and magnetocrystalline anisotropy field H_a . Extrinsic properties, on the other hand, are those critically dependent on the microstructure of the material, such as coercivity H_c and remanence M_r .

2.2.1 The intrinsic properties

Curie temperature and the temperature dependence of magnetization:

The Curie temperature T_c is the highest temperature at which a spontaneous magnetic moment can exist in a magnetic material. It is determined by the strength of the exchange interaction between magnetic moments. The magnetic moment of an atom (or ion) originates from its total angular momentum, \mathbf{J} , and their relationship

follows

$$\boldsymbol{\mu} = g_J \mu_B \mathbf{J} \quad (2.3)$$

where g_J is the Landé factor and μ_B is the Bohr magneton, equivalent to the spin moment of an electron in projection of a particular direction (the measurable spin moment associated with the electron). The total angular momentum is the sum of the orbital angular momentum \mathbf{L} and the spin angular momentum \mathbf{S} . The value of the Landé factor reflects the relative contribution of the orbital and spin to the total angular momentum and hence the magnetic moment (see [24] for example). The 4f electron shells, which are responsible for the magnetism of the rare earth atoms, are localized inside $5s^2$ and $5p^6$ electron shells and consequently keep their atomic levels. The total magnetic moment can be described by Hund's rules[24]. The 3d electrons, which are responsible for the magnetism of the transition metal atoms, are more itinerant: the 3d electron wave functions of neighboring atoms overlap considerably, which lead to 3d electron bands rather than 3d levels. As a result the orbital angular momentum of the 3d shell is quenched to nearly zero and the magnetic moment is usually the total spin moment of the 3d electrons. The 3d electrons are partly localized: each electron spends only a finite time on an atom before hopping to one of its neighbors. How well is the 3d electron localized is still a subject under discussion (see [47], [48] and [49], for example).

In a localized picture, magnetic moments are attributed to individual atoms in a solid and the exchange interaction between the two atomic moments is often expressed in terms of a Heisenberg Hamiltonian¹

$$H_{ex} = -J_{ex} \boldsymbol{\mu}_i \cdot \boldsymbol{\mu}_j \quad (2.4)$$

where J_{ex} is the exchange integral indicative of the strength of the exchange interaction between the two moments and $\boldsymbol{\mu}_i$ and $\boldsymbol{\mu}_j$ are the vectors of the two magnetic moments. The Heisenberg model is often used even on transition metals where the local moment model is more dubious. In Eq. 2.4, when J_{ex} is positive, the adjacent

¹Although the Heisenberg Hamiltonian is generally expressed in terms of spin[53, 24] it is convenient to write it in terms of magnetic moments in order to describe phenomenologically the interaction between magnetic moments.

moments are coupled parallel corresponding to a *ferromagnetic* interaction, while at an *antiferromagnetic* interaction J_{ex} is negative and the adjacent moments are therefore coupled anti-parallel. For a ferromagnetic material with one type of magnetic moment, the Curie temperature is predicted by the mean-field approximation (or molecular field theory¹) to be

$$T_c = zJ_{ex}g_J^2J(J+1)/3k_B = zJ_{ex}\mu^2/3k_B \quad (2.5)$$

In the above equation, z is the number of nearest neighbors and k_B is the Boltzmann constant. Within the mean field theory, the temperature dependence of the spontaneous magnetization of each moment is obtained to be

$$m(T) = g_J\mu_BJB_J\left(\frac{g_J\mu_B H}{k_B T}\right) = m_0B_J\left(\frac{m_0 B}{k_B T}\right) \quad (2.6)$$

where H (B) is the magnetic field (induction) inside the crystal and is the molecular field for spontaneous magnetization, m_0 is the magnetization at zero temperature and $B_J(x)$ is the Brillouin function defined as

$$B_J(x) = \frac{2J+1}{2J} \coth \left[\frac{(2J+1)x}{2J} \right] - \frac{1}{2J} \coth \left[\frac{x}{2J} \right]. \quad (2.7)$$

The magnetization of a material, M , is defined as the total moment per unit volume: $M = nm$, where n is the number of the magnetic atoms per unit volume.

For R-T intermetallic compounds, however, there are three types of exchange interactions, namely, the T-T, R-T and R-R interactions. The corresponding exchange integrals are J_{TT} , J_{RT} and J_{RR} respectively. All of them have to be taken into account to describe the magnetization and the Curie temperature. This is usually done within the molecular field theory by a two-sublattice (R and T sublattices) model.

In most R-T compounds which are of interest for permanent magnets, J_{TT} and J_{RR} are both positive, the two lattices being both ferromagnetic; the magnetization of each sublattice, $M_R(T)$ or $M_T(T)$, is described by a Brillouin function as defined in Eq. 2.7. The exchange interaction between R and T sublattice, J_{RT} , is either positive

¹In the mean field approximation the exchange interaction, which must be summed up over all pairs of moments, is replaced by a molecular field acting on a single moment, which is generated by all the other moments in the crystal.

(ferromagnetic) for the light rare earths or negative (antiferromagnetic) for the heavy rare earths. The total magnetization of an R-T compound M_{R-T} is

$$M_{R-T} = |M_T \pm M_R| \quad (2.8)$$

The total magnetization is high for the light rare earths and low for the heavy rare earths.

The R-R interaction is indirect because the 4f electrons are well localized and consequently there is no overlap between the 4f shells of different atoms. The R-R interaction is mediated by the conduction electrons, the well-known RKKY interaction[50]. As a result the R-R interaction is very weak compared to the other interactions and, for estimating the Curie temperature, it is usually neglected. The two sublattice model therefore yields[5]:

$$T_c \cong (a_{TT} + \sqrt{a_{TT}^2 + 4a_{RT}^2})/3k_B \quad (2.9)$$

and the definitions of a_{TT} and a_{RT} are

$$\begin{aligned} a_{TT} &= z_{TT} J_{TT} \mu_T^2 \\ a_{RT}^2 &= z_1 z_2 J_{RT}^2 \mu_R^2 \mu_T^2 \end{aligned}$$

where z_{TT} represents the average number of the similar neighbor atoms to a T atom; z_1 and z_2 represent the number of T neighbors to an R atom and the number of R neighbors to a T atom respectively; μ_R and μ_T are the average magnetic moment of an R and T atom respectively.

Fig. 2.12 illustrates an example of the application of the two-sublattice model to a $\text{Nd}_2\text{Fe}_{14}\text{B}$ compound. The total magnetic moment of the compound is the sum of the contributions from the iron and neodymium sublattices.

Magnetocrystalline anisotropy

Phenomenologically the magnetocrystalline anisotropy is described by an anisotropy energy, E_A in a magnetic material. For a crystal with uniaxial symmetry, that is, hexagonal or tetragonal, it may be expressed as

$$E_A(\theta) = K_1 \sin^2 \theta + K_2 \sin^4 \theta + \dots \quad (2.10)$$

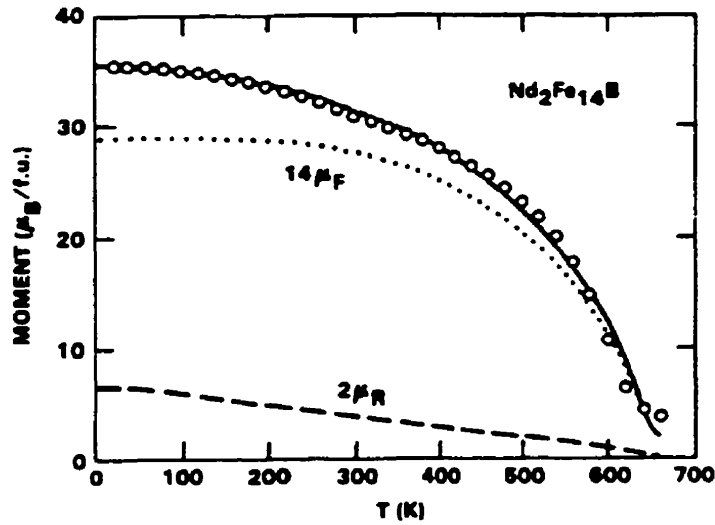


Figure 2.12: Molecular-field analysis by a two-sublattice (iron and neodymium sublattices) model (from [51]) for $\text{Nd}_2\text{Fe}_{14}\text{B}$. Open circles denotes the measured moment per formula unit. The solid line is the calculated total moment, which is the sum of the iron (dotted line) and neodymium (dashed line) contributions.

where K_1 and K_2 are the anisotropy constants and θ is the angle between the symmetry axis (c -axis) and the spontaneous magnetization. In equilibrium the anisotropy energy must be minimized at a specific angle θ_{EMD} , the so-called easy magnetization direction (EMD), determined by the combination of K_1 and K_2 . For permanent magnet materials, however, K_1 usually predominates and the easy magnetization direction is therefore determined by K_1 . For $K_1 > 0$, $\theta_{EMD} = 0$ corresponds to a uniaxial anisotropy and, for $K_1 < 0$, $\theta_{EMD} = \pi/2$ a planar anisotropy.

Another commonly used quantity for the description of the magnetocrystalline anisotropy is the anisotropy field, H_A , which is defined as the field necessary to rotate the magnetization from the easy to the hard direction and is given by

$$H_A = \frac{2K_1 + 4K_2}{\mu_0 M_s} \quad (2.11)$$

where M_s is the saturation magnetization.

Magnetocrystalline anisotropy generally results from the spin-orbit coupling and the Coulomb interaction of an atom with its environment. It is obtained by summing the contributions from all the single ions or atoms in a crystal and of course depends on the symmetry of the crystal structure. The crystal field theory is widely used to theoretically deal with the magnetocrystalline anisotropy. With this theory, the

macroscopic anisotropy described by the anisotropy constants K_1 and K_2 can be related to the crystal field parameters. In the R-T compounds for permanent magnets, the contribution of the R sublattice usually is an order of magnitude larger than the T sublattice anisotropy¹ and the macroscopic anisotropy is thus determined by the rare earth atoms and the theory gives[5]

$$K_1 \cong \frac{3}{2} \alpha_J \langle r^2 \rangle A_2^0 \langle O_2^0 \rangle \quad (2.12)$$

where α_J is the second-order Stevens factor, $\langle r^2 \rangle$ is the average over the $4f$ radius for the rare earth atoms, A_2^0 is the second-order crystal field parameter and $\langle O_2^0 \rangle$ is the thermal average of the second-order Stevens operator. The Stevens operator is related to the angular momentum and, in case where the exchange interaction dominates the crystal-field, its “fully-stretched” (ground state) value $\langle O_2^0(|J_z| = J) \rangle$ is positive. The sign of K_1 is thus determined by the sign of A_2^0 and α_J . A_2^0 is determined by the crystal structure of a given R-T compound. The value of α_J reflects the shape of the $4f$ orbitals. For Sm, Er and Tm, α_J is positive, which means that their $4f$ orbitals look like a cigar (or a rugby ball), whereas the other rare earths have a negative α_J , which means that their $4f$ orbitals are disc-like. Therefore in the case of rare earth dominated anisotropy, the R-T compound of a specific crystal structure for R=Sm, Er and Tm has a magnetocrystalline anisotropy different from other R elements.

2.2.2 Interstitial modification of R_2Fe_{17} properties

The Curie temperature (T_c) of the R_2Fe_{17} system is typically low, around room temperature, whereas T_c for α -Fe is about 770 C. The low T_c reflects the weak exchange interaction as expressed in Eq. 2.9. This may reflect the short Fe-Fe distances at the dumb-bell sites (for the dumb-bell sites, see Section 2.1.1). It is well known that the exchange interaction critically depends on the interatomic distance. From the classic Néel-Slater curve (Fig. 2.13), the exchange integral for Fe-Fe is negative (anti-ferromagnetic) when the Fe-Fe spacing is less than 2.5 Å. The Fe-Fe distance is typically 2.4 Å at the dumb-bell sites, they therefore interact negatively[52]. The

¹Only at high temperature the T sublattice is dominant because of the rapid decrease of the R sublattice anisotropy with increasing temperature.

negative interaction at the dumb-bell sites weakens the overall positive exchange and lowers the Curie temperature.

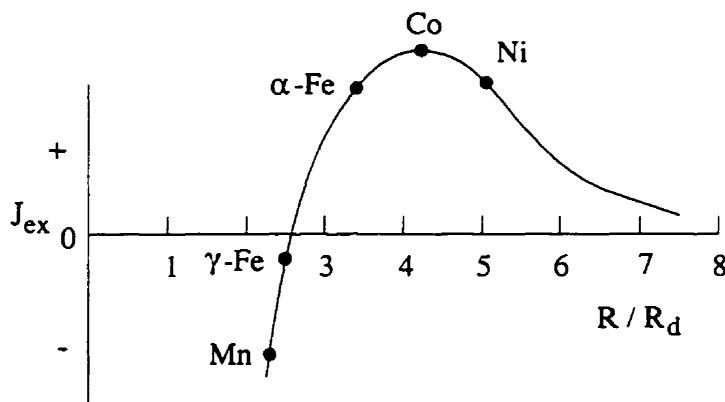


Figure 2.13: A variation of the exchange integral, J_{ex} , as a function of the ratio of the inter-atomic distance, R to the radius of d-shell, R_d . Solid line is the Néel-Slater curve (from [53])

The easy magnetization direction of R_2Fe_{17} systems lies in the basal plane for the whole temperature range except for Tm_2Fe_{17} , in which a change of the easy magnetization direction to c -axis below 80 K was reported[52]. The anisotropy constant K_1 for Tm is 2.3×10^6 J/m³ as deduced from the ¹⁶⁹Tm Mössbauer measurement[54], which is the same as the absolute value of $K_1 = -2.3 \times 10^6$ J/m³ found for the Fe sublattice contribution for the 2-17 system (determined from Y_2Fe_{17} [55])¹. As seen from Section 2.2.1, $K_1 > 0$ corresponds to a uniaxial anisotropy, while $K_1 < 0$ a planar anisotropy. The change of the easy magnetization direction is therefore due to the competition between Fe and Tm sublattice. Sm and Er in the 2-17 structure should have the similar magnetic anisotropies. However, these anisotropies are lower than that of the Fe sublattice, the overall anisotropy being planar consequently. For other rare earths, both the Fe and rare earth sublattices have planar anisotropies.

The introduction of a large amount of interstitial atoms, nitrogen or carbon, drastically increases the Curie temperature of the 2-17 systems (T_c is roughly doubled by the absorption of nitrogen). Since the increase of iron moment in the interstitial 2-17 system is rather small ($\leq 10\%$), the enormous increase essentially reflects

¹Yttrium is considered as a rare earth element. However it does not have the 4f electrons and, hence, is non-magnetic. Therefore, the magnetic properties of an yttrium-iron compound is commonly considered to reflect those of the iron sublattice.

the distance dependence of the exchange interaction between Fe atoms. The average Fe-Fe distance is expanded by the insertion of interstitial atoms and exchange interaction is consequently enhanced (see Fig. 2.13). It was determined that, for $\text{Gd}_2\text{Fe}_{17}$, $J_{\text{FeFe}}=2.64\times 10^{-22}$ J and $J_{\text{GdFe}}=-1.86\times 10^{-22}$ J. After full carbiding the $\text{Gd}_2\text{Fe}_{17}$ carbide has $J_{\text{FeFe}}=6.08\times 10^{-22}$ J and $J_{\text{GdFe}}=-1.12\times 10^{-22}$ J[56]. J_{FeFe} is more than doubled in the carbide, a significant increase.

The presence of nitrogen or carbon in the interstitial sites of the 2-17 structure (which has 2 rare earth neighbors, see Fig. 2.5) significantly modifies the electronic structure of the rare earth atoms. The absolute value of the second-order crystal field coefficient A_2^0 in Eq. 2.12 is greatly increased. In case of $\text{Sm}_2\text{Fe}_{17}$, $A_2^0=-20 \text{ Ka}_0^{-2}$ for the binary compound, while $A_2^0=-300 \text{ Ka}_0^{-2}$ for its nitride and $A_2^0=-450 \text{ Ka}_0^{-2}$ for its carbide[56] (here K is Kelvin and a_0 is Bohr radius). An extremely strong uniaxial anisotropy is developed upon nitriding or carbiding. The anisotropy field H_A was measured to be in the range of 14-26 T at fully nitriding or carbiding[57, 58, 59].

2.2.3 The extrinsic properties

Good intrinsic properties are necessary, but not sufficient, to ensure a good magnet. The performance of a permanent magnet depends on its extrinsic properties. Important extrinsic properties for a permanent magnet include the coercivity H_c , remanence M_r and energy product $(\text{BH})_{\text{max}}$. The definitions of those quantities are based on the magnetic hysteresis loop of the magnetic material as illustrated in Fig. 2.14. The wider the hysteresis loop the harder the magnet. The quality of a permanent magnet is evaluated according to the demagnetization curve (the second quadrant of a hysteresis loop) because a permanent magnet always experiences a demagnetizing field even at a zero external field (self-demagnetization).

The effect of self-demagnetization can be understood by considering a bar magnet, as shown in Fig. 2.15. The lines of the magnetic induction \mathbf{B} go from the north to the south pole outside the magnet, while the magnetization, \mathbf{M} , inside the magnet is directed from the south to north pole. Because of the discontinuity of the normal component of the magnetization at the surfaces of the magnet poles, there is a demagnetizing field, \mathbf{H}_d , in a direction opposite to the magnetization direction inside the bar magnet. Thus the magnetic induction produced by the magnet is given by

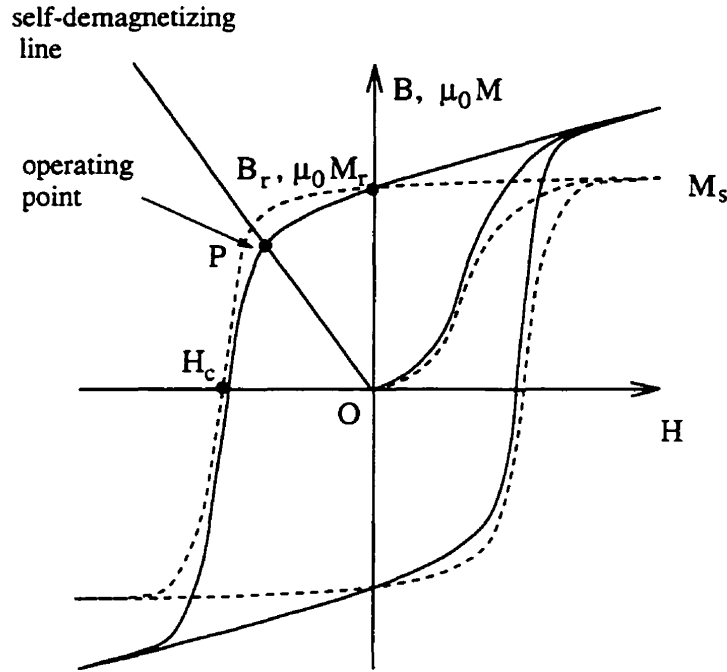


Figure 2.14: A typical hysteresis loop for a hard magnetic material plotted in either B-H or M-H coordinate. $B = \mu_0(H+M)$. Solid lines are for the B-H and dashed lines for the M-H relations. When a material is initially at a demagnetized state, its magnetization M and magnetic induction B is zero in zero applied field $H=0$, i.e. the origin of the coordinate O . It is magnetized by applying a positive (magnetization) field, and an initial magnetization curve is traced out (OA). At sufficiently high fields the magnetization reaches a constant value, the saturation magnetization. As the field is reduced to zero, M does not retrace the initial curve, but decrease more slowly. At zero applied field, M has a non-zero value, known as the remanence M_r . If a sufficiently large field is applied opposite in direction to the initial magnetization (demagnetizing field), M is reduced to zero. The magnitude of this field is the coercivity H_c . "OP" illustrate a typical demagnetizing line of a permanent magnet in operation as determined by the magnet's self-demagnetizing field. "P" is thus the operating point of the magnet as determined by the intersection of its demagnetization line with its hysteresis loop.

the equation

$$B = \mu_0(M + H_d). \quad (2.13)$$

The self-demagnetizing field, H_d , depends on the shape of the magnet and is, for a homogeneously magnetized sample, expressed by

$$H_d = N_d M, \quad (2.14)$$

where N_d is a geometric factor (the demagnetizing factor) and ranges between zero and one. Substituting Eq. 2.14 into Eq. 2.13 yields

$$B = \mu_0(1 - N_d)M. \quad (2.15)$$

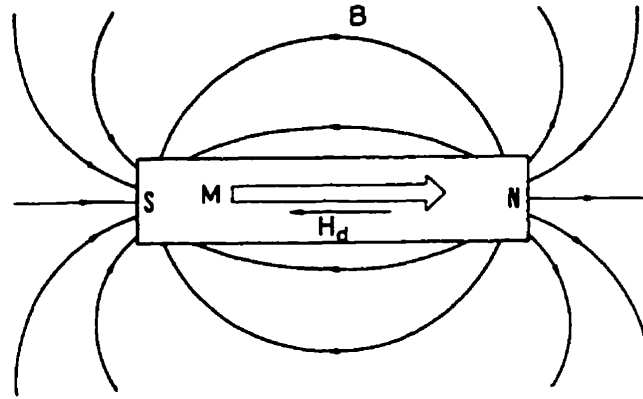


Figure 2.15: Magnetic induction B , magnetization M and the self-demagnetizing field H_d for a bar magnet.

The above expression shows the relationship between the magnetic induction, produced by the magnet in operation, and the magnetization of the magnet. As illustrated in Fig. 2.14 the operating point “P” is determined by the intersection of the self-demagnetizing line with the hysteresis loop. They will change when the magnetization of the magnet changes during operation. In a practical application, a permanent magnet usually operates under a large self-demagnetizing field (corresponding to a large demagnetizing factor) in order to produce high magnetic induction. This requires a high coercivity, a large remanence and a square demagnetization curve. The energy product $(BH)_{max}$ is commonly used to evaluate the quality of a permanent magnet. It is defined as the maximum product of the magnetic induction B and the applied field H in the second quadrant of the B - H hysteresis curve, as illustrated in Fig. 2.14. The energy product reflects the combination of the coercivity, remanence and squareness of the demagnetization curve; it is therefore a convenient measure of the power of a magnet.

These extrinsic properties critically depend the microstructure of a material. In general, the remanence and the squareness can be improved by the alignment of the easy magnetization direction¹ of all of the grains within the bulk of the material. That is, the bulk material is made to be magnetically anisotropic. Whereas to improve the

¹The easy magnetization direction is the one in a magnetic crystal along which the spontaneous magnetization is aligned.

coercivity nucleation and/or growth of domains¹ of reverse magnetization has to be suppressed, which depends on the details of the microstructure.

In a rare earth based permanent magnet, high coercivity originates from the high magnetocrystalline anisotropy of a hard magnetic phase, such as $\text{Nd}_2\text{Fe}_{14}\text{B}$ and $\text{Sm}_2\text{Fe}_{17}(\text{N,C})_x$. In that hard magnetic phase, magnetization in the crystal is along the c axis of its tetragonal or hexagonal unit cell. Demagnetization in such material is realized by rotating the magnetization by 180° . The high magnetocrystalline anisotropy provides a high energy barrier to the rotation. However, having a high magnetocrystalline anisotropy is only a prerequisite for a high coercivity. The microstructure of the material determines the mechanism of the coercivity. Even for the same magnetic phase, different microstructures may lead to different coercivity mechanisms[5, 60, 61, 62]. There are two coercivity mechanisms in general. In the first one, the coercivity is controlled by the nucleation of domains with reverse magnetization. The demagnetizing field required for the nucleation is commonly referred to as the nucleation field. The nucleation is considered to occur on grain boundaries where a large magnetic inhomogeneity favors the formation of the nuclei. The second coercivity mechanism involves domain pinning. In this mechanism, the domain wall is pinned by magnetic inhomogeneities. Effective pinning centers are those that have a size similar to the domain wall width, which is only a few inter-atomic distances for rare earth based permanent magnet materials. The demagnetizing field required for depinning the walls from those pinning centers is described as the depinning field, or propagation field. An important concept related to the coercivity is the idea of single domain grains. In a single-domain crystal, the grain sizes are made to be very small so that domain walls inside the grains are eliminated. There is a critical single-domain size, D_c , of the grains, below which formation of a domain wall is energetically unfavorable and above which a multidomain configuration is stable (see [63]). As an example, the critical single-domain size is about $0.3 \mu\text{m}$ for $\text{Nd}_2\text{Fe}_{14}\text{B}$. In a single-domain crystal, the magnetization reversal (demagnetization) involves nucleation and subsequent growth of domains of reverse magnetization. High

¹In a magnetic material below its Curie temperature, each grain in the material is divided into one or more regions spontaneously magnetized in the easy magnetization direction. These regions are known as (magnetic) domains and are separated by domain walls.

coercivity is achieved by preventing these two processes from occurring even under a large demagnetization field. The coercivity is determined by one of the processes which requires a higher demagnetizing field. In nucleating such a domain, an energy increase induced by the formation of a domain wall is overcome with the assistance of a demagnetizing field. The energy increase becomes relatively high with a decrease in the grain size and hence the nucleation requires a higher demagnetizing field for smaller grains[64]. The growth of reverse domains may be hindered by the pinning of domain walls by a high density of magnetic pinning centers. It is believed that grain boundaries are strong pinning centers for domain walls and high coercivities can be achieved in nanocrystalline materials with high density of grain boundaries[65, 66, 12]. Therefore, high coercivity may be achieved by reducing the grain sizes for either the nucleation-type or pinning-type magnet. This is essentially the main reason that we investigate fine-grain $\text{Sm}_2\text{Fe}_{17}$ carbides throughout the present study.

EXPERIMENTAL METHODS

3.1 A overview of Material Processing by Ball Milling

Ball milling is the major sample preparation method in the present study. It is a mechanical processing method which is now widely used as a nonequilibrium processing tool to produce metastable structures. High energy ball milling was first developed in the late 1960's by Benjamin and coworkers[67] to produce complex oxide dispersion-strengthened alloys for high temperature structural applications. This method, also termed *mechanical alloying*, could successfully produce fine, uniform dispersions of oxide particles which could not be made by more conventional powder metallurgy methods.

A ball milling apparatus usually consists of a container, called the vial, placed in a fast rotating (planetary ball mill) or vibrating frame (shaker mill). Inside the vial, the powder material to be processed, called the charge, is agitated by a number of quickly moving balls which are driven by the rotation or vibration. Both the vial and the balls are made of hard materials, such as hardened steel, tungsten carbide or agate. To minimize wear, the vial and balls are usually made of the same material. The collisions between the balls, or the balls and walls, transfer mechanical energy to the powder trapped in between. Part of the transferred energy is stored in the forms of crystalline defects and atomic disorders. The rest is dissipated as heat.

In the early 1980's an increasing interest in the ball milling method roused partly by the discovery of Koch *et al*[68] that amorphous alloys could be made by mechanical alloying. Since then the ability of high energy ball milling in material processing has been explored extensively and, apart from the uniform dispersions of oxide particles and amorphization, many other effects have been reported to occur from ball

milling, including extended solubility[69], disordering[70, 71], grain refinement[72], quasicrystallization[73], crystallization of amorphous alloys[74, 75, 76], nanocomposite mixing[77, 78], demixing reaction[79] and various chemical reactions, including solid-gas[80, 81], solid-liquid and reduction reactions[82, 83].

The wide scope and application of ball milling are the result of the fact that many processing variables are adjustable, leading to a drastic change in the processing conditions and hence the final products. A few important process parameters are: (1) the milling energy (the impact energy on particles), which may be adjusted in many ways, such as the size and density of the balls, the amount of the charge (usually characterized by the ball-to-material mass ratio) and rotation or vibration frequency; (2) the processing environmental atmosphere and temperature; (3) processing time.

3.1.1 *The process of ball milling*

The central events in ball milling are the ball-powder-ball and ball-powder-wall collisions. In those events, particles are under high stress of complex triaxial type, perhaps partially hydrostatic[84]. Therefore, ball milling is a process where the powder evolves under high mechanically-driven stress. The response of the powder to the stress critically depends on the properties of the powder particles, mostly mechanical properties. The evolution is characterized by irreversible change to the particles from deformation, fracture and coalescence.

Regarding individual particles, ductile particles are repeatedly deformed (sheeted) and/or fractured during ball milling. As a result a large amount of defects, such as new surfaces, dislocations, vacancies and chemical disorder¹, are created. For individual brittle particles, the major events are the fracture of particles to smaller size so that new surfaces are created as well².

The interaction between the particles, under the mechanical driving of ball milling, leads to the coalescence on the particle surfaces and a characteristic morphology is developed³. The morphology in the powder critically depends on the difference in

¹Chemical disorder occurs when the phase is multicomponent, such as an intermetallic phase.

²It has been suggested that brittle-to-ductile transformation may occur at a certain critical particle size so that very small particles may be ductile and deformed plastically[85, 84].

³The new surfaces created during ball milling, however, may chemically react with reactive substances, such as oxygen, nitrogen, leading a direct formation of chemical compounds.

the mechanical properties of particles, *i.e.* whether they are ductile or brittle. The morphology is the most important factor for the interaction between the particles in the powder under ball milling.

3.1.2 Mechanical alloying

In ball milling, mechanical alloying is a most remarkable effect. Literally it denotes a process of forming an alloy by direct reaction, in the solid state, between powder components, or between phases in a powder component¹.

For ductile/ductile components, intensive cold-welding occurs between the surfaces of the sheeted particles to form a composite lamellar structure. For long milling times the lamellar spacing decreases to such an extent that the diffusion paths are drastically shortened and alloying begins, aided by any heating that may be introduced by milling and the enhanced diffusion paths of the lattice defects created by the deformation. The largest body of research work on mechanical alloying concerns the ductile/ductile system (for a review see, for example, [84]). Besides the kinetic factors for a alloying reaction to occur, a thermodynamically favorable situation may also be created in this fine lamellar structure. This structure is a very high energy state due to the contribution from the enormous number of interfaces. The reaction between two adjacent layers involves the destruction of an existing interface surface, leading to a decrease in the total free energy with respect to the two adjacent layers. Due to a high driving force for the alloying reaction², the alloying can therefore far exceed the solubility of the one component in the other. The final product is thus a super-saturated solid solution or an amorphous phase, or a mixture of the two phases. This may be determined by the thermodynamic criterion of minimum total free energy within certain kinetic constraints. The mechanism of mechanical alloying in this ductile/ductile system is very similar to that found in the reaction between thin films of two crystalline metals[86, 87].

¹The term, mechanical alloying, is now used broadly to indicate a ball milling process that provokes structural modification at the atomic level, even for the processes that no significant solid state reaction occurs, for example the phase transformation induced by ball milling.

²The driving force for a transformation reaction is defined as the free energy difference between the initial and final state.

By contrast, fewer studies have been reported on the ductile/brittle or brittle/brittle system. The morphology of the ductile/brittle component is that of small particles of fragmented brittle phase embedded in a ductile matrix. This morphology is less favorable for the alloying reaction both kinetically and thermodynamically. The alloying between the components may, therefore, proceed much more slowly[88]. The morphology of the brittle/brittle component is a granular mixture. Also the contact areas are minimal, although material transfer (the alloying) can occur rather fast between certain brittle components. For example, it was reported[89] that complete alloying reaction between Si and Ge powders could be realized at milling times of 4 to 5 hours. However, the mechanism for mechanical alloying of brittle/brittle systems is not yet well understood. Possible mechanisms which may contribute to material transfer may include the plastic deformation under high energy ball milling or the friction wearing of one powder component.

Mechanical alloying is the ball milling process of a multi-component and/or multi-phase powder. However the ball milling of the powder of a single-phase compound has also shown very interesting results. In fact, the first example of the synthesis of amorphous alloys by ball milling was in the Y-Co and Gd-Co intermetallic compounds, such as YCo_3 and Y_2Co_{17} [90, 91]. In a ball milled powder, the crystalline compound is highly faulted, containing a large amount of various defects in the form of vacancies, dislocations, grain boundaries and chemical disorder. The free energy of the compound is significantly raised due to the presence of those defects. When the total stored energy associated with the defects is higher than the amorphous state, amorphization of the compound occurs. Which defects are controlling the amorphization reaction depends on their contributions to the total free energy, which varies for different alloy systems. For example, in $CuTi_2$ compound, the amorphization is mainly driven by the chemical disorder introduced by ball milling and the contribution from dislocations, grain boundaries and the chemical disorder was estimated to be 1, 2 and 11 kJ/mol, respectively[92]. The mechanism of the chemical-disorder induced is very similar to that found in electron-irradiated intermetallic compounds, where the chemical disorder induced by the electron-irradiation is also the major driving force for the amorphization transformation[93]. In Ni_3Al , however, the energy required

to induce the crystalline-to-amorphous transformation is assumed to be provided by grain boundaries when the size reaches a critical value of 1.5 nm and energy stored in the 1.5 nm-grain compound was estimated to be 23 kJ/mol[70].

The phase transformation of the intermetallic compound induced by ball milling does not necessarily lead to amorphization. It was reported that ball milling of TiSi_2 led to the transformation to a metastable orthorhombic ZrSi_2 -type structure[94] and that ball milling of $\text{Sm}_2\text{Fe}_{17}$ led to a mixture of α -Fe and a Sm-Fe amorphous phase[95].

A number of studies have shown that, given the same ball milling conditions, ball milling of intermetallic compounds generally leads to the same final state as the mechanical alloying of elemental powder mixtures with corresponding compositions[94, 95]. The final product depends only on the average composition of the powder. Therefore, a phase diagram, including the metastable phases produced by ball milling, could be constructed. Analogous to the equilibrium phases, a phase diagram has a thermodynamic origin essentially based on the minimization of the total free energy of a thermodynamic system. Thus, free energy analysis in ball milled systems has been very fruitful in explaining the phase formation in the final product.

3.2 Sample Preparation and Processing

Single phase compounds were used as the starting material for ball milling. The compound ingots were therefore prepared first.

3.2.1 Ingot preparation

Alloy ingots, $\text{Sm}_2\text{Fe}_{17}\text{C}_x$ ($x=0-1$) were prepared in an induction-melting cold crucible under Ar by melting appropriate amounts of the constituents (purity better than 99.9% for Sm and C and 99.99% for Fe). Sm has a very high vapor pressure at high temperature (about 10 torr at its melting point). Therefore an excess amount of Sm is used in the starting composition (corresponding to $\text{Sm}_{2.4}\text{Fe}_{17}\text{C}_x$) to compensate for its evaporation during alloying. Because of the high vapor pressure of Sm and the very different melting points of the constituents (for melting points, Sm:1072 C, Fe:1536 C and carbon:3827 C) a well thought out procedure is needed for the alloying. Typically,

carbon and Sm pieces are added to the Fe melt in sequence. For homogeneity, the alloy was re-melted at least 3 times. The mass loss was about 4% after the meltings due to the evaporation of Sm. The composition of the as-cast alloy was $\text{Sm}_{2.1}\text{Fe}_{17}\text{C}_x$, Sm rich by about 0.5 *at.*% with respect to the stoichiometric 2-17 phase. It was calculated from the final mass of the alloy assuming the mass loss was entirely caused by the Sm evaporation. The as-cast ingot contained a mixture of phases, including α -Fe, 2-17 and other Sm-rich phases, such as SmFe_2 , SmFe_3 or SmFeC .

To obtain single-phase compounds, high temperature annealing was performed subsequently. The $\text{Sm}_{2.1}\text{Fe}_{17}$ ingot was annealed at 1000°C for 48 h and the other ingots, containing carbon, were annealed at 1150°C for 5 h. During the high temperature annealing, the excess amount of Sm in the as-cast ingot evaporated. Thus, after annealing, the alloy was almost single-phase $\text{Sm}_2\text{Fe}_{17}\text{C}_x$ ($\text{Th}_2\text{Zn}_{17}$ -type structure, with carbon in its 9e interstitial sites), containing only a few percent of the Sm-rich phase, SmFe_3 , as detected by both x-ray diffraction and thermomagnetic measurements. The grains in a single phase $\text{Sm}_2\text{Fe}_{17}\text{C}_{1.0}$ compound were between 50 μm and 100 μm as observed by an optical microscope. For the optical microscopy, the sample was polished and etched with a 4-5 *vol.*% HNO_3 alcohol solution.

A series of other R_2Fe_{17} compounds (R=Ce, Pr, Nd, Gd, Tb, Dy, Ho and Er) were prepared for the ball milling process described below.

3.2.2 Ball milling procedure

The single-phase compounds, prepared as above, were used as starting materials for the ball milling process. Ball milling was carried out in a commercial SPEX 8000 mixer/mill. It is a high-energy ball mill apparatus, which operates by shaking the vial in three mutually perpendicular directions at a speed of about 1200 rpm. Two types of ball milling processes was used in the present study.

In the first process, ball milling was carried out at a relatively high energy level. The material was crushed into pieces smaller than 0.5 mm and, together with 2 hardened steel balls of diameter 12.7 mm (8 g each), was loaded into a hardened steel vial and sealed under purified Ar. The charge of the material was 2 g, leading to a ball-to-material mass ratio of 8:1. According to [89], the impact energy in collision

events is close to 0.1 J^1 .

In the second ball milling process, four smaller steel balls (4.0 mm in diameter, 0.25 g each) were used, for relatively-low-energy ball milling. The starting material was coarse powder of about 0.1 mm grains. The charge of the powder was 1 g, corresponding to a ball-to-material mass ratio of 1:1. The impact energy is thus scaled down, by the ball mass, to about 0.003 J.

The ball milling sample was in the form of powder. Fig. 3.1 is a scanning electron micrograph showing a typical morphology of the powder processed by low-energy ball milling. The powder particles have sub-micrometer sizes. Fine powders are very sensitive to air; particularly, the rare earth element has a high affinity to oxygen and nitrogen. Even very small amounts of oxygen or nitrogen in the sample will lead to the precipitation of appreciable amounts of α -Fe and Sm oxide or nitride. To reduce the contamination from oxygen and nitrogen in the course of sample processing and handling, an ultra-clean glove box filled with purified Ar gas was used (for the glove box system, see the following section).



Figure 3.1: A scanning electron micrograph of a $\text{Sm}_2\text{Fe}_{17}$ powder processed by the low-energy ball milling for 2 h. The short bar represents a distance of $1 \mu\text{m}$.

The overall oxygen and nitrogen content in certain samples were measured in a Leco O_2/N_2 analyzer. The starting alloy contained 0.04 wt.% oxygen and 0.02 wt.%

¹Only a fraction of the energy was imparted to powders.

nitrogen. A powder ball milled for 10 h contained oxygen and nitrogen at 0.40 wt.% and 0.18 wt.%, respectively. The contamination comes mainly from the ball milling process. In the ball milled powder subsequently annealed at 1000°C for 1 hour, the oxygen and nitrogen contents were 0.31 wt.% and 0.15 wt.%, respectively. The noticeable decrease of the contaminants after the annealing process reflects a certain degree of outgassing of the dissolved gases. The oxygen and nitrogen contamination is negligible for the present study.

3.2.3 *Melt spinning*

Complementary to ball milling, rapid quenching was used for sample preparation. The as-cast ingot, Sm rich by about 0.5 at.% with respect to the stoichiometric 2-17 phase, was used for the melt spinning process. Fig. 3.2 is a schematic diagram of the apparatus used for the single roller melt spinning process.

In the process, the ingot (about 1 g) was rf-induction melted in a quartz tube under ~ 17 kPa helium atmosphere and ejected out of the tube through an orifice (~ 0.5 mm in diameter) onto a rapidly spinning copper wheel under an argon overpressure of ~ 100 kPa. The spinning wheel was used to continuously and rapidly conduct the heat away from the melt. The linear surface velocities of the wheel was varied between 5 to 65 m/s. Melt spun ribbons with cross-sections of between 2 to 3 mm in width and 20 to 100 μm in thickness were obtained. The faster the spinning speed the smaller the cross-sectional area of the ribbons.

3.2.4 *Heat treatments*

In this study, annealing the samples to introduce phase transformation was performed frequently. There are usually two ways to do the annealing: (1) in a thermal analyzer, mostly in a calorimeter, under a flow of ultra pure Ar (purity 99.999%) or (2) in a furnace with the sample sealed in a quartz tube; the quartz tube had been filled with purified Ar inside the glove box (O_2 and H_2O content less than 1 ppm).

In the first method the sample temperature and thermal properties were continuously measured during the annealing. The sample temperature is calibrated precisely by measuring the onset temperature of known thermal events, such as the melting of Sn and Zn. The annealing can be, therefore, controlled precisely in terms of the an-

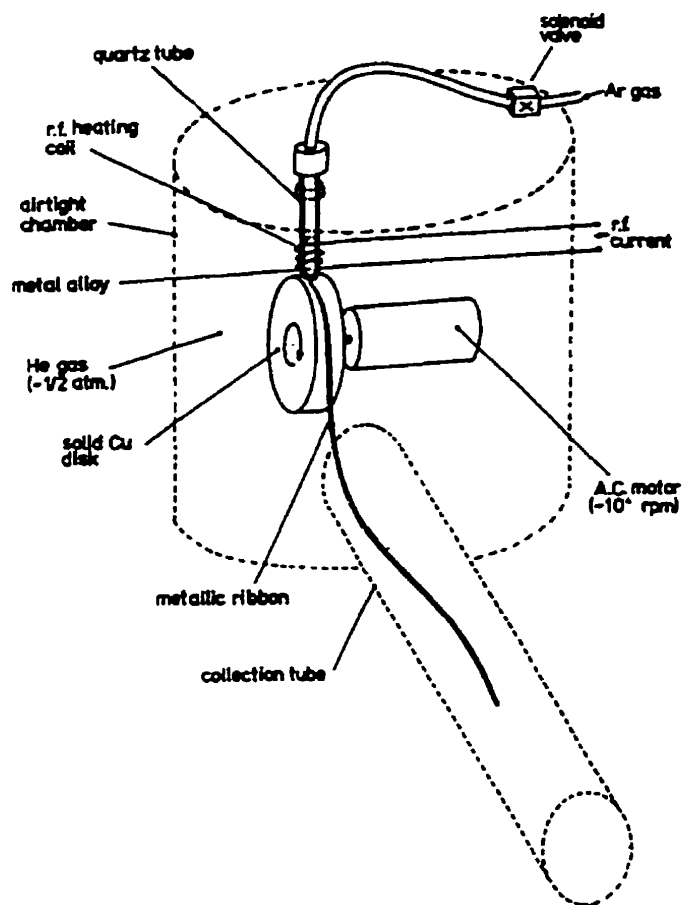


Figure 3.2: A schematic diagram of the melt spinning apparatus.

nealing rate and the end product of the annealing. However the contaminants in the atmosphere are relatively high (the O_2 and H_2O content >10 ppm) and the available temperature is relative low (the calorimeter has a maximum operational temperature of 727 C).

In the second method of annealing, the atmosphere is much cleaner, which is increasingly important for powder samples of finer particles, and the attainable temperature is as high as 1500 C with a high temperature furnace. However the sample temperature cannot be calibrated as precisely as that for the thermal analyzer.

In our studies both methods of annealing were used as they are complementary.

3.3 A simple, high purity glove box

The oxygen and nitrogen content in our samples was effectively controlled at a very low level, usually under 1 at.% (see Section 3.2). For the ball milling powders, the low contamination level was realized by making use of a specially designed Ar-filled glove box with O₂/H₂O concentration less than 1 ppm. Sample handlings were all performed under the ultra-clean Ar atmosphere inside the glove box.

To reduce the cost, the glove box system was in-house constructed by the author with technical assistance. Compared to the commercial product of such a system (about US\$50,000), the cost of our system is much less (less than US\$10,000.). A sketch of the system is shown in Fig. 3.3. The glove box system comprises of two major parts: a glove box, as the working space, and a gas purifier to re-circulate the Ar gas.

For the measurement of the O₂ and H₂O partial pressures in Ar atmosphere, a simple and economical method was established by the author[96] and a brief description of the method is given below. This method is based on the lifetimes of commercial light bulbs in an inert gas.

Commercial light-bulbs of two different brands were calibrated. They were 40 W residential lamps made by the General Electric Company (*GE*) and the Osram Sylvania Inc. (*SA*). The light bulb was opened and its filament placed upright in the glove box¹. The filament was heated to full power, 105-118 V. The temperature of the filament was estimated to be 2000-2100 C.

The lifetime of the filament was measured by a simple electronic logic circuit as illustrated in Fig. 3.4. The filament is in series with a relay coil. When the current through the filament and the coil is turned on, a timer (electric counter or clock) is initiated. Once the filament is burnt, the power for the relay is cutoff and the timer stopped. In this way the lifetime of the filament is recorded. A dimmer is needed for slowly increasing the filament to full power, otherwise direct supply of full power

¹The lifetime of the filament opened in air is slightly shorter (by ~3%) than that when opened in the glove box without air exposure.

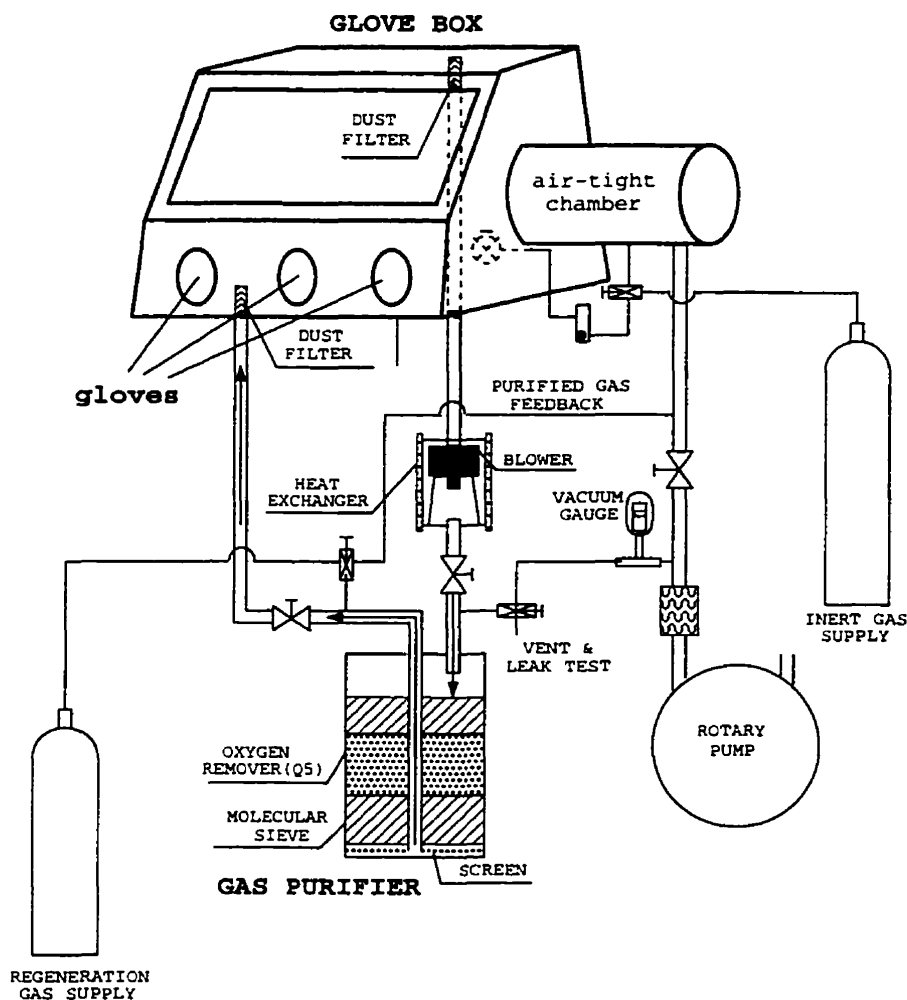


Figure 3.3: A schematic Diagram of the in-house constructed glove box system.

may cause a catastrophic break of the filament at its contact points.

It was found that the lifetime of the incandescent filament is sensitive to certain gas impurities, such as O_2 , H_2O and some hydrocarbons (toluene and hexane), but insensitive to N_2 . The relationship between the lifetime, τ , and the O_2 and H_2O concentrations was carefully calibrated and are plotted in Fig. 3.5. The open and filled symbols are for O_2 and H_2O , respectively.

The calibration curves in Fig. 3.5 clearly exhibit a linear relationship on a log-log scale for both O_2 and H_2O (lines a and b) implying a power-law relationship between

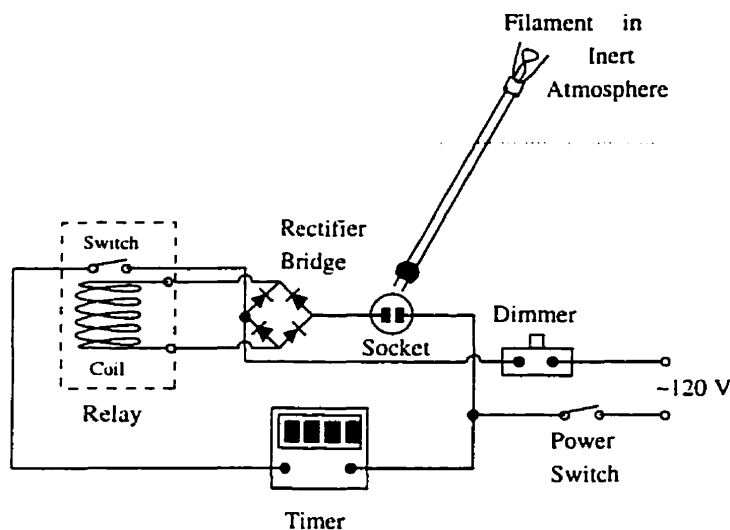


Figure 3.4: Diagram of the electronic logic for recording the lifetime of filament.

the filament lifetime, τ_x ($x = \text{O}_2$ or H_2O), and the impurity concentration, C_x :

$$\tau_x = AC_x^{-\gamma} \quad (3.1)$$

where the unit for τ_x is in seconds and for C_x in ppm. A least-squares fit gives, for $x=\text{O}_2$, $A=3.0 \times 10^{4 \pm 0.09}$ s and $\gamma=0.80 \pm 0.03$. For $x=\text{H}_2\text{O}$, $A=2.0 \times 10^{3 \pm 0.14}$ s and $\gamma=0.78 \pm 0.11$ for both filaments. The simplicity in the power-law relationship is an advantage for the present method. Moreover this method could be used to detect the gas impurities in other inert gases, such as He.

3.4 Powder X-Ray Diffraction (XRD)

X-ray diffraction (XRD) is a well established and reliable method for the analysis of structures and phases. In the present study, it was used extensively for phase identification, lattice constant determination, quantitative phase analysis, microstructure analysis of grain size and strains and determination of disorder in stoichiometric compounds.

X-ray diffraction was performed with an automated Nicolet-Stöe powder diffractometer (model STADI 2/PL, Nicolet XRD Co. Fremont, California) with graphite monochromated CuK_α radiation. Fig. 3.6 is a schematic diagram of the diffractome-

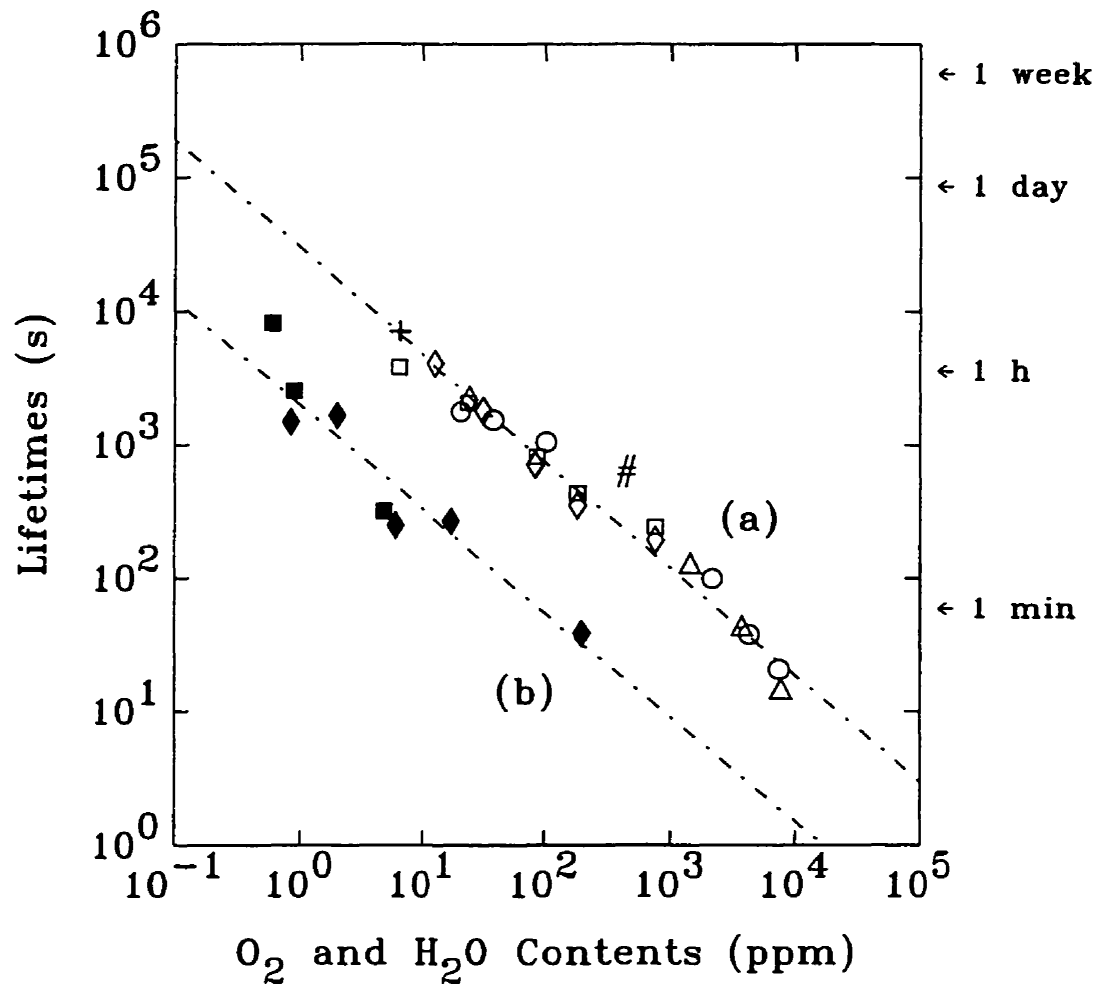


Figure 3.5: Dependence of lifetime of filament on impurity concentrations. The open and filled symbols are for O₂ and H₂O, respectively. For the meaning of the various symbols in the figure see [96].

ter in the non-dispersive reflection geometry which was used for θ - 2θ scans (θ is the angle of the sample plane and 2θ is the elastic scattering angle). The shape of the x-ray beam at the sample is approximately rectangular. The beam is about 10 mm high. The width of the beam at the sample is given by:

$$W = R \times \frac{\sin \alpha \cos 2\theta}{\cos \alpha \sin \theta} \quad (3.2)$$

where $R=179$ mm is the radius of the diffractometer and $\alpha=0.6$ is the equatorial divergence of the incident beam at the sample. The smaller the 2θ , the wider the beam at the sample. The minimum value of interest 2θ in our experiments was 20° , corresponding to $W=9.7$ mm. Accordingly, all XRD samples were prepared

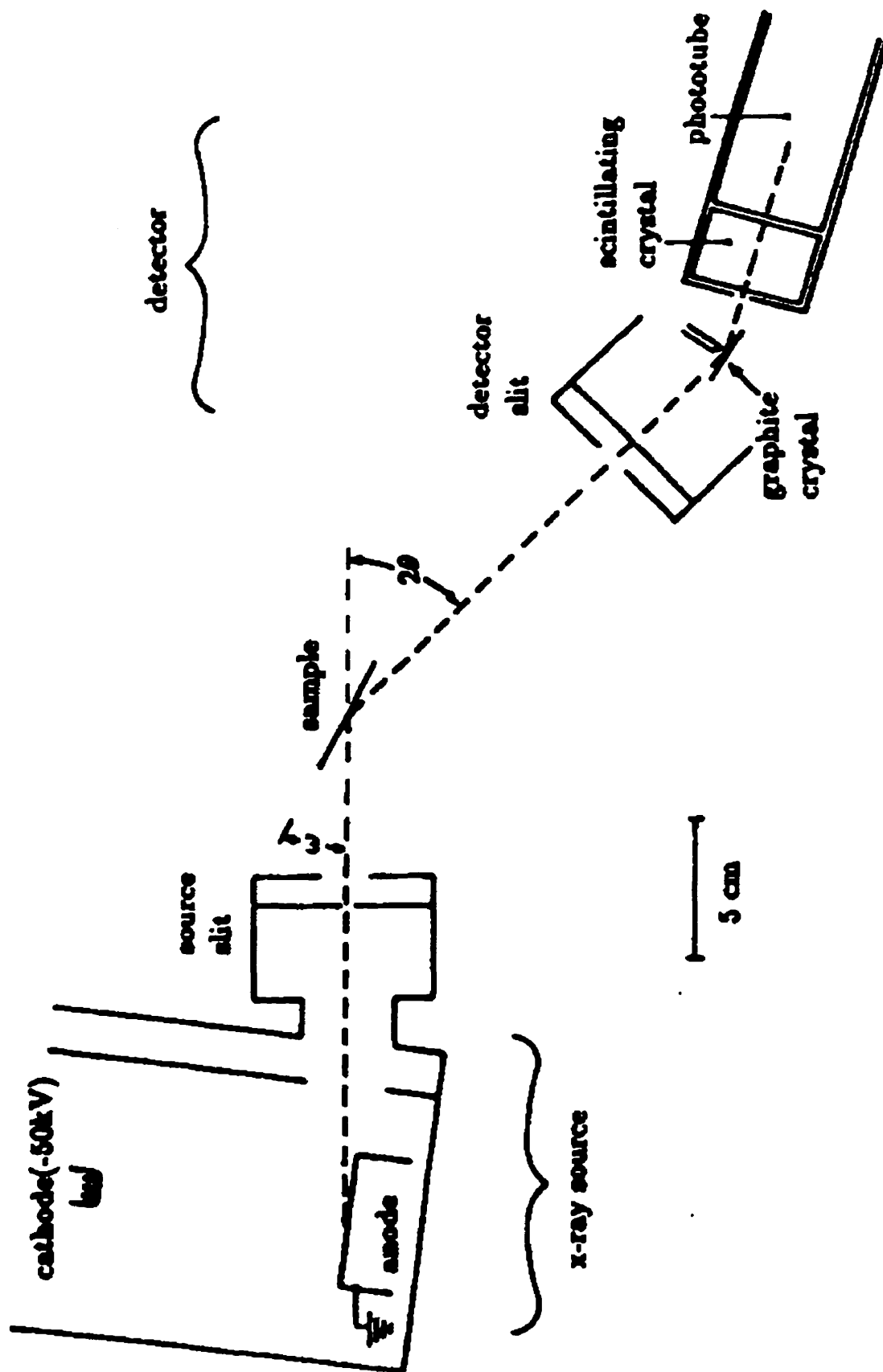


Figure 3.6: A schematic diagram of the x-ray diffractometer.

to be 15 mm wide and 15 mm high to ensure a sample larger than the beam size. The powder for the XRD measurement was ground with a mortar and pestle and smoothly spread on one side of double-sided tape, which in turn is placed on a glass slide (sample mount).

3.4.1 Profile of XRD peaks

Diffraction of x-rays occurs when the x-rays scattered from an object constructively and destructively interfere with each other. The constructive interference gives the diffraction peaks, also called the Bragg peaks. Ideally the peaks should have the shape of delta functions: infinitesimally narrow and infinitely high. Real diffraction peaks, however, only have finite values. For the width of the peak, there are generally two types of broadenings: instrument-related and sample-related broadening. The amount of the instrumental broadening associated with the diffractometer was obtained by scanning a reference sample that has negligible sample-related broadening effects, such as pulverized single crystal Si and well annealed metal powders. The spread of Bragg peaks beyond that due to instrumental broadening is sample-related and usually results from (1) finite grain size and (2) inhomogeneous strain (lattice distortion)¹. The observed peak broadening is the result of convolution of the instrumental and sample broadening. The profile, or the shape, of the XRD peak is determined by the details of the two types of broadenings. Various functions, or combinations of functions, have been proposed to fit the peak profile. The closer the functions to the real profile, the more precise the determination of the grain size and strain. The most widely used functions are the Lorentzian and Gaussian. It is known that the broadening profiles related to instrumental effects and small grained samples are approximately Lorentzian, while the strain broadening is more nearly Gaussian. In the present work, the sum of Lorentzian and Gaussian functions, the so-called pseudo-Voigt function[97], was therefore used for a better fit. The pseudo-Voigt function used to fit the XRD peak is defined as:

$$\Phi(x) = \Phi(0)[\eta L + (1 - \eta)G] \quad (3.3)$$
$$0 \leq \eta \leq 1$$

¹Homogeneous strain is the one that causes an overall expansion or contraction of a lattice.

where L and G are the Lorentzian and Gaussian functions, respectively, and η describes the fraction of the Lorentzian component in the XRD peak. The two limiting cases, $\eta=1$ and $\eta=0$, corresponds to the pure Lorentzian and Gaussian function, respectively. In using the pseudo-Voigt function to model the peak profiles, the half width (that is, the overall width of the profile at half maximum intensity, FWHM), w , was made equal for the Lorentzian and Gaussian function. Therefore the pseudo-Voigt function becomes

$$\Phi(x) = \Phi(0) \left[\eta \frac{w^2}{w^2 + x^2} + (1 - \eta) \pi \ln 2 \exp(-\ln 2x^2/w^2) \right] \quad (3.4)$$

Fig. 3.7 shows the fit for a mechanically alloyed $\text{Sm}_2\text{Fe}_{17}$ powder containing nanocrystalline α -Fe and amorphous Sm-Fe.

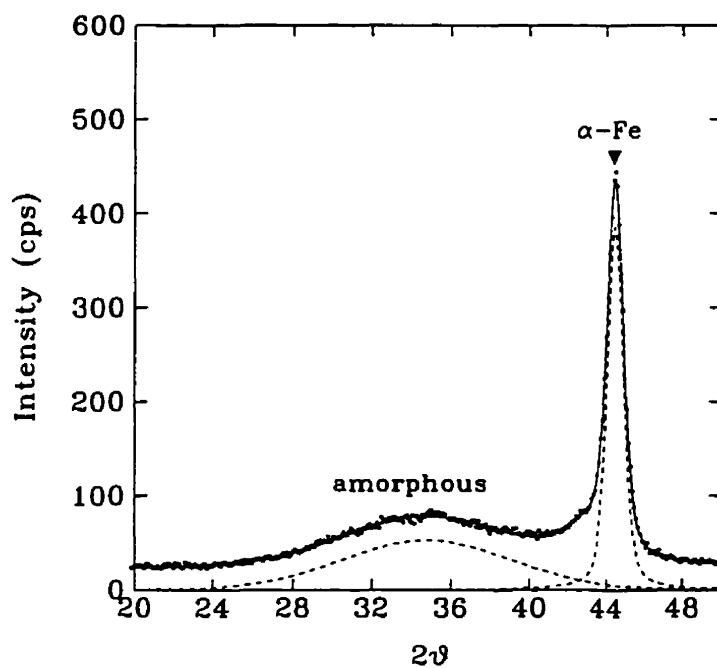


Figure 3.7: An example of a fit for a mechanically alloyed $\text{Sm}_2\text{Fe}_{17}$ powder. The dots are the experimental points, the dashed lines are fitted patterns representing the amorphous phase and the α -Fe phase and the solid line is the overall fitting of the XRD scan.

3.4.2 Analysis of grain sizes and strains

In the analysis of grain sizes and strains the *integral breadth* possesses special mathematical significance. It is defined as the integrated intensity (the area under the

peak) divided by the height of the peak. From this definition, the integral breadth obtained for Eq. 3.4 is

$$\beta = [\eta\pi + (1 - \eta)\left(\frac{\pi}{\ln 2}\right)]w \quad (3.5)$$

The most important reason to use the integral breadth β instead of the easier-to-measure half width w , as defined in Eq. 3.4, is that there are simple relations between the grain sizes/strains and the integral breadth.

Wilson[98] has shown that the 2θ -dependence of strain broadening is given by

$$\beta^{strain} = 4e \tan \theta, \quad (3.6)$$

where e is an approximate upper limit to the inhomogeneous strain[99]. More commonly used the literature is a root-mean-square inhomogeneous strain $\langle \epsilon^2 \rangle^{1/2}$, which is given by

$$\langle \epsilon^2 \rangle^{1/2} = \frac{4}{5}e. \quad (3.7)$$

The 2θ -dependence of grain-size broadening is given by the well-known Scherrer formula[100]

$$\beta^{size} = \frac{\lambda}{d \cos \theta}, \quad (3.8)$$

where λ is the x-ray radiation wavelength ($=1.5418 \text{ \AA}$ for the $\text{CuK}\alpha$ radiation) and d is the average grain size.

Eqs. 3.6 and 3.8 can be significantly simplified in reciprocal space by making the change of variable $\theta \rightarrow s$ according to

$$s \equiv \frac{2 \sin \theta}{\lambda}, \quad (3.9)$$

in which case

$$(\delta s)^{strain} = 2es \quad (3.10)$$

and

$$(\delta s)^{size} = \frac{1}{d}. \quad (3.11)$$

From Eqs. 3.10 and 3.11, it is obvious that a plot of the measured *total* peak broadening $(\delta s)^{tot}$ against s can be used to separate the contributions from the broadening due to grain size and strain, namely

$$(\delta s)^{tot} = \frac{1}{d} + 2es, \quad (3.12)$$

where

$$(\delta s)^{tot} = \frac{2\beta \cos \theta}{\lambda} \quad (3.13)$$

and β is determined from the fitting parameter ω using Eq. 3.5. The slope of the $(\delta s)^{tot}$ - s plot gives the strain and the intersection at $s=0$ yields the grain size. This method was adopted in our studies.

3.5 Thermomagnetometry (TMA)

Thermomagnetometry (TMA) measures the magnetizations of samples as a function of temperature. It was used to determine the magnetic transformation temperature and the formation or demise of magnetic phases.

The thermomagnetometer used in the present work is actually a Perkin-Elmer TGA-7 thermogravimetric analyzer (TGA), with a field gradient in the vicinity of the sample. The field gradient and strength (about 60 Oe at the sample position) was generated by a small "U" shape permanent magnet outside the furnace tube. The arrangement close to the sample area is illustrated in Fig. 3.8. TGA measures the weight of a sample by making use of an electromagnetic balance. It has a high sensitivity (0.1 microgram) and is very stable against vibration and ambient changes. The gradient of a magnetic field exerts an extra force on a magnetic sample, so any change of the magnetization is reflected as a "weight" change. The extra force is thus proportional to the magnetization of the sample¹.

In a typical TMA measurement, the real weight of a sample was measured at the beginning without the magnetic field gradient. This amount of the weight was

¹Notice that magnetization is a vector. The measured magnetization is only the component in the direction of the applied field (about 60 Oe).

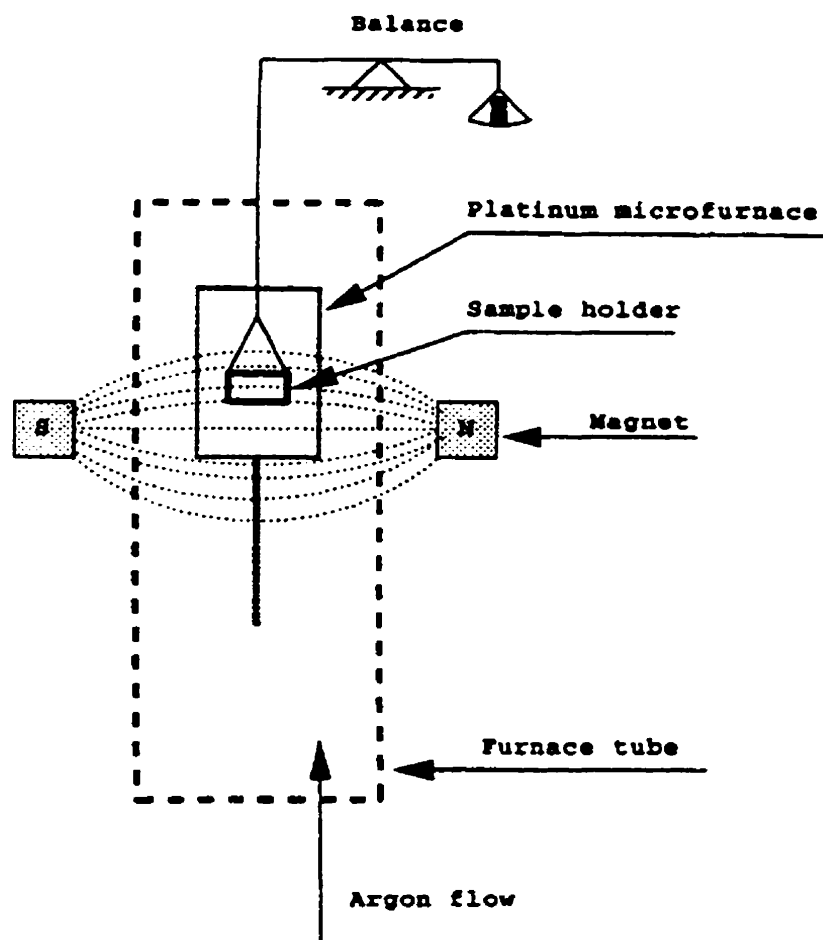


Figure 3.8: A schematic diagram of the thermomagnetometer.

subtracted out by the computer of the analyzer system, leading to a “zero” reading of the sample weight. The field gradient was then introduced by placing the permanent magnet close to the sample (see Fig. 3.8). The measured weight is, therefore, purely magnetic¹ and is proportional to the total magnetization of the sample. Fig. 3.9 illustrates an example of the pattern of a TMA scan. Although only a small amount of the sample (about 2 microgram) was used, the signal was very stable, giving very smooth scanning curves.

As demonstrated by Fig. 3.9, the TMA measurement can be used to estimate the amount of a magnetic phase in a sample, provided that the saturation magnetization of the phases are known.

¹The change of sample mass is negligible during the measurement.

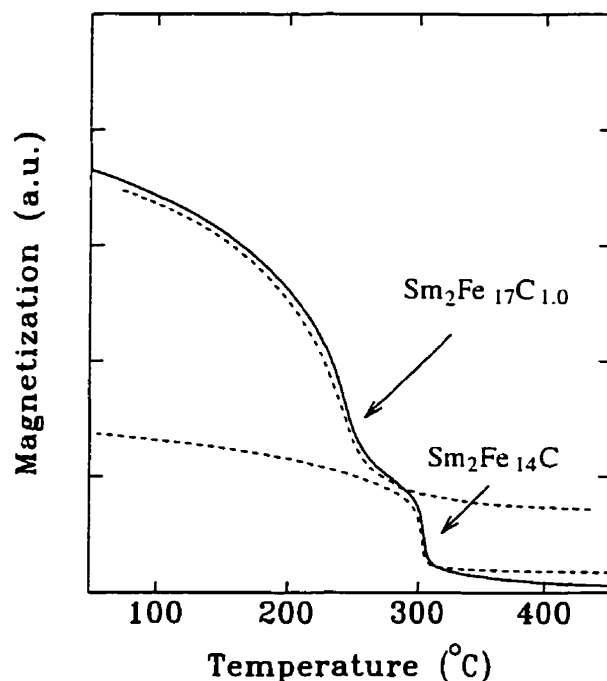


Figure 3.9: An example of a TMA scan of a $\text{Sm}_2\text{Fe}_{17}\text{C}_{1.0}$ powder at a heating rate of 40 C/min (solid line), containing both the $\text{Sm}_2\text{Fe}_{17}\text{C}_{1.0}$ ($\text{Th}_2\text{Zn}_{17}$ structure) and the $\text{Sm}_2\text{Fe}_{14}\text{C}$ ($\text{Nd}_2\text{Fe}_{14}\text{B}$ structure) phase as indicated by their respective Curie temperature in the figure. The volume fraction of the $\text{Sm}_2\text{Fe}_{14}\text{C}$ phase is about 25%. The dashed lines illustrate the magnetizations of a single phase $\text{Sm}_2\text{Fe}_{17}\text{C}_{1.0}$ and $\text{Sm}_2\text{Fe}_{14}\text{C}$ compound respectively. The superposition of the two magnetizations gives rise to the total magnetization (solid line). (For a clearer view, the dashed lines are shifted by 5 C to lower temperature.)

3.6 Differential Scanning Calorimetry (DSC)

When a material undergoes a change in its physical state, such as melting or a transition from one crystalline form to another, heat is absorbed or liberated. A differential scanning calorimeter is designed to determine the enthalpy changes of these processes. In the present study, a Perkin-Elmer DSC-2C, as illustrated in Fig. 3.10, was used. In a typical DSC measurement, the sample and an inert reference are heated at a constant rate, the calorimeter records the electric power required to maintain the sample and the reference at the same temperature. In this way the heat flow in and out of the sample during heating is measured. The enthalpies of transformations and transition temperatures are thus determined.

An example of DSC scans are shown in Fig. 3.11. The transformation to the crystalline $\text{Dy}_2\text{Fe}_{17}$ in a mechanically alloyed $\text{Dy}_2\text{Fe}_{17}$ powder releases heat and gives

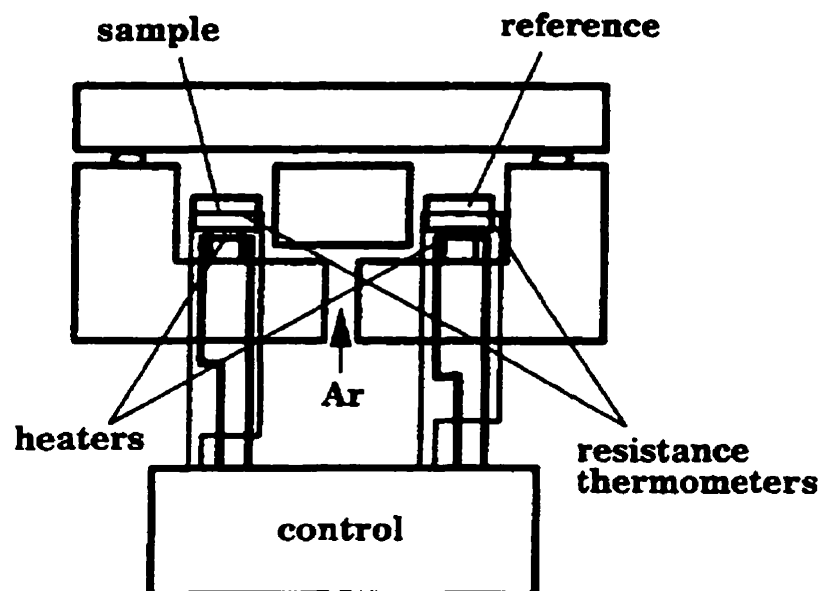


Figure 3.10: A schematic diagram of the DSC apparatus.

rise to a strong exothermic peak as illustrated. The peak shifts to higher temperatures at higher heating rates. The shift of the peak temperature can be used to determine the “activation energy” of the transformation[101, 102].

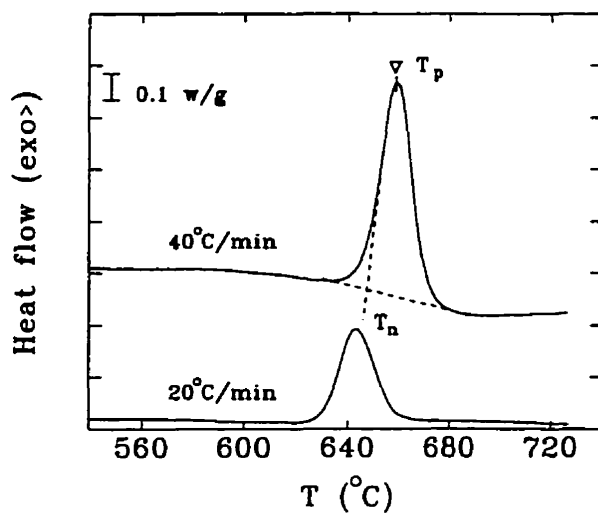


Figure 3.11: An example of DSC scans of a mechanically alloyed $\text{Dy}_2\text{Fe}_{17}$ powder at heating rates of 20 and 40 C/min. The exothermic peaks correspond to the formation of crystalline $\text{Dy}_2\text{Fe}_{17}$ phase. The definitions of the onset temperature T_n and peak temperature T_p are demonstrated as well.

MECHANICAL ALLOYING OF R_2Fe_{17}

In this chapter, phase formation and transformation in mechanically alloyed R_2Fe_{17} and in the subsequently annealed specimens is investigated. Rare earths are quite similar, in many cases, regarding the formation of alloys and compounds with other elements due to their almost identical chemical properties. In the R-Fe alloy systems, corresponding phase diagrams show that there exist four types of equilibrium intermetallic phases. They are R_2Fe_{17} , R_6Fe_{23} , RFe_3 and RFe_2 . The R_2Fe_{17} phase is commonly formed for all rare earth materials reflecting the similarity among different rare earth elements. However, the other three phases are not necessarily formed for all the rare earths. For rare earths heavier than Sm, all the four equilibrium intermetallic phases exist, while for the rare earths lighter than Sm they only form one equilibrium intermetallic phase, R_2Fe_{17} , with Fe. Sm is different: it forms three intermetallic phases with Fe; all those for the heavier rare earths, except the R_6Fe_{23} phase. In terms of the phase formation properties in the R-Fe system, Sm is therefore on the boundary between the light and heavy rare earths although it is usually considered as a light rare earth.¹ In order to provide a general understanding of the phase formation properties in the Sm-Fe alloy system, it is therefore necessary to study the phase formation in a series of mechanically alloyed R-Fe alloys.

4.1 *Mechanical Alloying*

Mechanical alloying was carried out by high-energy ball milling of the single-phase R_2Fe_{17} alloys. The ball diameter was 12.7 mm and the ball-to-material mass ratio was 8:1.

¹Rare earths are generally classified into two categories, light and heavy, according to whether they lie in the first or second half of the series from La to Lu elements.

The 2-17 structure is unstable under the high-energy ball milling. Fig. 4.1 shows the XRD patterns of a Sm_2Fe_{17} alloy as a function of the process time, t_{BM} . Ball milling leads to the decomposition of the Sm_2Fe_{17} phase into a mixture of nanocrystalline α -Fe and amorphous Sm-Fe. After 10 to 20 h of processing, the nanocrystalline α -Fe and the amorphous Sm-Fe become the two predominant phases in the powder. The average grain size of α -Fe is 8.4 nm for the 15 h powder obtained from the x-ray analysis.

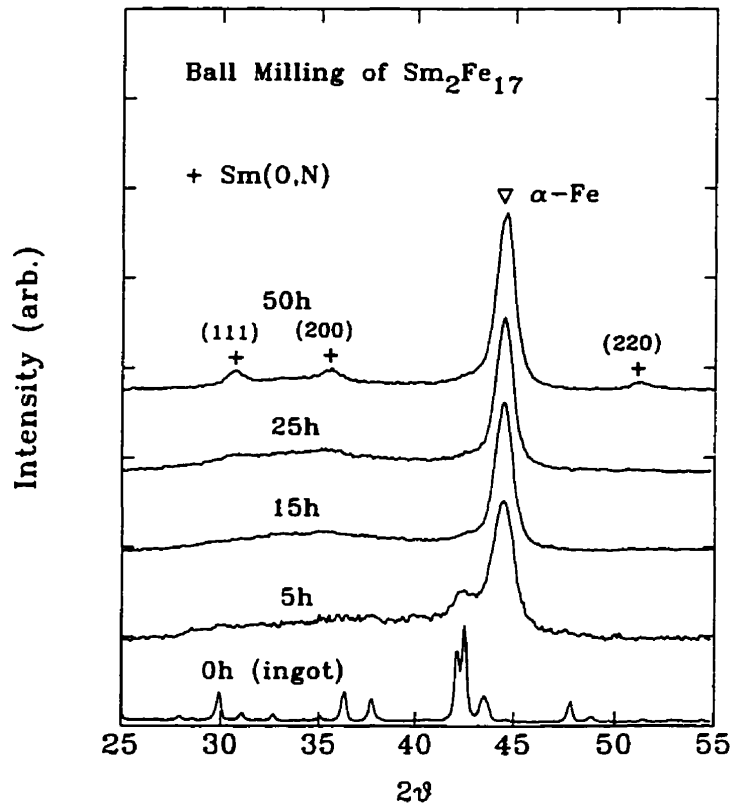


Figure 4.1: X-ray diffraction scans of Sm_2Fe_{17} ball milled for various time periods.

The amorphous phase gives a rather diffuse background in the XRD pattern. An enlarged x-ray diffractogram for the 15 h powder, as shown in Fig. 4.2, gives a clearer view of the XRD pattern for the amorphous Sm-Fe. There is a set of two diffuse peaks, centered at $2\theta = 34.7^\circ$ and 59.7° , which are characteristic of an amorphous structure.

The state of the mixture of the nanocrystalline α -Fe and amorphous Sm-Fe reached by ball milling for 10 to 20 h is a steady-state one. It is relatively independent of

the starting state or the ball milling energy. It has been reported [103, 95, 104] that mechanical alloying of the elemental powders, Sm and Fe, leads to the formation of the mixture of the nanocrystalline α -Fe and amorphous Sm-Fe. In the present study it has been observed that, at a lower energy level, by reducing the ball-to-material mass ratio to 4:1, 20 h ball milling of $\text{Sm}_2\text{Fe}_{17}$ also leads to the steady-state of the two-phase mixture. The steady-state, relatively independent of the starting state and of the ball milling energy, implies that it is related to the properties of the alloy system itself. In section 4.4.2 we will see that the steady-state is essentially determined by the Gibbs free energies of various phases that are accessible in the ball milling processes.

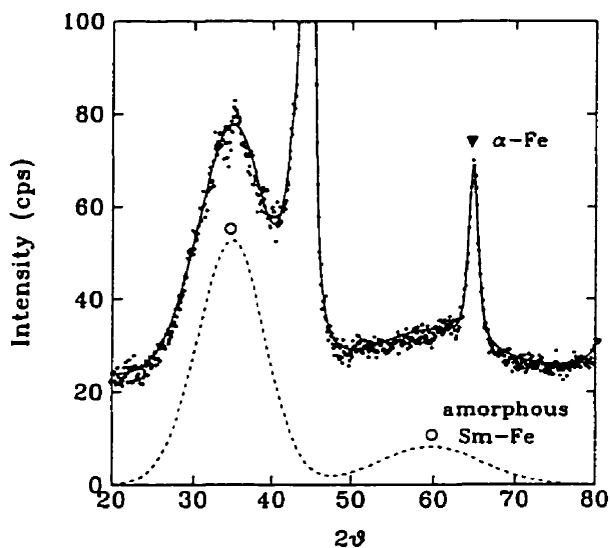


Figure 4.2: An enlarged X-ray diffraction scan for $\text{Sm}_2\text{Fe}_{17}$ ball milled for 15 h (scan (a) in Fig. 4.1). The dots are the experimental points, the dashed line is a fitted pattern representing the amorphous phase and the solid line is the overall fitting of the XRD scan.

At the steady-state the configuration of the state does not change with time. However, for the prolonged ball milling process $t_{BM} > 25$ h a new phase appears in the $\text{Sm}_2\text{Fe}_{17}$ powder, as seen from the XRD measurements in Fig. 4.1 (marked with “+”). This phase is identified as the interstitial oxynitride $\text{Sm}(\text{O},\text{N})$ of the NaCl-type structure (the concentrations of O and N may be smaller than stoichiometric composition [105, 106]). It is formed due to the absorption of a small amount of O and N into the material during the ball milling process. Due to the high affinities of Sm with O and N, the presence of O and N results in the disproportionation of amorphous Sm-Fe forming $\text{Sm}(\text{O},\text{N})$ and α -Fe. The mechanically alloyed powders

were then annealed. In powders prepared by ball milling for less than 25 h, annealing above 600 C leads to the formation of single phase Sm_2Fe_{17} , indicating that the O and N contents are negligible in the powders. In contrast, in powders prepared by prolonged ball milling, the oxynitride $Sm(O,N)$ persists during annealing up to 1000 C. Therefore, it is the absorption of O and N that has destabilized the steady-state (the mixture of nanocrystalline α -Fe and amorphous phase).

Under our ball milling conditions we conclude that the optimum process time t_{BM} is between 15 and 25 h, when the steady-state is reached with negligible contamination by O and N. A series of mechanically alloyed R_2Fe_{17} powders were thus prepared by 20 h of ball milling.

Fig. 4.3 shows a few typical XRD patterns for the R_2Fe_{17} powders mechanically alloyed for 20 h. For Sm and heavier rare earths, the mixture of α -Fe and amorphous R-Fe is the typical product of mechanical alloying, whereas for the lighter rare earths a *fcc*-like phase is formed as indicated by "o" in Fig. 4.3. As shown in the figure, this phase is clearly seen in the Pr_2Fe_{17} powder, while only a trace of it is seen in the Nd_2Fe_{17} powder.

Fig. 4.4 shows the overall fitting of the XRD pattern between $2\theta=20^\circ$ and 55° for the mechanically alloyed Pr_2Fe_{17} powder. Besides the reflections from α -Fe and the *fcc*-like phase, there is a split broad peak (see dashed-line curve in Fig. 4.4), indicating the presence of an amorphous phase as well. The pattern of the split broad peak in the range of $2\theta=20^\circ$ - 55° was not observed for the R_2Fe_{17} powders with $R=Sm$ or heavier, where the typical pattern is as shown in Fig. 4.2. For mechanically alloyed Nd_2Fe_{17} powder, the XRD reflection between $2\theta=20^\circ$ and 55° is more diffuse and weaker than that for other powders. This may be due to the inhomogeneity of the composition in the amorphous phase, as will be discussed in Section 4.4.2. The *fcc*-like phase in the Pr_2Fe_{17} and Nd_2Fe_{17} powders is metastable; it reacts with α -Fe to form 2-17 phase upon annealing above 600 C. The lattice constant of the *fcc* phase is 5.13 nm and 5.10 nm for Pr and Nd, respectively, as calculated from the line positions of the corresponding XRD reflections. The values are in good agreement with those for the high pressure *fcc* Pr and Nd[107]. The *fcc* Pr and Nd observed in this study are thus identified as a high pressure phase. The formation of the high pressure phase during

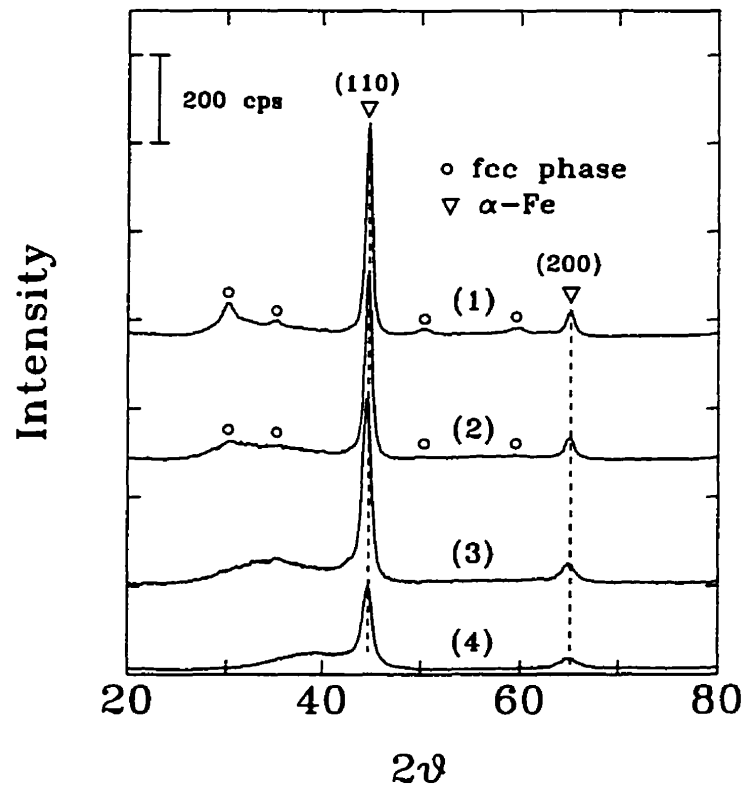


Figure 4.3: X-ray diffraction scans of various R_2Fe_{17} powders ball-milled for 20 hours: R = (1) Pr, (2) Nd, (3) Sm and (4) Dy.

ball milling will be discussed in Section 4.4.1.

Comparing the XRD patterns for the various mechanically alloyed R_2Fe_{17} powders (see Fig. 4.3), we noticed that the reflection intensity from α -Fe is lower for heavier rare earths, indicating correspondingly less α -Fe in the mixture. In mechanically alloyed R_2Fe_{17} for R=Sm or heavier, the mixture has two components: amorphous R-Fe and α -Fe. The decrease in α -Fe therefore implies an enrichment of Fe in the amorphous R-Fe.

The composition of amorphous R-Fe has been estimated from the analysis of the XRD measurements from the weight percent of α -Fe.

The weight percent of α -Fe, $x_{\alpha-Fe}$, is obtained from its relative integrated intensity (I) with respect to that for a pure α -Fe powder (I_0),

$$I/I_0 = \frac{\mu_{Fe}^* x_{\alpha-Fe}}{\mu^*}, \quad (4.1)$$

where μ_{Fe}^* is the mass absorption coefficient of the Cu- K_{α} x-ray radiations for Fe and

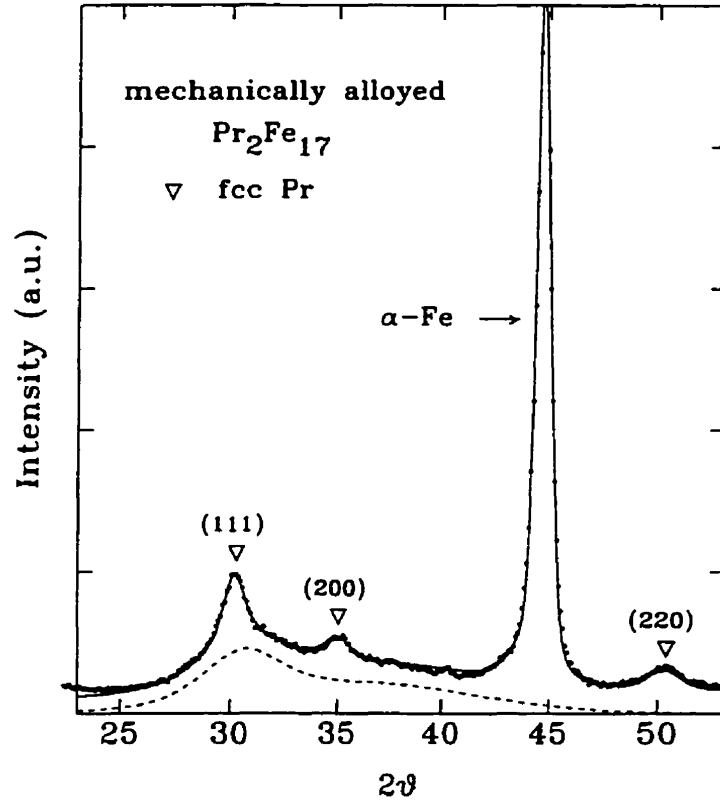


Figure 4.4: Fitting of XRD scan for Pr_2Fe_{17} ball milled for 20 hours. Dots are the experimental data. The solid line is the overall fitting. Besides the α -Fe and *fcc* Pr, two broad peaks, as illustrated by the dashed lines, are needed to fit the pattern.

μ^* is the average coefficient for the R_2Fe_{17} composition.

Combining Eq. 4.1 with the composition-balancing equation for the decomposition

$$0.5R_2Fe_{17} = RFe_z + (8.5 - z) \alpha-Fe, \quad (4.2)$$

we have

$$z = 8.5(1 - I/I_0) - I/I_0 \left(\frac{\mu_R^* m_R}{\mu_{Fe}^* m_{Fe}} \right), \quad (4.3)$$

where μ_R^* is the mass absorption coefficient for R, and m_R and m_{Fe} are the atomic weights for R and Fe respectively. The composition of the amorphous phase in the mechanically alloyed powder is thus estimated using Eq. 4.3 and is listed as Z in Table 4.1. The error in determining the relative intensity of α -Fe, I/I_0 , is about 5%. The resulting error in the estimate of the amorphous composition, Z, is 10%.

In writing Eq. 4.2, we have neglected the solubility of the rare earth in α -Fe. The amount of the rare earth atoms in the α -Fe lattice has been estimated from the lattice

expansion in α -Fe. The lattice constant α -Fe was calculated from the positions of the first two x-ray reflections, that is, (110) at $2\theta=44.67^\circ$ and (200) at $2\theta=65.02^\circ$ for a pure Fe powder. The α -Fe in the mechanically alloyed R_2Fe_{17} powder has a larger lattice constant than the pure Fe powder. The lattice expansion is possibly caused by the substitution of Fe by rare earth atoms, which have larger sizes. The rare earth content in the α -Fe lattice has been calculated, from the measured lattice expansion, to vary between 0.08 at.% (for Pr) and 0.25 at.% (for Ho) with an error of ± 0.04 at.%. The solubility increases with the atomic number of the rare earth. Heavier earth elements have smaller atomic sizes and higher mixing enthalpies with Fe (see the discussion section). As a result, the heavy rare earths have a larger solubility in α -Fe. However, for the analysis of the amorphous compositions, the solubilities of rare earth atoms in α -Fe is negligible.

Apart from the weight percentage of α -Fe, the composition of the amorphous R-Fe may also be estimated from the center position of the corresponding amorphous peak. The position gives an estimation of the average interatomic distance in the amorphous phase using the Ehrenfest relation $R_{nn}=\lambda/1.6267 \times \sin \theta$ [108]. Assuming a close-packed hard sphere model for the amorphous phase, its approximate composition is thus calculated from the average interatomic distance using the corresponding atomic radii. The amorphous compositions have been estimated from the peak positions and are in reasonable agreement with the values listed in Table 4.1.

In mechanical alloying, the mixing of phases occurs on the scale of nanometers. A TEM study on microstructure of the mechanically alloyed Sm_2Fe_{17} (the ball milling conditions are almost identical to the present study) revealed that α -Fe crystallites of about 10 nm are embedded in the amorphous matrix[95, 109]. The crystallite size is too small to resolve the composition of the amorphous region by means of micro-analysis. Using the smallest beam size available in the TEM (15 nm), energy dispersive spectroscopy showed a nearly spatially uniform composition. Quantitative X-ray analysis may therefore be the simplest way to estimate the composition of the amorphous phase in the mechanically alloyed mixture.

Table 4.1: Compositions of amorphous R-Fe in mechanically alloyed R_2Fe_{17} powders obtained from quantitative analysis of x-ray measurements. I/I_0 is the relative (integrated) intensity of α -Fe in the mechanically alloyed mixture with respect to the pure Fe powder; Z is the amorphous composition estimated by using Eq. 4.3.

R	I/I_0	Z
Pr	0.58	$Pr_{15}Fe_{55}^a$
Nd	0.58	$Nd_{50}Fe_{50}^a$
Sm	0.57	$Sm_{43}Fe_{57}$
Gd	0.46	$Gd_{27}Fe_{73}$
Tb	0.43	$Tb_{21}Fe_{79}$
Dy	0.42	$Dy_{21}Fe_{79}$
Ho	0.52	$Ho_{23}Fe_{77}$
Er	0.48	$Er_{21}Fe_{79}$
Y	0.59	$Y_{25}Fe_{75}$

^aCorrected for the presence of the third phase, *fcc* Pr or Nd, the accuracy is lower. The error is estimated to be $\pm 15\%$.

4.2 Post-Annealing of Mechanically Alloyed Sm_2Fe_{17}

DSC and TMA measurements were used to follow phase formation and transformation in mechanically alloyed Sm_2Fe_{17} powders. Fig. 4.5 shows the heating scans at 40 C/min. The structural evolution and phase formation at various stages, indicated by Roman numerals in Fig. 4.5, was followed by performing XRD and TMA measurements on samples heated to the corresponding temperatures followed by fast cooling.

In the as-milled powder, the overall lattice strain and the average grain size in α is 0.62% and 8.4 nm, respectively, as determined from the XRD peak widths. Heating to 300 C only led to the release of the strain in the nanocrystalline α -Fe, the grain sizes remaining the same. The first exothermic peak around 200 C is therefore considered to be related to the strain release. Because of considerable overlap with other DSC peaks, it is difficult to accurately determine the enthalpy enveloped in the first exothermic

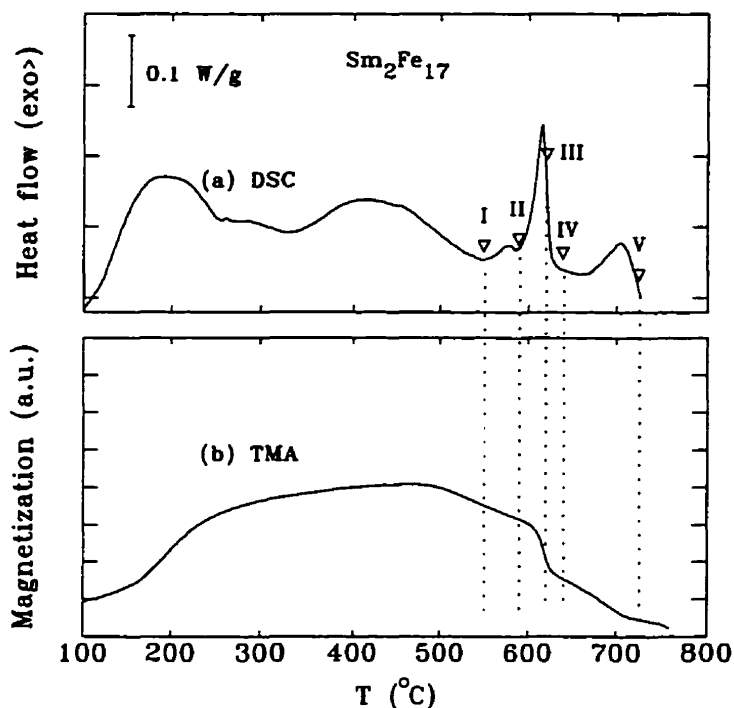


Figure 4.5: DSC and TMA heating scans at 40 C/min for the mechanically alloyed $\text{Sm}_2\text{Fe}_{17}$ powder. TMA data is plotted in an arbitrary unit. The marked temperature points are (I) 540 C, (II) 590 C, (III) 610 C, (IV) 640 C and (V) 727 C. The corresponding XRD patterns are shown in Fig. 4.7.

peak. It is estimated at 2 ± 0.5 kJ/g-atom¹. Considering that the fraction of α -Fe is 33 ± 3 wt.% in the mixture (estimated using Eq. 4.1 and data from Table 4.1), the energy stored in the form of lattice strains in α -Fe is thus 5.1 ± 1.5 kJ/mole. The value is substantially higher than the 1 kJ/mole, reported on the mechanically alloyed pure Fe powders[110] with a magnitude of strains similar to that in the present sample. The discrepancy may come from the reaction between Sm and O. One sample was deliberately exposed to air for a long time, ~ 10 h, before DSC measurement. It was observed that the first exothermic peak was considerably increased, suggesting that oxidation occurs around 200 C. It can be estimated that with even 1 at.%O in the sample the reaction of forming Sm_2O_3 will generate 6.6 kJ/g-atom. The first exothermic peak is thus from the strain release in α -Fe and oxidation of Sm.

The XRD pattern for the 410 C sample in Fig. 4.6 shows that the amorphous peak becomes smaller and a small amount of *fcc* Sm is formed, indicating the on-

¹A g-atom is used to denote a mole of atoms without distinguishing their species. For example, one mole of $\text{Sm}_2\text{Fe}_{17}$ has 19 units of g-atom.

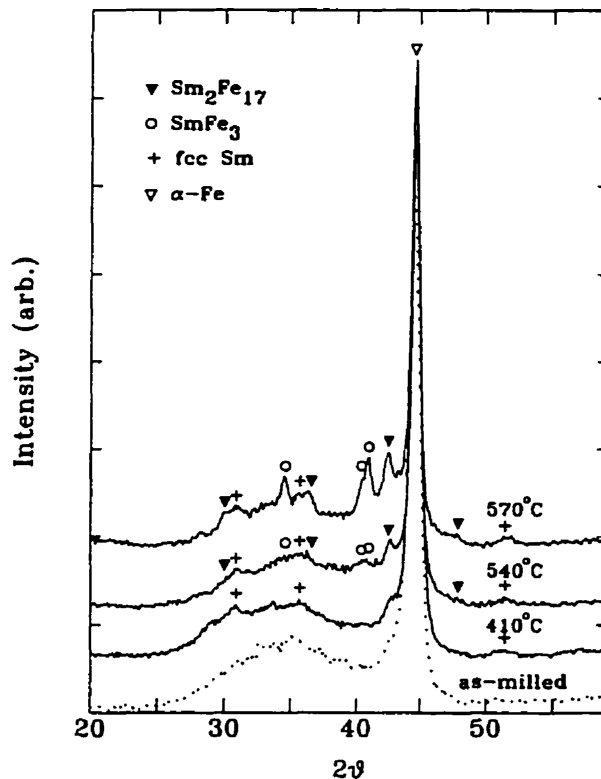


Figure 4.6: XRD scans for the as-milled and post-annealed Sm_2Fe_{17} powders heated to various temperatures. Samples are heated to the corresponding temperature at 40 C/min followed by fast cooling.

set of crystallization of the amorphous phase. The *fcc* Sm is a high pressure phase. The formation of the high pressure phase is possibly due to the effective high pressure sustained by the matrix of the phase mixture[111]. The amorphous phase only partially crystallizes even when heated up to 540 C (see Fig. 4.6) and there is no prominent enthalpy release in the DSC scans up to that temperature except for the first exothermic peak around 200 C. This is because the structural change in the amorphous Sm-Fe proceeds very slowly, as can be seen from the corresponding XRD pattern shown in Fig. 4.6, so that the exothermic peak is broad and weak. Hence the broad peak between 350 C and 550 C is attributed to the structural change in the amorphous Sm-Fe. The integrated area yields ~ -0.9 kJ/g-atom.

Heating to above 540 C results in the formation of $SmFe_3$ ($PuNi_3$ structure) and the high-pressure phase *fcc*-Sm (see the scan for 570 C in Fig. 4.6). The lattice constants of the $SmFe_3$ phase are $a=5.18$ Å and $c=25.0$ Å, as calculated from its x-

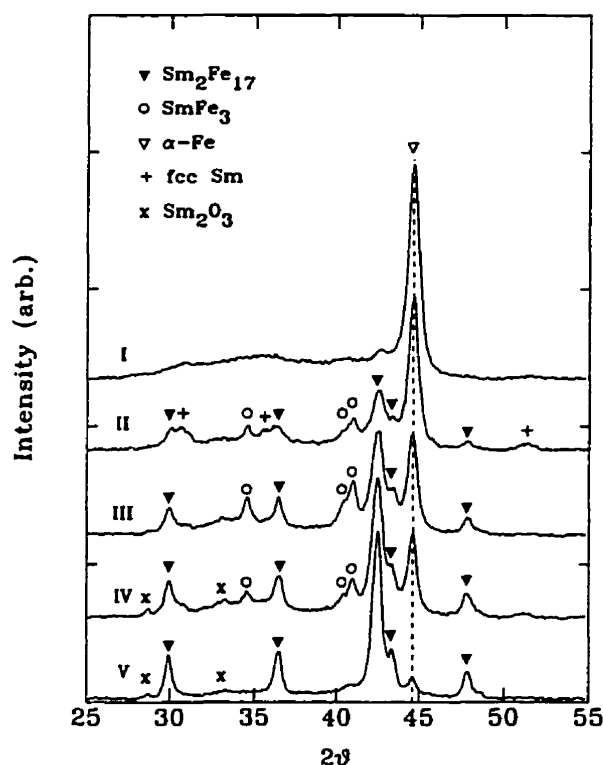


Figure 4.7: XRD scans for the mechanically alloyed $\text{Sm}_2\text{Fe}_{17}$ powders heated to the corresponding temperatures as marked in Fig. 4.5: (I) 540 C, (II) 590 C, (III) 610 C, (IV) 640 C and (V) 727 C. Samples are heated to the corresponding temperature at 40 C/min followed by fast cooling.

ray line positions. The Curie point is 380 C measured by the TMA scans, which agrees with the reported SmFe_3 compound [7]. The amount of SmFe_3 evolved increases with annealing temperature, while the *fcc*-Sm decreases very fast with a corresponding increase in the 2-17 phase and decrease in α -Fe (see scans II and III in Fig. 4.7), suggesting that the *fcc*-Sm is reacting with α -Fe to form the 2-17 compound. The pronounced enthalpy release in the DSC scan and the sharp decrease in the TMA scan around 610 C (see Fig. 4.5) are attributed to this reaction. The 1-3 phase also reacts with α -Fe forming 2-17, but the process is relatively slow. It occurs between 590 C and 727 C (see scans III, IV and V in Fig. 4.7). The decrease in the magnetization between 610 C and 720 C as seen from the TMA scan in Fig. 4.5 is attributed to the reaction of α -Fe with the 1-3 phase. The complete reaction between the SmFe_3 and α -Fe leads to the formation of single-phase 2-17 powder. The minor amount of residual α -Fe seen from the scan V in Fig. 4.7 reflects the precipitation of Fe caused

by the oxidation of Sm during heating in the DSC equipment. A trace of Sm_2O_3 can be seen from the XRD patterns in Fig. 4.7.

From the XRD patterns in Fig. 4.7, one notices that both the 2-17 and the 1-3 phase formed during the heating are *disordered*. Forming the ordered structure is a process of long-range ordering of the atoms. Reasonable kinetics for this process requires a relatively high temperature. Ordering in the 2-17 structure is indicated in Fig. 4.8. Above 800 C, the superlattice reflection (204) of the structure around $2\theta=37.5^\circ$ appears. The superlattice peak becomes stronger as the annealing temperature increases.

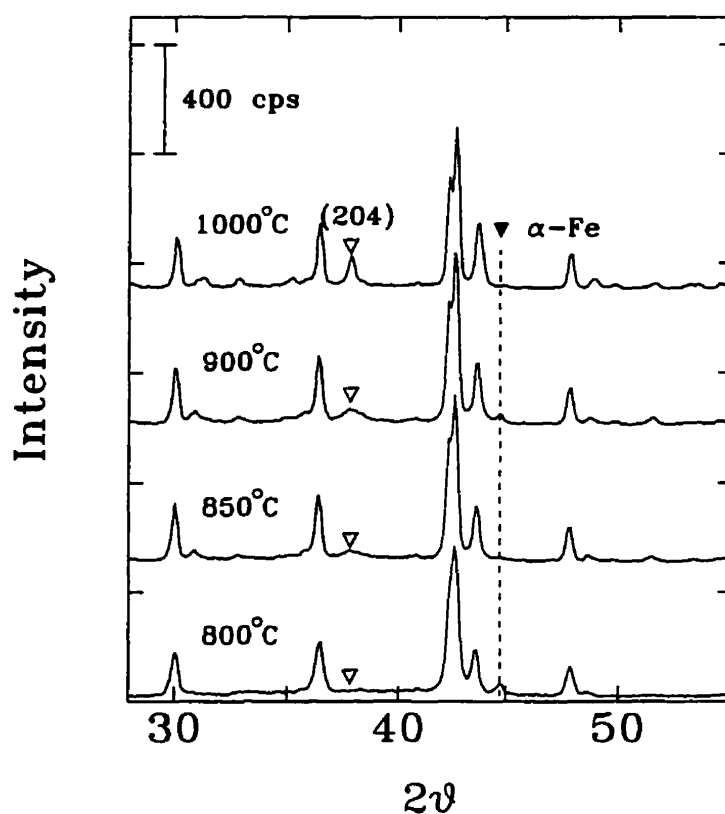


Figure 4.8: XRD scans of mechanically alloyed Sm_2Fe_{17} heated to temperature higher than 727 C, showing the ordering in the disordered 2-17 structure. Samples are heated to the corresponding temperature at 40 C/min followed by fast cooling. The evolution of the superlattice reflection (204) is indicated.

The typical disorder in the 2-17 structure is the random distribution of the dumb-bell Fe pairs. Generally the R_2T_{17} (T=transition metals) structure can be derived from the RT_5 structure (CaCu₅-type) by replacing 1/3 of the R atoms with pairs of

T dumb-bells in an ordered way (see Chapter 2). The disorder occurs when the order in the replacement is disturbed. To describe the disorder in the $\text{Sm}_2\text{Fe}_{17}$ structure, we may define an order parameter as

$$S = 3R_{\text{Sm}} - 2 = \frac{1}{2}(3R_{\text{Fe-pair}} - 1) \quad (4.4)$$

and

$$R_{\text{Fe-pair}} = 2R_{\text{Sm}} - 1, \quad (4.5)$$

where $R_{\text{Fe-pair}}$ is the fraction of the Fe dumb-bell sites occupied by Fe dumb-bell pairs and R_{Sm} is the fraction of Sm sites occupied by Sm atoms. For fully ordered $\text{Sm}_2\text{Fe}_{17}$ we have $S=1$, whereas complete disorder yields $S=0$. The value of S is given by the integrated intensity of superlattice peak (204), I_{204} , as

$$S = \sqrt{\left(\frac{I_{204}}{I_{204}(S=1)}\right)}, \quad (4.6)$$

where $I_{204}(S=1)$ is the integrated intensity for the fully ordered phase. Table 4.2 lists the order parameter as a function of annealing temperature. The evolutions of other important quantities with annealing temperature are determined and listed in the table as well. The $\text{Sm}_2\text{Fe}_{17}$ prepared by annealing at 1100 C for 5 h is the reference as the fully ordered structure.

With an increasing annealing temperature, ordering of the 2-17 has a profound effect on the properties of the phase, most particularly, the Curie temperature, as shown in Table 4.2, which changes of 17%. In the fully ordered $\text{Sm}_2\text{Fe}_{17}$, the Curie temperature is relatively low, $T_c=117$ C (390 K). With increasing disorder, *i.e.* decreasing S , the Curie temperature becomes higher.

In addition to the change in the Curie temperature, the lattice constant ratio, c/a , of the $\text{Sm}_2\text{Fe}_{17}$ phase decreases with the increasing temperature. The decrease in c/a is possibly a direct result of the ordering. As illustrated in Fig. 4.9, the dumb-bell lies along the c -axis of the hexagonal unit cell. The pair distance between the Fe atoms in the dumbbell is 2.38 Å as determined by neutron diffraction and x-ray measurements (see [112] for example). The dumb-bell can be represented by a rod

Table 4.2: The ordering in Sm_2Fe_{17} heated up to the corresponding temperatures (T_a) as shown in Fig. 4.8. Tabulated are the ordering parameter (S) the Curie temperatures (T_c), the lattice constant ratios (c/a) and the domain sizes of the ordered region (d_{DS}). The grain sizes (d_{GS}) are also obtained from the XRD measurements.

T_a (C)	727	800	850	900	1000	1100 ^a
d_{GS}	18 nm	25 nm	45 nm	~76 nm	- ^d	100 μm^c
S	- ^b	- ^b	0.63	0.81	0.88	1
T_c (C)	183	155	138	132	122	117
c/a	1.4638	1.4601	1.4567	1.4556	1.4543	1.4539
d_{DS}	- ^b	- ^b	9.6 nm	7.7 nm	28 nm	- ^d

^a Ingot annealed at 1100 C for 5 h.

^b X-ray reflection too weak to be detected.

^c Size estimated from optical microscopy.

^d Peak broadening too small to be deconvoluted from instrumental resolution of the diffractometer.

4.76 Å (=2×2.38 Å) long, as illustrated in Fig. 4.9, whereas the vertical distance between the rods is only $c'=4.15$ Å, shorter than the length of the rod. As a result, the disorder in the arrangement of the rods may cause the lattice to be stretched along the c -axis of the hexagonal unit cell of the 2-17 structure. Therefore the decrease in c/a may reflect the ordering of the 2-17 structure. The error in determining the value of c/a from the XRD measurement is $\pm 0.01\%$. Comparing the error in determining the lattice constant itself, which is $\pm 0.1\%$, accuracy in determining c/a is an order of magnitude higher. The high accuracy is a benefit of our fitting algorithm which uses the lattice constants, a and c , and corresponding indices to fit the whole XRD pattern.

In the R_2Fe_{17} compound, it has been established that volume expansion, such as the insertion of interstitial atoms, can cause the increase in its Curie temperature. However, during the ordering of the Sm_2Fe_{17} there is no noticeable volume change of the lattice within the experimental error of $\pm 0.2\%$. If the volume of the lattice

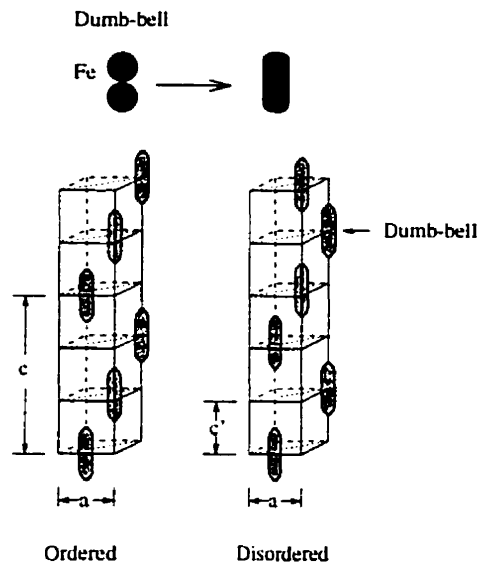


Figure 4.9: The dumb-bell Fe pair may be considered as a rod. In the ordered 2-17 structure, the dumb-bells are arranged in an ordered manner (see Chapter 2 for the structures of 2-17). Disorder may cause the lattice to be stretched along the rod, that is, the c -axis of the hexagonal unit cell of the 2-17 structure. Complete disorder leads to a statistical unit cell same as CaCu_5 , known as TbCu_7 -type structure.

is expanded by 0.2%, the corresponding increase in the Curie temperature is less than 15 C. Therefore there is no noticeable volume expansion to cause the significant increase in the Curie temperature. The pair of Fe atoms in a dumb-bell has the shortest interatomic distance (2.38 Å) in the $\text{Sm}_2\text{Fe}_{17}$ structure. Due to their short Fe-Fe distance, it is believed that the Dumb-bell pairs are mostly responsible for the low Curie temperature of the R_2Fe_{17} compound (see Chapter 2 for more details). Disordering may profoundly affect the magnetic exchange coupling between the Fe atoms in a dumb-bell pair either by direct increase of the Fe-Fe distance or by subtle change of the electronic environment around them so that the Curie temperature is increased. In contrast, it is interesting to note that the Curie temperature for the disordered SmFe_3 phase, $T_c=380$ C, is the same as that for the ordered one within the experimental error. SmFe_3 , similar to $\text{Sm}_2\text{Fe}_{17}$, is a derivative of the RT_5 structure (CaCu_5 -type). The structure is derived by the replacement of 1/10 of the T atoms by the R atoms in an ordered way (see Chapter 2 for the RT_3 structure). In the 1-3 phase there are no Fe dumb-bells and the randomness in the replacement does not therefore change its Curie temperature.

From Fig. 4.8, it is also noticed that, below 1000 C, the superlattice peak is considerably broader than the rest of the 2-17 peaks, suggesting that the domains of the ordered 2-17 are very small. The average size of the domains is estimated from the broadening of the superlattice (204) peak and listed in Table 4.2. In fact below 850 C (corresponding to $S=0.63$) the superlattice peak becomes so broad and weak it can not be detected in the XRD pattern. In contrast, the Curie temperature, T_c , and the c/a ratio is still very sensitive to the annealing temperature below 850 C, suggesting that T_c and c/a are more sensitive measures for the disorder in the 2-17 structure than the order parameter S . Fig. 4.10 shows the relationships between S , T_c and c/a .

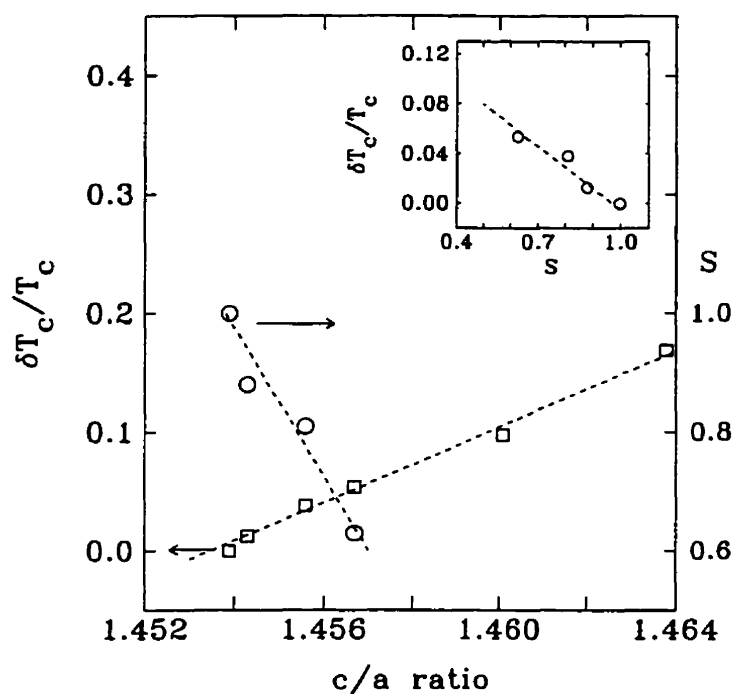


Figure 4.10: Relationships between S , T_c and c/a from the results listed in Table 4.2. It should be noticed that T_c in $\delta T_c/T_c$ is in Kelvin. The dashed lines illustrate the linear relationships expressed in Eq. 4.7.

A least-square fit for the relationship gives

$$\delta T_c/T_c = 0.0075 + 15.857(c/a - 1.4539)$$

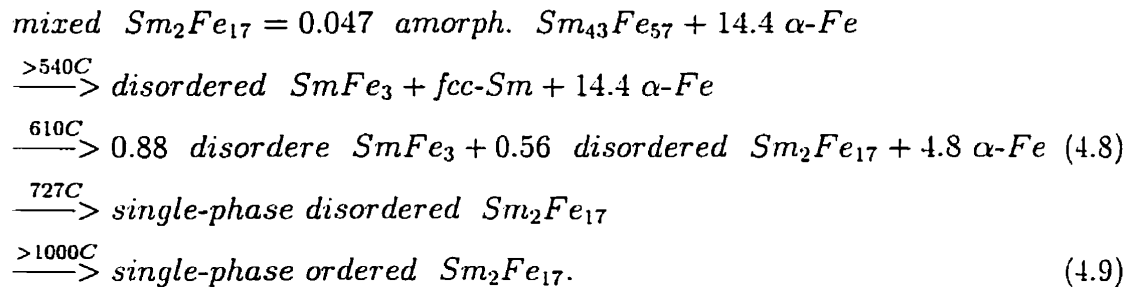
$$c/a = 1.4620 - 0.0080S$$

$$\delta T_c/T_c = 0.165 - 0.170S \quad (4.7)$$

From the above equations we have $c/a=1.462$ and $\delta T_c/T_c=0.165$ (corresponding to $T_c=181$ C) for $S=0$. This value is close to those in Table 4.2 for 727 C, suggesting that the 2-17 structure, annealed at 727 C, is completely disordered. Whereas for 800 C, $S\sim 0.3$ is derived from the corresponding c/a and $\delta T_c/T_c$ in Table 4.2 by using Eq. 4.7, even though the superlattice (204) peak for 800 C is invisible in Fig. 4.10.

The ordering process starts beyond the maximum operating temperature of the DSC equipment. Attempts with a Differential Analyzer (DTA), which operates up to above 1200 C, failed to determine the ordering enthalpy. The DTA has a lower sensitivity than DSC.

To summarize the phase evolution of the high-energy ball milled Sm_2Fe_{17} powders upon heating to various temperatures:



The weight percents of α -Fe and $SmFe_3$ after the reaction between the α -Fe and the fcc -Sm are calculated, from Eq. 4.8, and are 15% and 22% respectively, consistent with the corresponding XRD scan IV in Fig. 4.7.

4.3 Post-Annealing of Mechanically Alloyed R_2Fe_{17}

DSC scans at 40 C/min of a number of the mechanically alloyed R_2Fe_{17} powders are shown in Fig. 4.11. Light rare earths behave very differently from heavy rare earths. Pronounced *endothermic* peaks are observed in the Pr_2Fe_{17} and Nd_2Fe_{17} powders, while for the heavier rare earths, exotherms occur. The results of the DSC measurements on mechanically alloyed R_2Fe_{17} powders are summarized in Table 4.3.

Annealing around the exothermic and the endothermic peaks, as marked in Fig. 4.11, yields single phase 2-17 compounds. These thermal events are therefore related to

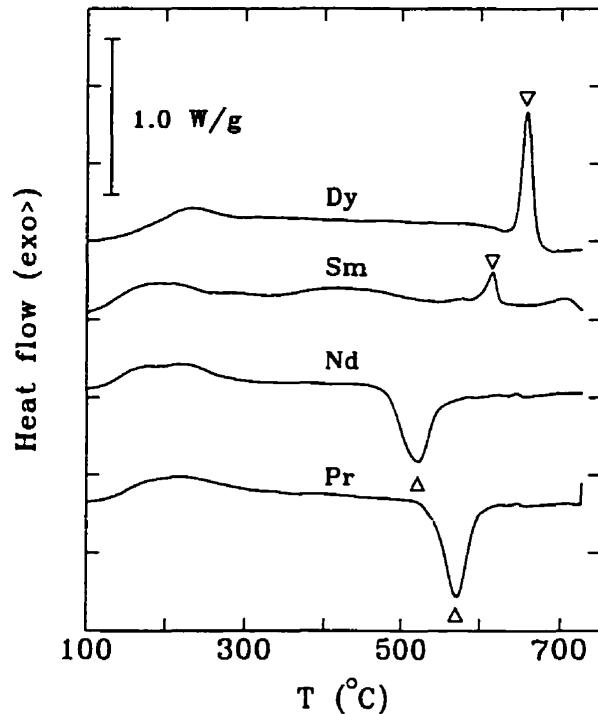


Figure 4.11: DSC scans at 40 C/min for R_2Fe_{17} ($R=Pr, Nd, Sm, Dy$) powders mechanically alloyed for 20 h. The results for the marked peaks are tabulated in Table 4.3

the formation of the 2-17 phase. It is noticed that all the 2-17 compounds formed by these annealings are *disordered* because the corresponding superlattice reflections are missing in the XRD patterns, as shown in Fig. 4.13.

The ordered structure is recognized by a distinct superlattice peak in the diffraction patterns of either the (204) reflection for the Th_2Zn_{17} -type structure (Nd_2Fe_{17} compound) or the (203) reflection for the Th_2Ni_{17} -type structure (Dy_2Fe_{17} compound). It is formed by high temperature (~ 1000 C) annealing the mechanically alloyed powders or of the cast alloys.

The disordered 2-17 phase, on the other hand, is distinguished by the disappearance of the superlattice reflection (see Fig. 4.13). It is formed by annealing of the mechanically alloyed powders at temperatures around the DSC peaks marked in Fig. 4.11. Annealing at intermediate temperatures yields partially disordered 2-17 phase, indicated by a relatively weak superlattice reflection (See Fig. 4.8 for the Sm_2Fe_{17} powder as an example).

Table 4.3: List of DSC results for R_2Fe_{17} ($R=Pr, Nd, Sm, Dy$ and Er) powders mechanically alloyed for 20 h corresponding to the high-temperature peak marked in Fig. 4.11. The definition of the onset temperature T_n and peak temperature T_p are illustrated Fig. 4.12. The enthalpy release ΔH_{MA} is in kJ/g-atom.

scanning rate	R =	Pr	Nd	Sm	Dy	Er	Y
40 C/min scans	T_n (C)	543	479	601	646	-	663
	T_p (C)	571	521	616	659	-	675
	ΔH_{MA}	+1.9	+1.6	$\sim -0.4^a$	-1.3	-	-0.6^b
20 C/min scans	T_n (C)	537	-	-	631	647	-
	T_p (C)	568	-	603^a	643	660	-
	ΔH_{MA}	+1.9	-	$\sim -0.7^a$	-1.3	-0.7	-

^a There are two exothermic peak close together. Particularly, for the 20 C/min scan, as shown in Fig. 4.12, the two peaks overlap and resulting $\Delta H_{MA} \sim -0.7$ kJ/g-atom is considerably larger than that from the 40 C/min scan.

^b This value has a lower accuracy than others because the exothermic peak is close to the maximum operating temperature, 727 C, of the DSC equipment.

4.4 Analysis and Discussion

4.4.1 High pressure phases of rare earth metals

Rare earth metals are well known to exhibit polymorphic behavior at high hydrostatic pressure[113, 114]. However, there is a common difficulty in the identification of the *fcc* high-pressure phase because the NaCl-type rare earth oxide or nitride, $R(O,N)$, has almost the exact same XRD pattern as the *fcc* structure. The structure of the NaCl-type $R(O,N)$ is a derivative of the high-pressure *fcc* rare earth simply obtained by inserting the small atoms, O or N, into the octahedral interstitial sites of the *fcc* structure. Full occupation of the octahedral interstitial sites yields the stoichiometric $R(O,N)$ phase. Nevertheless the concentration of the interstitial atoms may vary, leading to non-stoichiometric NaCl-type $R(O,N)_y$ ($y \leq 1$)[105, 106]. In other words, the *fcc* phase of rare earth metal forms a solid solution with O and N over a wide range, and it may be called an *fcc*-like structure. (In the subsequent Chapter 5 we will also

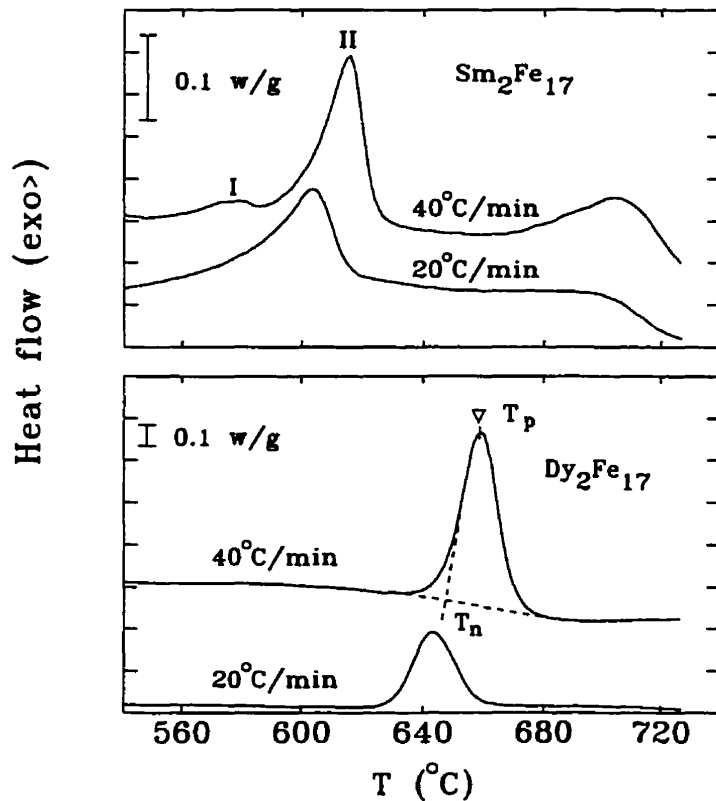


Figure 4.12: DSC scans at 20 C/min and 40 C/min for mechanically alloyed Sm_2Fe_{17} and Dy_2Fe_{17} respectively. The top figure illustrates that, for Sm_2Fe_{17} , peak I and II are merged together at 20 C/min. The bottom figure illustrates how to determine the onset temperature T_n and peak temperature T_p .

see that a metastable NaCl-type SmC_y carbide is formed during the crystallization of amorphous Sm-Fe-C). The octahedral interstitial sites are large (with a radius of about 1.1\AA for *fcc* Nd) enough to accommodate the interstitial C, N and O. In addition, the rare earths have high affinities for C, N and O[115]. As a consequence, the *fcc* rare earth metal can accommodate a large amount of interstitial C, N and O¹. Forming a solid solution over a wide concentration range with interstitial atoms is thus a characteristic of the *fcc* rare earth metals. We therefore propose a schematic Gibbs free energy diagram for the R-(O, N) system as shown in Fig. 4.14. Although the NaCl-type $R(O,N)_y$ of intermediate O and N concentrations may be metastable with respect to the phase separation into the R metal and the oxy-nitride of richer O and

¹In fact, the *fcc* structure also accommodates a large amount of interstitial hydrogen although hydrogen atoms mainly occupy the tetrahedral interstitial sites, different from C, N and O atoms.

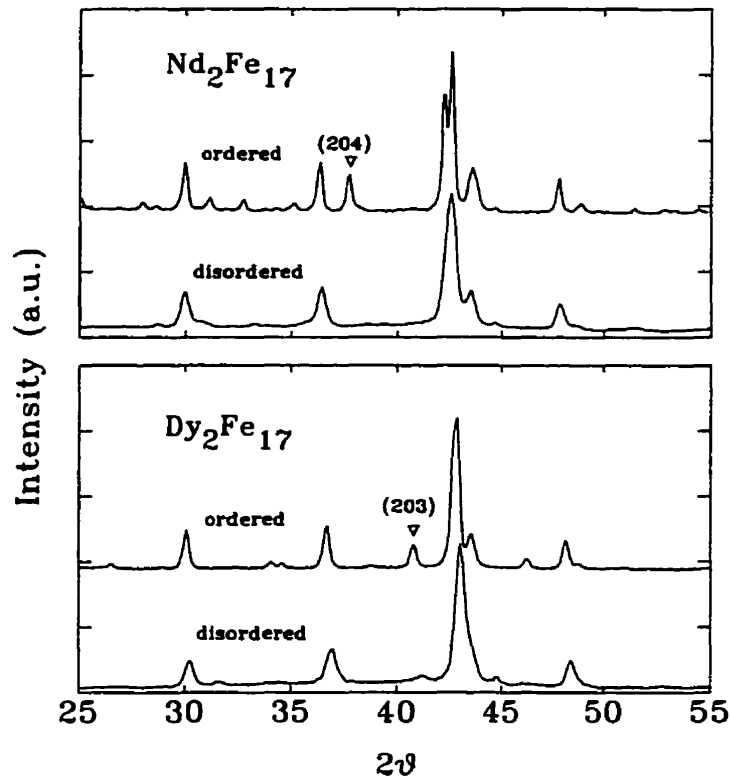


Figure 4.13: XRD scans for the ordered- and disordered- R_2Fe_{17} phases.

N (point “a” and “d”)¹, it may be kinetically stable because the separation requires long-distance atomic diffusion. Further absorption of O and N leads to the formation of the equilibrium NaCl-type $R(O,N)$ phase (O and N richer than point “d”), which may occur during annealing. The study in Chapter 5 will show that NaCl-type SmC_y may be stable up to 1100 C, caused by the absorption of O and N during annealing. The O- and N-stabilized *fcc*-like structure is also frequently found in the manufacture of Nd-Fe-B based permanent magnets[116].

The close relation between the *fcc* and NaCl-type phases may lead to misinterpretation of structures due to the unsuspected presence of impurities[117, 118, 119]. Alonso *et al.*[120] reported the formation of the high pressure *fcc* rare earth metals of Nd, Sm, Gd or Dy by mechanical alloying of elemental powders. The author later

¹The rare earth oxide has two stable phase, RO and R_2O_3 , as illustrated in Fig. 4.14. Although R_2O_3 is stabler than RO (the enthalpy of formation for SmO and Sm_2O_3 is -65 Sm₂O₃ -360 kJ/g-atom, respectively), RO appears much more frequently in our samples. It is possibly due to the presence of N.

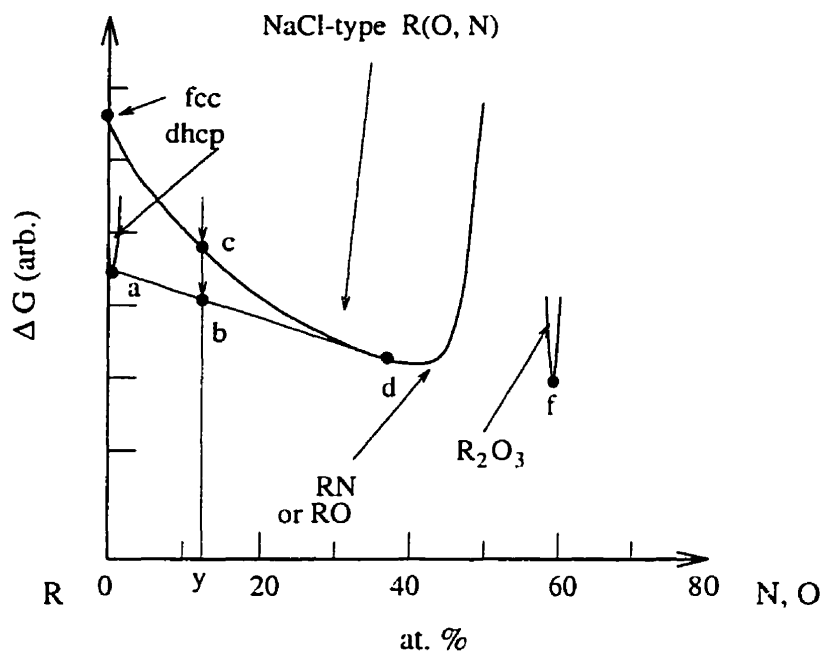


Figure 4.14: Schematic free energy diagram for the R-interstitial system.

announced that the *fcc* phases were, in fact, NaCl-type phases formed by reaction with oxygen and nitrogen during milling in a poorly sealed vial[119]. In the present study the contamination from oxygen and nitrogen has been reduced to a negligible level, as measured by the O/N analyzer, and annealing of the Pr_2Fe_{17} and the Nd_2Fe_{17} powder above 600 C led to the disappearance of the *fcc* phase and the formation of single phase 2-17 powder. We believe that the *fcc* phase observed in our study is the true high pressure phase and not an oxynitride and that this is the first conclusive work on the existent of the formation of the high pressure phase Pr and Nd by ball milling. The high pressure metastable phase does not decompose at room temperature because the transformation rate to the standard phase is slow. However, when the Sm_2Fe_{17} powder is ball milled for long times (≥ 50 h) (see Fig. 4.1), the prolonged milling causes sufficient absorption of O and N to produce the *fcc*-like phase, probably the NaCl-type $Sm(O,N)$. This is confirmed by the fact that the phase persist as a minor phase during annealing up to 1000 C.

The appearance of a high pressure phase in ball milling suggests the occurrences of high pressure conditions during the process. The standard structure (at atmospheric pressure and room temperature) for both Pr and Nd is *dhcp*. High pressure induces

the phase transformation from *dhcp* (double-*c hcp*) to *fcc*. The transition pressure is temperature dependent. It has been estimated that [89, 74, 121] ball-powder collisions during ball milling may cause local temperature increases up to ~ 300 – 400 C. During our ball milling process the ambient temperature was about 50 C. The processing temperature is then perhaps around 400 C. At that temperature, the transition pressure for the *dhcp* \rightarrow *fcc* transformation is 4.5 GPa for Pr and 4.0 GPa for Nd. The formation of the *fcc* Pr and Nd therefore suggests that the effective pressure in ball milling is above 4.5 GPa, consistent with the pressure estimated by other studies [72, 122] from the limit to the grain sizes reduction achieved by ball milling.

For Sm and heavier elements no sign of elemental rare earth metals was detected by the XRD; they form an amorphous phase with Fe. The difference in the phase formation in the mechanically alloyed R_2Fe_{17} is discussed in the following section.

4.4.2 Schematic free energy diagrams for R-Fe

Gibbs free energy diagrams are very useful for the understanding of mechanical alloying process. Phase formation in the mechanically alloyed R_2Fe_{17} compounds suggests schematic Gibbs free energy diagrams for the R-Fe systems as depicted in Fig. 4.15, 4.16 and 4.17. They represent the situation around the processing temperature of ball milling. At this relatively low temperature the Gibbs free energy is mainly determined by the enthalpy term ΔH in Eq. 4.10. In the following discussion, $\Delta H \approx \Delta G$ is sometimes implicit when the mechanical alloying process is addressed. Fig. 4.15, 4.16 and 4.17 are essentially for metastable phase; the intermetallic phases, that is, R_2Fe_{17} , R_6Fe_{23} , RFe_3 and RFe_2 , are not stable under ball milling and do not exist in the mechanically alloyed powders. The free energy curves for those intermetallic phases in the diagrams are drawn to illustrate the situation during annealing of the mechanically alloyed powders or to give a guideline in drawing the free energy curve for the amorphous phase.

Fig. 4.15 is for the rare earth heavier than Sm. The relative free energies for the intermetallic compounds, *ie.* R_2Fe_{17} , R_6Fe_{23} , RFe_3 and RFe_2 , are drawn based on the Y-Fe system, which has been well studied and has known thermodynamic functions for all the equilibrium intermetallic phases (Y is usually classified as a heavy rare earth element). To first order, the free energies for the Y-Fe compounds represent

those for the R-Fe compounds with R heavier than Sm. From Ref. [123], the Gibbs free energies of the four Y-Fe compounds are:

$$\Delta G (\text{general}) = \Delta H - T\Delta S, \quad (4.10)$$

$$\Delta G (Y_2Fe_{17}) = -6.38 \pm 0.31 + (1.9 \pm 0.28) \times 10^{-3}T \text{ kJ/g-atom},$$

$$\Delta G (Y_6Fe_{23}) = -8.09 \pm 0.49 + (2.24 \pm 0.44) \times 10^{-3}T \text{ kJ/g-atom},$$

$$\Delta G (YFe_3) = -8.97 \pm 0.54 + (3.03 \pm 0.48) \times 10^{-3}T \text{ kJ/g-atom},$$

$$\Delta G (YFe_2) = -7.09 \pm 0.61 + (0.96 \pm 0.55) \times 10^{-3}T \text{ kJ/g-atom}, \quad (4.11)$$

where ΔH and ΔS are the enthalpy and the entropy of the system, temperature T is in Kelvin.

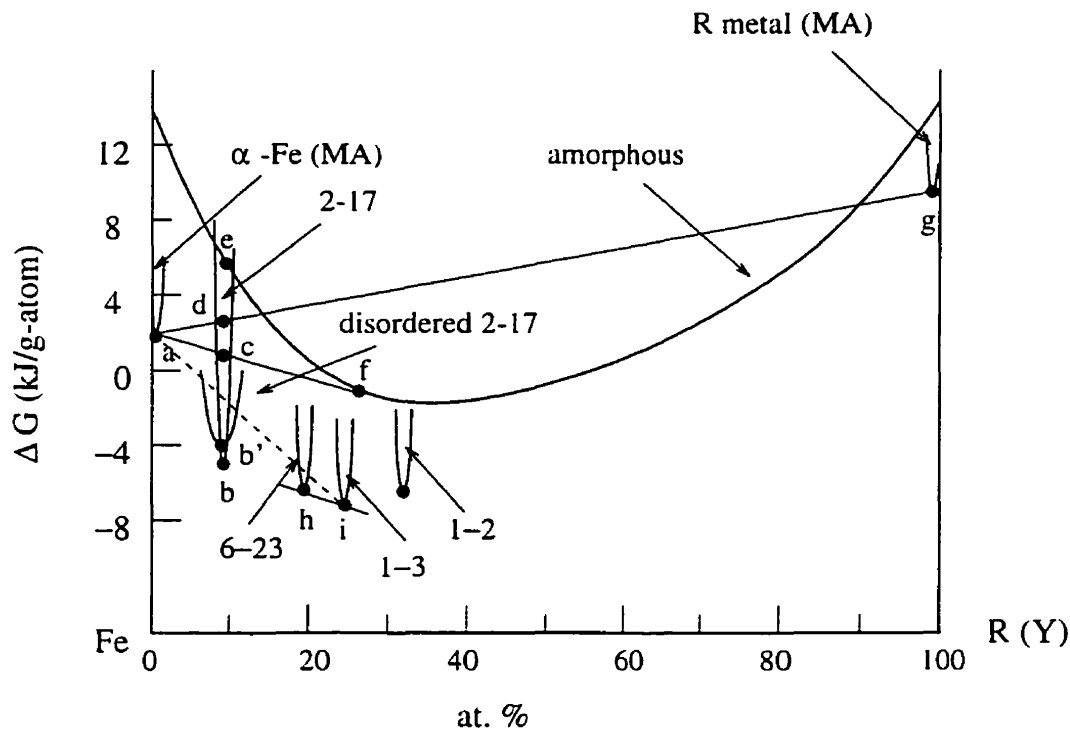


Figure 4.15: Schematic free energy diagram of the R-Fe system for R heavier than Sm. The energy of α -Fe under mechanical alloying, as denoted by " α -Fe (MA)", is about 2 kJ/g-atom higher than well-crystallized α -Fe[110] mainly due to high strains ($\sim 1\%$) in the lattice and large amount of grain boundaries for the ~ 10 nm grains.

At 400 C (estimated processing temperature), the corresponding free energies of the four compounds are $\Delta G = -5.1$ kJ/g-atom, -6.6 kJ/g-atom, -7.8 kJ/g-atom

and -6.7 kJ/g-atom, respectively. The common tangent between the α -Fe and the amorphous curves in the free energy diagram determines the compositions of the amorphous R-Fe (point “f”). To first order, the slope of the line “af” is close to that of line “hi” (the line connecting the 6-23 and 1-3 compounds) in Fig. 4.15. This gives a guideline in drawing the free energy diagram. The low-end limit of the amorphous ΔG is the intermetallic phases — the free energy of an amorphous phase must be higher than its crystalline counterpart below the melting point. This gives the estimation of the free energy difference between the 2-17 intermetallic phase and the α -Fe/amorphous mixture, $\Delta G_{bc} < -4$ kJ/g-atom (refer to line “ai” in Fig. 4.15). The enthalpy diagram for the heavy earth-iron can be constructed similarly to the free energy diagram based on the known Y-Fe system. The enthalpy of formation is also estimated to be $\Delta H_{bc} < -4$ kJ/g-atom, or $|\Delta H_{bc}| > 4$ kJ/g-atom. As studied above, the 2-17 initially crystallizes in the disordered form up to the maximum temperature of the DSC equipment. However the enthalpy associated with the ordering process could not be measured in our study, as explained in Section 4.2. The ordering enthalpy for several ordered compounds, such as AlNi_3 and CuTi , is about 30% of the enthalpy of formation [124, 125, 126]. In the case of R_2Fe_{17} structure the order-disorder only involves 6 atoms in one formula unit, *ie.* 2 R atoms and 2 pairs of Fe dumb-bells, which comprises 30% of the total atoms (19 atoms per formula). The ordering enthalpy for the R_2Fe_{17} is thus estimated to be 0.6 kJ/g-atom. In addition, as can be seen in Table 4.2 and Fig. 4.9, the disordering stretches the lattice along the c -axis, resulting in an increase in c/a ratio by 0.7%. Assuming the conservation of the total volume of the 2-17 phase, this increase corresponds to an increase of 0.5% in c . For the estimate of the elastic energy stored in this elastic deformation we assume the Young’s modulus of the 2-17 compound (along the c -axis) to be about 200 GPa, a value typical for steels. The elastic energy is estimated to be 50 J/g-atom, negligible comparing to other forms of energies, such as the ordering enthalpy and strains in the lattice induced by ball milling. The enthalpy of formation for the disordered 2-17, ΔH_{bc} , is therefore approximated as was ΔH_{bc} . However from the DSC scans (Fig. 4.11) and listed value in Table 4.3, the enthalpy release corresponding to the exotherm is about 1 kJ/g-atom, considerably smaller than $|\Delta H_{bc}|$, suggesting that the exothermic

enthalpy is not a result of the reaction between α -Fe and the amorphous R-Fe. In fact, for the mechanically alloyed Sm_2Fe_{17} powder, relaxation and crystallization of amorphous R-Fe occurs below the exothermic peak. However no prominent exothermic enthalpy associated relaxation and crystallization were observed, except the first exothermic peak at low temperature (see the scan for Dy in Fig. 4.11), ~ 200 C, which, according to the study on the Sm_2Fe_{17} powder, is attributed to the strain release in α -Fe and oxidation of the rare earth. The study on the Sm-Fe powder reveals that the structural change in the amorphous Sm-Fe proceeds very slow, as can be seen from the corresponding XRD pattern shown in Fig. 4.6. A slow thermal event yields broad and weak exothermic peak so that in the case of R-Fe (R heavier than Sm) it is not detectable by the DSC measurements.

Fig. 4.16 illustrates the Sm-Fe system, which has a richer rare earth content in the amorphous phase compared to the heavier rare earths (see Table 4.1). In this case, a broad exothermic peak between 350 C and 550 C, which corresponds to the structural change in amorphous Sm-Fe, is noticeable (see Fig. 4.11 and 4.6). The total integrated enthalpy for the temperature range between 300°C and 727°C is estimated to be -1.5 kJ/g-atom, which is approximately the value of $\Delta H_{\mu c}$. From the present study, the composition of amorphous Sm-Fe is close to be equiatomic, suggesting that the enthalpy of formation for the amorphous Sm-Fe is positive with respect to the elemental components over most of the composition range except for the region around $Sm_{50}Fe_{50}$, as illustrated in Fig. 4.16 (point "f"). A study[127] showed that mechanical alloying of $Sm_{20}Zr_7Fe_{73}$ led to the formation of a single amorphous phase; the addition of small amounts of Zr considerably enhances the ability of amorphous phase formation. Fe-Zr has a large negative enthalpy of formation for amorphous Fe-Zr ($\Delta H = -10$ kJ/g-atom at the equiatomic composition[127]). As a result, amorphous Fe-Zr is formed over a wide composition range by mechanically alloying. Iron-rich amorphous Sm-Fe can therefore be formed by the addition of a small amount of Zr.

Regarding the crystallization of the amorphous Sm-Fe, it is interesting to note that the crystallization product $SmFe_3$ phase of the mechanically alloyed amorphous Sm-Fe (composition $\sim Sm_{50}Fe_{50}$ as estimated by this study; (see Table 4.1)) is different from that of melt-spun amorphous Sm-Fe[128]. Crystallization of amorphous

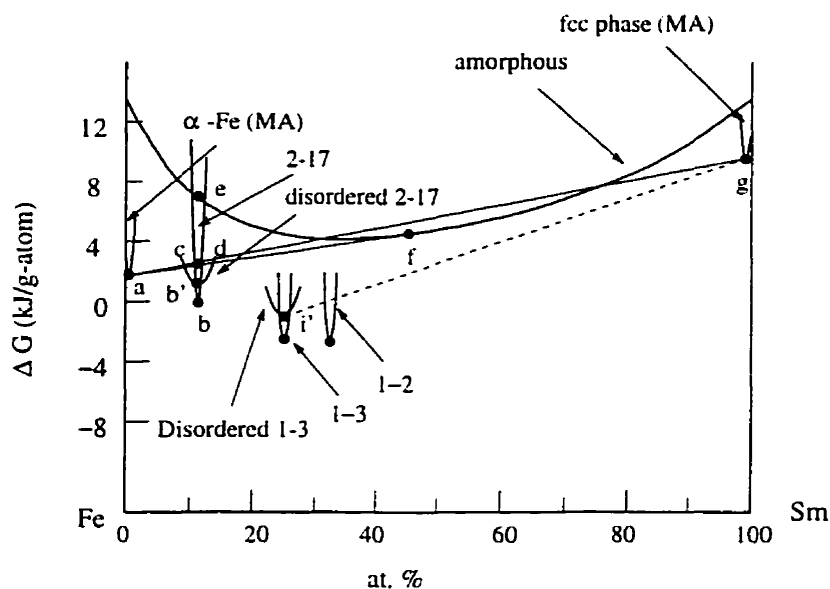


Figure 4.16: Schematic free energy diagram for Sm-Fe system.

Sm-Fe in over-quenched $\text{Sm}_{2.7}\text{Fe}_{17}$ alloys led to the formation of SmFe_2 (MgCu₂-type structure)[129] instead of SmFe_3 . Study by Miyazaki *et al*[128] showed that in amorphous $\text{Sm}_x\text{Fe}_{1-x}$ for $x=17 - 72.5$ prepared by melt spinning crystallization leads to SmFe_2 without a trace of SmFe_3 . The difference in the crystallization behavior between the amorphous specimens prepared by the two methods does not therefore result from the difference in the compositions. In the case of Sm-Fe we have observed, by the XRD measurements, traces of SmFe_2 phase exist in over-quenched $\text{Sm}_2\text{Fe}_{17}$ ribbons prepared by melt spinning with a Cu-wheel surface-speed of 62 m/s and the orifice of $\phi 0.3$ mm. (The corresponding XRD pattern is shown in Fig. 5.2 in the following chapter.) The existence of SmFe_2 phase implies that in the melt-spun ribbons short range order close to SmFe_2 may exist, whereas in the mechanically alloyed Sm-Fe powders the tendency to form any intermetallic phase is inhibited by nucleation difficulties. The difference in the crystallization behaviors in the two types of specimens is, therefore, probably due to the difference in short range order. Significant difference in crystallization behavior and kinetics of amorphous specimens prepared by the two methods (with the same composition) were also observed with Ni-Zr alloys[130, 131, 132, 133]. The major difference was the different degree of thermal relaxation; the low temperatures at which mechanical alloying took place allows

one to obtain samples in very unrelaxed state. Further work is therefore needed for understanding of the difference of the amorphous Sm-Fe phases prepared by both mechanical alloying and melt spinning methods.

Fig. 4.17 illustrates the schematic free energy diagram for the light rare earths, Nd and Pr. The curve is very similar to that suggested in Ref. [127]. Thermodynamic calculations based on the Miedema model[134] show that for Nd-Fe the enthalpy of formation for the amorphous Nd-Fe is positive with respect to the elemental components over the whole composition range[135]. A mixture of elemental components is thus thermodynamically favored. It has been reported that for Nd-Fe the steady-state in the mechanically alloyed Nd-Fe (starting with elemental powders) is the unmixed elements[136].

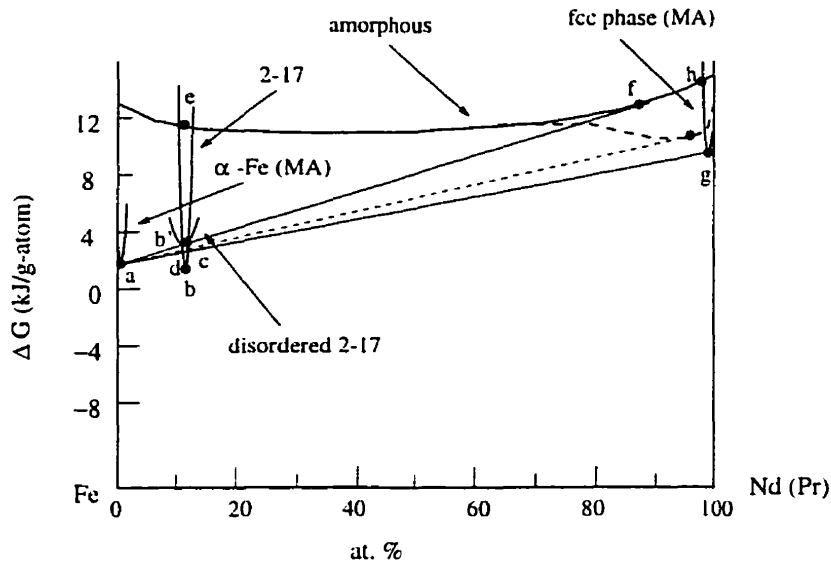


Figure 4.17: Schematic free energy diagram of the R-Fe system for R=Pr or Nd. The dashed curve illustrates that for Pr there may be an inclination in the amorphous Pr-Fe free energy curve around the Pr-rich end.

Due to the positive enthalpy of mixing for Pr-Fe, demixing of Pr and Fe by ball milling of Pr_2Fe_{17} compound is observed in this study (see Fig. 4.3). Whereas in the Nd_2Fe_{17} powder only a small amount of high pressure phase is formed after the 20 h mechanical alloying process. The demixing requires kinetically long-range atomic diffusions, which is a slow process. Fig. 4.4 shows the overall fitting of the XRD pattern for the Pr_2Fe_{17} powder: two broad peaks are present besides the α -Fe and

the *fcc* phase. The broad peak centered at $2\theta \sim 30.5^\circ$ is possibly correspondent to a Pr-rich amorphous phase, implying that an inclination in the amorphous Pr-Fe free energy curve around the Pr-rich end may exist. The existence of the inclination is perhaps the reason that the demixing proceeds faster in the $\text{Pr}_2\text{Fe}_{17}$ powder than that in the $\text{Nd}_2\text{Fe}_{17}$ powder. Without the inclination as postulated for the $\text{Nd}_2\text{Fe}_{17}$ powder the demixing of the elements requires an extra energy to overcome the energy rising along curve “fh” in Fig. 4.17. The XRD pattern for the $\text{Nd}_2\text{Fe}_{17}$ powder (see Fig. 4.3) shows very diffuse background between 30° and 40° in addition to the α -Fe and the high pressure phase, implying that the amorphous Nd-Fe may have a range of compositions falling in between “f” and “h” as illustrated in Fig. 4.17. In Fig. 4.17 it is illustrated that the 2-17 phase (at least the disordered one) has a high free energy than that for the mixture of elemental Pr and Fe. It is so illustrated because our study has shown that the formation of 2-17 phase is associated with an endothermic transformation with $\Delta H = +1.9$. A similar endothermic phase transformation in the mechanically alloyed $\text{Nd}_2\text{Fe}_{17}$ occurs as seen from DSC scans in Fig. 4.11. Few alloy systems demonstrate endothermic phase transformation in forming an intermetallic phase. It was reported that in melt-spun MnBi ribbons the intermetallic MnBi is formed through endothermic transformation, where the endothermic process is the melting of the Bi-rich eutectic. The eutectic points for the rare earth-rich Pr-Fe and Nd-Fe eutectic are 620 C and 640 C [137], which are much higher than the endothermic points 570 C and 520 C (see Table 4.3) for $\text{Pr}_2\text{Fe}_{17}$ and $\text{Nd}_2\text{Fe}_{17}$, respectively. This endothermic enthalpy is therefore not related to the melting of Pr-Fe or Nd-Fe eutectic. Further study is needed to understand this endothermic transformation.

4.5 Summary

In the present study, phase formation in mechanically alloyed R_2Fe_{17} and the phase transformation reaction in the subsequently annealed samples is quantified by x-ray diffraction and thermomagneto-metric measurements. With the help of complementary DSC measurements and the available thermodynamic data, we are able to propose plausible free energy diagrams for the series of R-Fe. The free energy diagrams are consistent with the quantitative phase analysis and the enthalpy measurements.

Through the present study it is established that Sm behaves as a heavy rare earth element in the R-Fe system although it belongs to the first half of the rare earth series. This is a useful understanding for the development of the R-Fe based compounds for the new permanent magnet materials.

In our studies, a variety of metastable phases have been characterized by x-ray, TMA and DSC measurements. These include amorphous R-Fe, nanocrystalline and highly strained α -Fe, high-pressure *fcc* rare earths and its derivatives with interstitial atoms, disordered R_2Fe_{17} and RFe_3 . The phase transformation reactions associated with those phases are studied. Particularly, the ordering transformation in the 2-17 structure is systematically characterized, for the first time, by the order parameter, lattice constant and the Curie temperature, and the relationships among them are established.

The knowledge acquired through the present study (that is, in the free energy diagrams, phase formation and transformation and the structural properties of the 2-17 phase) is essential for the study of the more complicated ternary Sm-Fe-C system. Phase formation and transformation in iron-rich Sm-Fe-C and the stability of 2-17 carbides form the central subject of the present thesis and will be presented in the following chapter.

Furthermore the present study also reveals that the R-Fe alloys for the light rare earths (Pr and Nd) is an interesting system. The high pressure phase is formed by the high energy ball milling and an endothermic process occurs in the crystallization of the R_2Fe_{17} phase.

PHASE FORMATION IN IRON-RICH SM-Fe-C

In this chapter phase formation and transformation in the mechanically alloyed iron-rich Sm-Fe-C is investigated. First, phases in the powders as-prepared by ball milling are analyzed. Then the result of annealing to successively higher temperatures is examined. We will learn how the $\text{Sm}_2\text{Fe}_{17}$ carbide is formed by mechanical alloying, what is the critical content of carbon in $\text{Sm}_2\text{Fe}_{17}$ and what phases are produced when the carbon content in $\text{Sm}_2\text{Fe}_{17}$ exceeds this limit. We focus on the compositions of $\text{Sm}_2\text{Fe}_{17}\text{C}_x$ ($x=0-1.0$). $x=1.0$ is chosen as the highest carbon content for the present study because this is maximum carbon content for a stable $\text{Sm}_2\text{Fe}_{17}$ carbide that has been reported[5, 21, 138, 139]¹.

5.1 Mechanical Alloying

Mechanically alloyed powders were prepared by ball milling single phase compounds at high energy for 15 h. These compounds are $\text{Sm}_2\text{Fe}_{17}\text{C}_x$ ($x=0, 0.3, 0.45, 0.85$ and 1.0) and $\text{Sm}_2\text{Fe}_{14}\text{C}$. The ball diameter was 12.7 mm and the ball-to-material ratio was 8:1. The ball milling time was chosen in accordance with the studies in the previous chapter (refer to Fig. 4.3). 15 h is the minimum time required for these compounds to reach steady-state under mechanical alloying. Longer milling-times were not used because oxygen and nitrogen then become absorbed by the powders. Nitrogen and oxygen content have to be minimized for the present study because we are investigating samples with a small amount of carbon content, and the presence

¹As to the maximum carbon content, even though $\text{Sm}_2\text{Fe}_{17}\text{C}_x$ with $x > 1.0$ can be prepared through low temperature reaction between $\text{Sm}_2\text{Fe}_{17}$ and a carbon-containing substance, it is metastable through the whole temperature range up to 1150 C; the maximum carbon content for a stable $\text{Sm}_2\text{Fe}_{17}$ carbide is $x=1.0$ which occurs at high temperatures at around 1150 C.

of even very small amounts of nitrogen and oxygen may alter the phase formation of carbon with Sm and Fe.

Mechanical alloying of $\text{Sm}_2\text{Fe}_{17}\text{C}_x$ and $\text{Sm}_2\text{Fe}_{14}\text{C}$ compounds lead to a mixture of an amorphous phase and nanocrystalline $\alpha\text{-Fe}$, as shown in Fig. 5.1. A small amount of residual 2-17 phase (<5 vol.% estimated from its integrated intensities in XRD scans) is present as well, as indicated in Fig. 5.1.

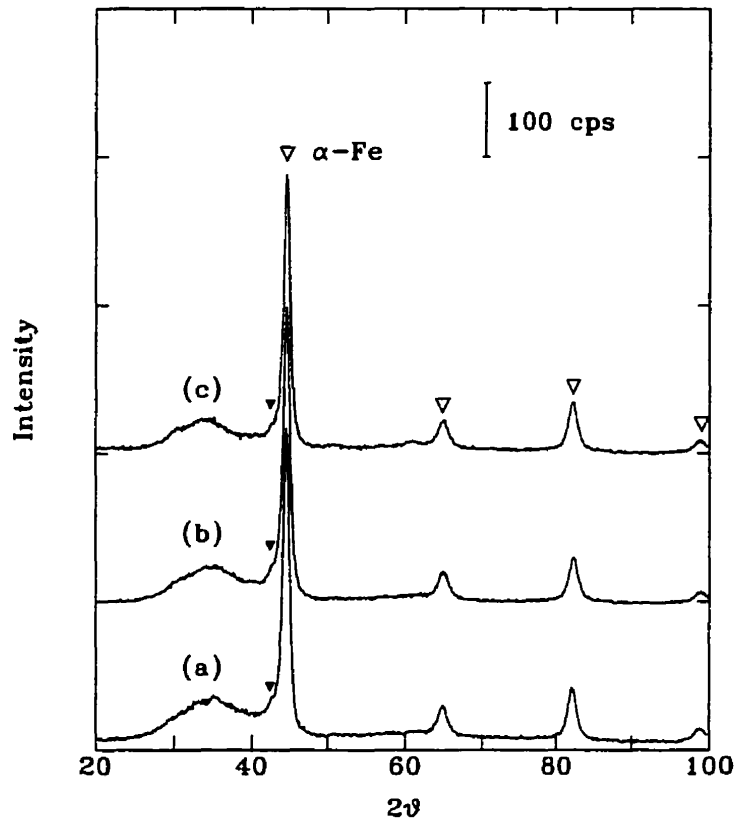
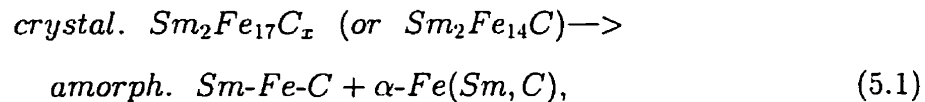


Figure 5.1: XRD scans of mechanically alloyed (15 h) $\text{Sm}_2\text{Fe}_{17}\text{C}_x$ for (a) $x=0$, (b) $x=0.45$ and (c) $x=1.0$. The filled triangles mark the position of the principal reflection of the 2-17 structure. The amount of 2-17 phase is negligible.

The decomposition scheme during the ball milling can be summarized as



neglecting any residual amount of the 2-17 phase. The results of quantitative XRD analysis are listed in Table 5.1 and are used to estimate the composition of $\alpha\text{-Fe}$ and the amorphous phase.

Table 5.1: Quantitative analysis of x-ray measurements on mechanically alloyed Sm-Fe(-C) powders. d and e are the average grain size and overall lattice strains in α -Fe. $\Delta V/V$ is the lattice expansion and I/I_0 is the relative (integrated) intensity of α -Fe in the mechanically alloyed mixture with respect to the pure Fe powder; Z is the amorphous composition estimated by using Eq. 5.3.

	d (nm)	e	$\Delta V/V$	I/I_0	Z
$\text{Sm}_2\text{Fe}_{17}$	8.4	0.62%	0.35 %	57 %	$\text{Sm}_{43}\text{Fe}_{57}$
$\text{Sm}_2\text{Fe}_{17}\text{C}_{0.45}$	-	-	0.41%	55 %	$\text{Sm}_{37}\text{Fe}_{55}\text{C}_8$
$\text{Sm}_2\text{Fe}_{17}\text{C}_{1.0}$	7.7	0.66%	0.44 %	53 %	$\text{Sm}_{33}\text{Fe}_{51}\text{C}_{16}$
$\text{Sm}_2\text{Fe}_{14}\text{C}$	-	-	0.38 %	49 %	$\text{Sm}_{35}\text{Fe}_{48}\text{C}_{17}$

In the mechanically alloyed powders, the unit cell volume, V , of α -Fe is slightly larger for the carbon-containing powders than that for the binary $\text{Sm}_2\text{Fe}_{17}$ powder, as seen from Table 5.1. The difference is possibly due to carbon interstitials in the α -Fe lattice. The carbon content in α -Fe for carbon-containing powders is estimated from the difference in the lattice expansions to be ~ 1 at.%. (Carbon has a very small solubility in α -Fe; at equilibrium, the maximum solubility of carbon, 0.42 at.%, occurs at 1495 C in δ -Fe, which has the same *bcc* structure as α -Fe). Most of the C atoms should therefore be in an amorphous phase. The equation balancing composition for the decomposition of $\text{Sm}_2\text{Fe}_{17}\text{C}_x$ is therefore expressed as

$$0.5\text{Sm}_2\text{Fe}_{17}\text{C}_x = \text{SmFe}_z\text{C}_{0.5x} + (8.5 - z) \alpha\text{-Fe}, \quad (5.2)$$

neglecting any solution of Sm and C in α -Fe.

The composition of the amorphous phase can be estimated from the relative intensity of the α -Fe x-ray reflection using the following equation, derived by combining Eq. 5.2 with Eq. 4.1,

$$z = 8.5(1 - I/I_0) - I/I_0 \left(\frac{\mu_R^* m_R + 0.5x \mu_C^* m_C}{\mu_{Fe}^* m_{Fe}} \right), \quad (5.3)$$

where μ_C^* and m_C are the mass absorption coefficient of the Cu- K_α x-ray radiation and the atomic weight for carbon, the other notations are the same as defined in

Eq. 4.3. Using the above equation the Sm:Fe ratio in the amorphous phase, z , is calculated from the relative intensity of the α -Fe intensity, I/I_0 , as listed in Table 5.1. The carbon content listed in the table is calculated by assuming that all the carbon atoms are in the amorphous matrix as expressed in Eq. 4.3. From Table 5.1 it can be seen that the relative concentrations of Sm and Fe (or the ratio of the two concentration) in the amorphous phase are the same within experimental error ($\pm 10\%$ in composition estimation) after the addition of carbon atoms. In fact this is obvious from the XRD patterns in Fig. 5.1, which show that the α -Fe intensity in all the different powder samples is almost constant. Further evidence that the amorphous phase accommodates most of the carbon atoms can be seen from the significantly different crystallization behavior of amorphous phases in the $\text{Sm}_2\text{Fe}_{17}$ and the $\text{Sm}_2\text{Fe}_{17}\text{C}$ powders, as we examine in the following section.

In spite of the presence of up to 16 at.% of carbon atoms in the amorphous phase (corresponding to the $\text{Sm}_2\text{Fe}_{17}\text{C}_{1.0}$ and $\text{Sm}_2\text{Fe}_{14}\text{C}$ milled-powders), the Fe content remains almost constant. As discussed in the previous chapter the allowed composition range in mechanical alloying is determined by the free energy diagram, essentially from the enthalpy of mixing. The fact that the Fe concentration is the same in all the series of carbon-containing amorphous phases is probably a result of a positive enthalpy of mixing between Fe and carbon (the formation enthalpy for Fe_3C is $\Delta H = +8$ kJ/g-atom at room temperature[16]).

The relative amount of the amorphous phase in the series of mechanically alloyed $\text{Sm}_2\text{Fe}_{17}\text{C}_x$ is therefore constant. In contrast to mechanical alloying, amorphization of $\text{Sm}_2\text{Fe}_{17}\text{C}_x$ with melt-spinning strongly depends on the carbon content, x . As shown in Fig. 5.2 the addition of carbon considerably increases the fraction of the amorphous phase. Quantitative x-ray analysis shows that the volume fraction of the amorphous phase is 20% and 75% for the melt-spun $\text{Sm}_2\text{Fe}_{17}$ and $\text{Sm}_2\text{Fe}_{17}\text{C}_{1.0}$, respectively. The process of formation of 2-17 phase in the melt-spun $\text{Sm}_2\text{Fe}_{17}\text{C}_{1.0}$ will be studied briefly in the next section as a comparison with the corresponding ball milled specimens.

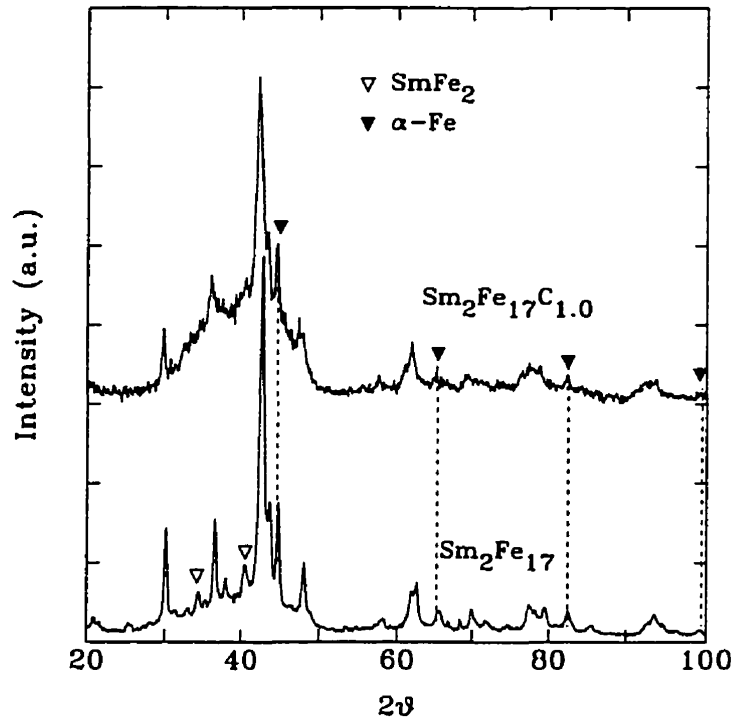


Figure 5.2: XRD scans for melt spun $\text{Sm}_2\text{Fe}_{17}$ and $\text{Sm}_2\text{Fe}_{17}\text{C}_{1.0}$ ribbons. Both types of ribbons were prepared at 62 m/s surface speed with $\phi 0.3$ quartz orifice.

5.2 Annealing of Mechanically Alloyed $\text{Sm}_2\text{Fe}_{17}\text{C}_{1.0}$

Phase formation in mechanically alloyed $\text{Sm}_2\text{Fe}_{17}\text{C}_{1.0}$ powders under various annealing conditions is studied in this section. Annealing was carried out in two different ways. In the first way, a sample was heated at a constant rate of 40 C/min to a predetermined temperature followed by fast cooling, while, in the second, the sample was held at the temperature for a certain period of time (isothermal annealing). The structural change and phase formation at various annealing stages were monitored by XRD and TMA measurements performed on samples cooled to room temperature.

5.2.1 Phase formation during heating at 40 C/min

Low temperature annealing:

The differential scanning calorimeter was used to carry out the annealing and the maximum operating temperature is 727 C for the calorimeter.

The release of enthalpy and the change in magnetization during heating of the mechanically alloyed $\text{Sm}_2\text{Fe}_{17}\text{C}_{1.0}$ were measured by DSC and TMA as shown in

Fig. 5.3.

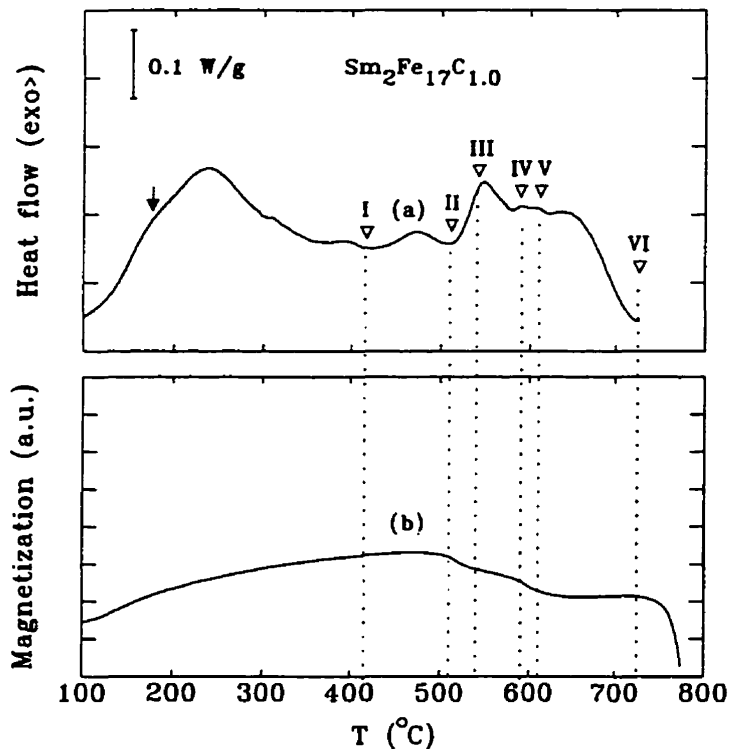


Figure 5.3: DSC and TMA scans at 40 C/min for the mechanically alloyed $\text{Sm}_2\text{Fe}_{17}\text{C}$ powder. TMA data is plotted in an arbitrary unit. The marked temperatures are: (I) 410 C, (II) 510 C, (III) 540 C, (IV) 590 C, (V) 610 C and (VI) 727 C. The corresponding XRD patterns are shown in Fig. 5.4. An arrow in the figure indicates the oxidation of Sm involved in the first exothermic peak.

Heating to 410 C leads to the release of strains in the α -Fe lattice, as determined from the peak widths of the corresponding x-ray reflections, the average grain size of α -Fe (8 nm) remaining the same as that for the as-milled powder. The enthalpy of the first exothermic peak (2.5 ± 0.5 kJ/g-atom) is however considerably larger than the reported enthalpy associated with the strains in the mechanically alloyed α -Fe[72]. As studied in Chapter 4, oxidation of Sm occurs around 200 C and a small amount of oxygen, less than 1 at.%, releases a large enthalpy. The first exothermic peak between 100 C and 400 C therefore involves two processes, namely, the oxidation of Sm and strain release in α -Fe. However the two processes overlap. The “shoulder” in the first exothermic peak around 200 C, as indicated in Fig. 5.3, is attributed to the oxidation of Sm. This is confirmed by the observation that the magnitude of the “shoulder” increased when a sample was deliberately exposed to air for a long time.

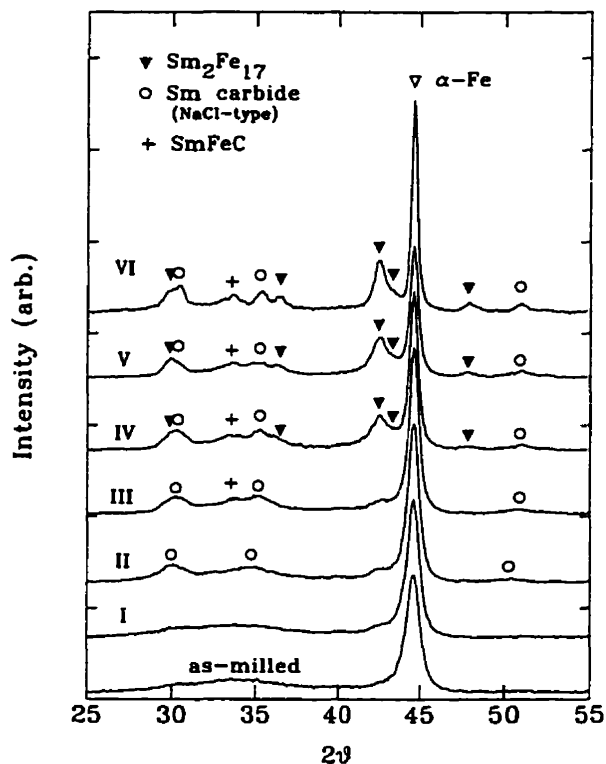


Figure 5.4: XRD scans for the as-milled and post-heated $\text{Sm}_2\text{Fe}_{17}\text{C}$ powder to various temperatures: (I) 410 C, (II) 510 C, (III) 540 C, (IV) 590 C, (V) 610 C and (VI) 727 C. Heating rate is 40 C/min.

Heating to 510 C yields the crystallization of a metastable NaCl-type SmC_y interstitial carbide (see scan II in Fig. 5.4). XRD analysis shows a lattice constant of $a=5.14\pm 0.01$ Å, a value smaller than previously reported[140]. (The reported NaCl-type SmC_y interstitial carbide is a high temperature phase, called tri-rare-earth carbide, Sm_3C [141, 140] and has a lattice constant of $a=5.17$ Å. The carbon content in the Sm_3C phase is reported to vary between 25 and 33 at.%) According to the study in the previous chapter, this NaCl-type rare earth interstitial compound does not dissolve Fe. The smaller lattice constant therefore suggests less carbon content in the structure. Linear extrapolation (assuming the lattice constant for zero carbon content is 5.04 Å, the value for the high pressure *fcc* Sm) gives $\text{SmC}_{0.21}$. The small exothermic peak between I and II in Fig. 5.3 corresponds to this transformation. The crystallization of the metastable NaCl-type SmC_y from the amorphous Sm-Fe-C must be accompanied by that of a Fe-rich phase because the composition of the amorphous phase is about $\text{Sm}_{33}\text{Fe}_{51}\text{C}_{16}$ (see Table 5.1). With the broad XRD peaks from the

nanocrystalline $\text{SmC}_{0.21}$ (average grain size ~ 5 nm, as determined from XRD analysis), this Fe-rich phase is difficult to resolve by XRD measurement; it is either an amorphous phase or a crystalline phase of very fine grains.

A phase transition occurs between 510 C and 590 C and a decrease in α -Fe was observed in this temperature range (see the DSC and TMA scans between II and IV in Fig. 5.3). XRD measurements (scans III and IV) show that a number of events occur in this temperature range: 1) SmC_y peaks are shifted to higher angles reflecting a decrease in the lattice constant ($a=5.07$ Å) to correspond to a carbon content of 6 at.% in the SmC_y ; 2) the amount of SmC_y is increased by 70%; 3) the α -Fe content is reduced by about 20%, a value consistent with the TMA measurement in Fig. 5.3; 4) a peak around $2\theta=33.8^\circ$ emerges, indicating the formation of a new phase, which we later identify as the SmFeC phase, isostructural with GdFeC [142].

Fig. 5.5 illustrates the presence of the SmFeC phase in the powder heated to 727 C, as is seen comparing the XRD pattern to an as-cast $\text{Sm}_2\text{Fe}_{17}\text{C}_{1.0}$. The presence of the SmFeC phase is clearer in the as-cast specimen because the corresponding XRD peaks are sharper. It can be seen that the SmFeC peaks overlap considerably with peaks that belong to other phases.

It is seen from Fig. 5.3 (between IV and V) that a further decrease in α -Fe (about 15%) occurs between 590 C and 610 C with a corresponding increase in the 2-17 phase (see scans IV and V in Fig. 5.4), reflecting the reaction between α -Fe and a Sm-rich phase to form the 2-17 structure. The 2-17 phase formed at this stage is disordered, as there is no superlattice reflection (204) around $2\theta=37.5^\circ$ (see page 66) The 2-17 phase evolved contains a negligible amount of interstitial carbon atoms, as determined from the lattice constants. The Curie temperature of the phase is $T_c=190$ C, suggesting a completely disordered 2-17 structure (see Fig. 4.10 and Eq. 4.7). The temperature range for the formation of the 2-17 phase coincides with that in the mechanically alloyed $\text{Sm}_2\text{Fe}_{17}$ powders, as studied in the previous chapter.

Further heating to 727 C does not induce noticeable reaction between the phases in the mixture. However the XRD peaks become narrower comparing to those in the powders annealed to 610 C, reflecting grain growth and strain release in each of the phases.

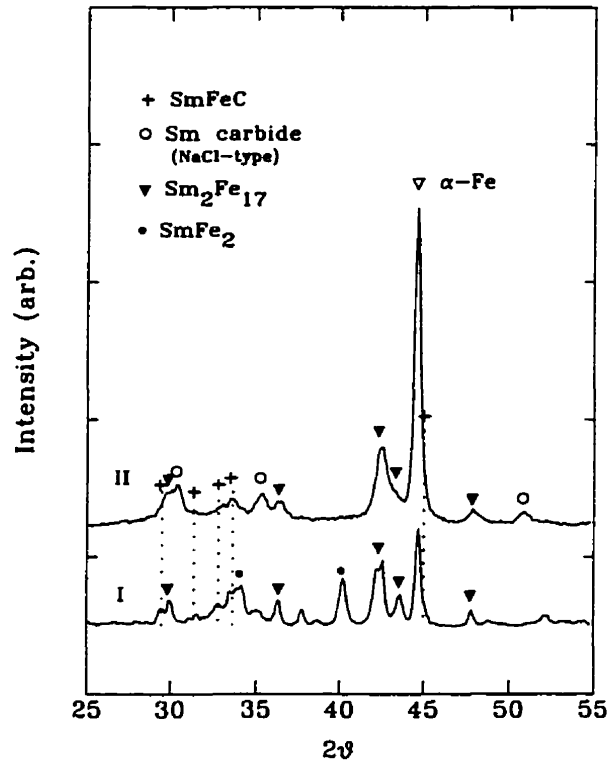
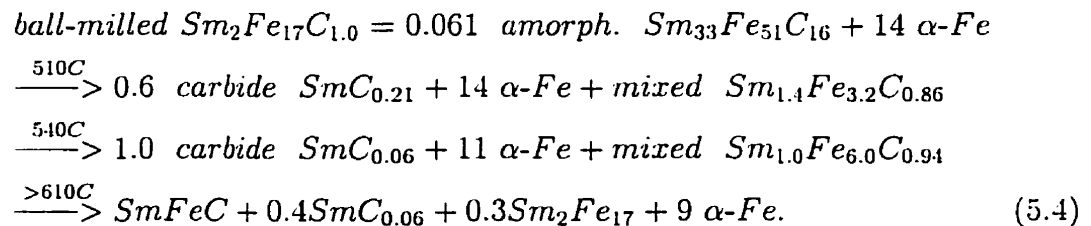


Figure 5.5: XRD scans for a mechanically alloyed powder heated to 727 C (pattern II) and an as-cast ingot of $\text{Sm}_2\text{Fe}_{17}\text{C}_{1.0}$ (pattern I).

Quantitative phase analysis has been conducted on the XRD scans shown in Fig. 5.4, and combined with the DSC and TMA measurements, allows us to describe the phase evolution of the mechanically alloyed $\text{Sm}_2\text{Fe}_{17}\text{C}_{1.0}$ powders upon annealing as follows:



It should be noted that quantitative phase analysis is available for the $\text{Sm}_2\text{Fe}_{17}$, $\alpha\text{-Fe}$ and SmC_y , but not for the SmFeC as its crystal structure is not well established¹. The above expressions are therefore balanced to have the overall composition

¹The primitive unit cell of the GdFeC -type structure is hexagonal. However, the space group and the atomic positions in the structure is unknown.

$\text{Sm}_2\text{Fe}_{17}\text{C}_{1.0}$. For example, in Eq. 5.4, the fractions of the $\text{Sm}_2\text{Fe}_{17}$, $\alpha\text{-Fe}$ and $\text{SmC}_{0.06}$ are obtained from the quantitative phase analysis, but that for SmFeC , it is calculated from the composition balance. In the above expressions, the mixed $\text{Sm}_{1.4}\text{Fe}_{3.2}\text{C}_{0.86}$ or $\text{Sm}_{1.0}\text{Fe}_{6.0}\text{C}_{0.94}$, which are determined from the requirement of the composition balance, contains SmFeC and another phase that cannot be resolved in this study.

XRD and TMA measurement on other compositions, $\text{Sm}_2\text{Fe}_{17}\text{C}_x$ for $x=0.3, 0.45, 0.85$ and $\text{Sm}_2\text{Fe}_{14}\text{C}$, were performed as well. Heating to 727 C, the maximum temperature of the DSC system, led to the phase mixture of $\text{Sm}_2\text{Fe}_{17}$ (disordered), SmFeC , $\text{SmC}_{0.06}$ and $\alpha\text{-Fe}$, similar to the case for the $\text{Sm}_2\text{Fe}_{17}\text{C}$ powders. However, the relative amount of each phase depends on the overall composition of the powder. In powders of lower carbon contents, heating to 727 C results in lower amount of SmFeC , $\text{SmC}_{0.06}$ and $\alpha\text{-Fe}$ but a higher amount of $\text{Sm}_2\text{Fe}_{17}$.

$\text{Sm}_2\text{Fe}_{17}$ carbides are not formed in any of the powders when heated up to 727 C.

High temperature annealing:

Further heating of $\text{Sm}_2\text{Fe}_{17}\text{C}_{1.0}$ powders to temperatures above 727 C, which is the maximum operating temperature of the differential scanning calorimeter, was carried out in a high temperature furnace. As shown in Fig. 5.6, heating to 750 C leads to the formation of almost single phase $\text{Sm}_2\text{Fe}_{17}\text{C}_{1.0}$, except for a small amount of $\text{SmC}_{0.06}$ and $\alpha\text{-Fe}$. The $\text{Sm}_2\text{Fe}_{17}\text{C}_{1.0}$ is formed by a reaction of $\text{Sm}_2\text{Fe}_{17}$, SmFeC , $\text{SmC}_{0.06}$ and $\alpha\text{-Fe}$. The crystal structure of the $\text{Sm}_2\text{Fe}_{17}\text{C}_{1.0}$ is similar to that of the $\text{Sm}_2\text{Fe}_{17}$ compound (the $\text{Th}_2\text{Zn}_{17}$ structure, space group $R\bar{3}m$) with carbon atoms in the interstitial 9e sites (see page 14 for the crystal structure). The introduction of the interstitial carbon atoms into $\text{Sm}_2\text{Fe}_{17}$ results in a lattice expansion as indicated by the shift of the corresponding XRD peaks towards lower angles (see Fig. 5.6). It is calculated from this shift of the XRD peaks that, for the $\text{Sm}_2\text{Fe}_{17}\text{C}_{1.0}$, the lattice expansion is 2.0% with respect to the $\text{Sm}_2\text{Fe}_{17}$. In addition to the lattice expansion, the presence of the interstitial carbon atoms also results in an increase in the Curie temperature by ~ 100 C as can be seen in Fig. 5.8.

However, $\text{Sm}_2\text{Fe}_{17}\text{C}_{1.0}$ is not stable at higher temperatures. As shown by the XRD patterns in Fig. 5.6, heating above 780 C leads to the transformation of the $\text{Sm}_2\text{Fe}_{17}\text{C}_{1.0}$ to another phase, which is identified as $\text{Sm}_2\text{Fe}_{14}\text{C}$, isostructural with

$\text{Nd}_2\text{Fe}_{14}\text{B}$. The Curie temperature of $\text{Sm}_2\text{Fe}_{14}\text{C}$ is 310 C[143], as illustrated in Fig. 5.8.

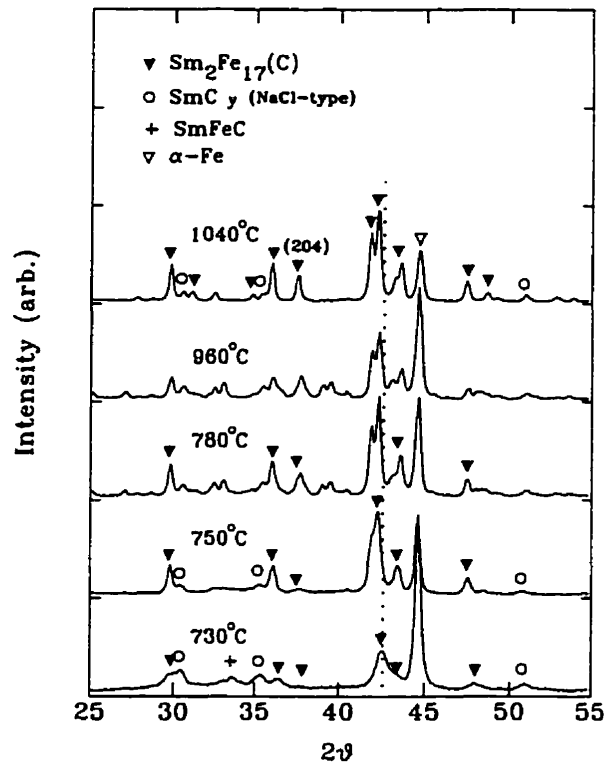


Figure 5.6: XRD scans of mechanically alloyed $\text{Sm}_2\text{Fe}_{17}\text{C}_{1.0}$ powder heated to temperatures higher than 727 C at ~ 40 C/min. Above $T \geq 750$ C the XRD peaks corresponding to the 2-17 structure shift to lower angles, reflecting the lattice expansion caused by the presence of the interstitial carbon atoms in 2-17 structure to form $\text{Sm}_2\text{Fe}_{17}\text{C}_{1.0}$. The unmarked peaks belong to the 2-14-1 structure.

The 2-14-1 and 2-17 phase have considerable similarity in their structures (see Section 2.1.5) and as a consequence their principal XRD reflections overlap. Fig.5.7 illustrates the XRD patterns of the single phase 2-17 and 2-14-1 compounds. Deconvolution of the two sets of XRD patterns is difficult.

Furthermore, as a result of its complicated structure, the 2-14-1 phase has a large number of XRD lines, leading to a low intensity of each line. Thus XRD is not a sensitive way to detect 2-14-1. The most effective way to distinguish it from 2-17 is through TMA. 2-14-1 has a Curie point at 310 C, easily be distinguishable from 2-17 and its carbides, although difficulty in distinguishing the $\text{Sm}_2\text{Fe}_{14}\text{C}$ and $\text{Sm}_2\text{Fe}_{17}\text{C}_x$ by TMA does arise when their Curie temperatures are close (as occurs when $x \sim 1.5$). Furthermore, TMA is very sensitive as illustrated in Fig. 5.8, where it shows clearly that heating to 780 C yields a considerable amount of the 2-14-1

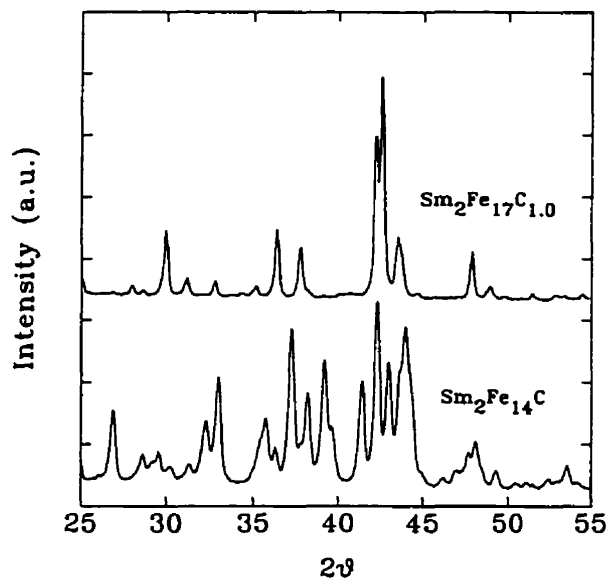
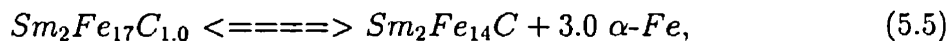


Figure 5.7: XRD patterns for single phase 2-17 and 2-14-1 compound.

phase. The corresponding XRD scan in Fig. 5.6 shows only a few lines corresponding to 2-14-1.

The amount of 2-14-1 increases with temperature up to 960 C and then transforms back to $\text{Sm}_2\text{Fe}_{17}\text{C}_{1.0}$ at 1040 C, leading to an almost single-phase $\text{Sm}_2\text{Fe}_{17}\text{C}_{1.0}$ powder (see Fig. 5.6 and Fig. 5.8). A small amount of the SmC_y carbide persists in the powder annealed to 1040 C ($y=0.06$ as calculated from its lattice constant $a=5.07$ Å). Possibly it is stabilized by the absorption of oxygen and nitrogen during annealing. (The oxynitride $\text{Sm}(\text{O},\text{N})$ has a lattice constant of $a=5.03$ Å and the difference in lattice constant shows clearly that carbon is in the structure; for the relationship between the NaCl-type oxynitrides, carbides and the Sm high pressure phase, see the discussion in Chapter 4.) The presence of the Sm carbide results in the precipitation of α -Fe.

The transformation between $\text{Sm}_2\text{Fe}_{17}\text{C}_{1.0}$ and $\text{Sm}_2\text{Fe}_{14}\text{C}$ ($\text{Sm}_2\text{Fe}_{17}\text{C}_{1.0} \rightarrow \text{Sm}_2\text{Fe}_{14}\text{C}$ above 750 C and $\text{Sm}_2\text{Fe}_{14}\text{C} \rightarrow \text{Sm}_2\text{Fe}_{17}\text{C}_{1.0}$ at 1040 C) is always accompanied by the formation of or reaction with α -Fe. Our XRD and TMA analysis has established that the transformation proceeds as:



For simplicity, however, the α -Fe phase will not usually be mentioned when addressing the transformation, unless necessary.

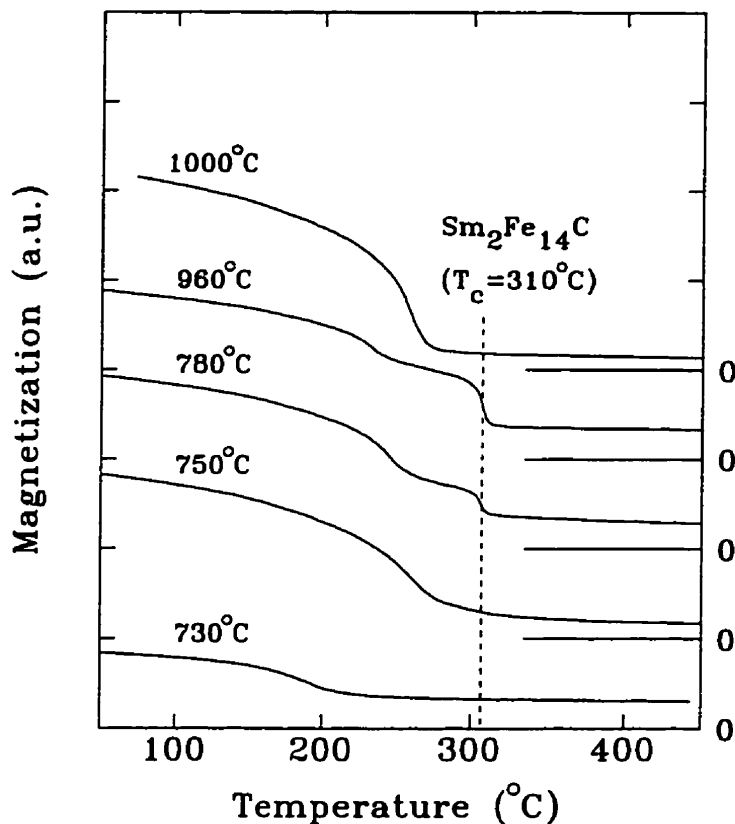


Figure 5.8: TMA scans of samples corresponding to the XRD scans in Fig. 5.6.

The XRD and TMA scans in Fig. 5.6 and Fig. 5.8 are performed on samples heated to appropriate temperatures at 40 C/min, followed by fast cooling. It is observed that when the samples are held at those temperatures a phase transformation from $\text{Sm}_2\text{Fe}_{17}\text{C}_{1.0}$ to $\text{Sm}_2\text{Fe}_{14}\text{C}$ proceeds. For example, even though after heating to 750 C at 40 C/min followed by fast cooling the powder is almost single phase $\text{Sm}_2\text{Fe}_{17}\text{C}_{1.0}$, maintaining the sample at 750 C for 2 h leads to a complete transformation to $\text{Sm}_2\text{Fe}_{14}\text{C}$. This observation suggests that the formation of $\text{Sm}_2\text{Fe}_{17}\text{C}_{1.0}$ can be kinetically favored even though 2-14-1 is the thermodynamically stable phase.

We therefore conclude that $\text{Sm}_2\text{Fe}_{14}\text{C}$ is a low temperature phase (LTP) that is stable below a transition temperature, T_t ; above this temperature it transforms into $\text{Sm}_2\text{Fe}_{17}\text{C}_{1.0}$, which we call the high temperature phase (HTP). The term “high temperature phase” is used to denote the carbide $\text{Sm}_2\text{Fe}_{17}\text{C}_x$ of $x=1.0$, but not other x values as is further explained on page 104.

5.2.2 The phase formation under different annealing conditions

The influence of the heating rate:

The phase transformation between 750 C and T_t is very sensitive to the detailed conditions of the heat treatment, reflecting competition between the kinetically favored HTP and the thermodynamically favored LTP. The phases formed at 960 C for various heating rates are demonstrated by the TMA scans in Fig. 5.9. Low heating rates favor, and high heating rates suppress, the formation of LTP. At a heating rate of 15 C/min there is only a very small amount of HTP in the 960 C powders, implying that HTP has been transformed into LTP; whereas at the rate of 80 C/min no LTP is seen in the 960 C powders, suggesting that the HTP→LTP transformation has not occurred. The dependence of the transformation on the heating rate is a reflection of the competition between the kinetics of both grain growth in the $\text{Sm}_2\text{Fe}_{17}\text{C}_{1.0}$ phase and the overall HTP→LTP transformation. In Section 5.5.2 we will see that the HTP→LTP transformation is critically dependent on the grain sizes of the $\text{Sm}_2\text{Fe}_{17}\text{C}_{1.0}$ HTP and that the HTP→LTP transformation drops drastically with the increase of grain sizes of the HTP. Suppression of the HTP→LTP transformation at high heating rate is possibly caused by the grain growth of the HTP. A detailed study on the phase transformation from the HTP $\text{Sm}_2\text{Fe}_{17}\text{C}_{1.0}$ to the LTP $\text{Sm}_2\text{Fe}_{14}\text{C}$ below the transition temperature is presented in Section 5.5.2.

Isothermal annealing at relatively low temperatures:

The study in Section 5.2.1 has shown that $\text{Sm}_2\text{Fe}_{14}\text{C}$ is the low temperature phase and is formed by heating to above 750 C at 40 C/min. In this section, the formation of $\text{Sm}_2\text{Fe}_{14}\text{C}$ below this temperature is investigated. For this purpose, long-time isothermal annealing was carried out on the mechanically alloyed $\text{Sm}_2\text{Fe}_{17}\text{C}_{1.0}$ and $\text{Sm}_2\text{Fe}_{14}\text{C}$ powders at relatively low temperatures, between 600 C and 700 C.

The formation kinetics of $\text{Sm}_2\text{Fe}_{14}\text{C}$ are very sluggish. After 32 h annealing at 600 C the powder is still in the multi-phase state, $\text{Sm}_2\text{Fe}_{17}$, SmFeC , SmC_y , and $\alpha\text{-Fe}$. The corresponding XRD and TMA scans are similar to the 730 C scans in Fig. 5.6 and Fig. 5.8, respectively. A closeup plot of the TMA scan around the Curie temperature of the 2-14-1 shows the presence of that phase in only a few volume percent, implying that 2-14-1 is indeed the low-temperature equilibrium phase but that the formation

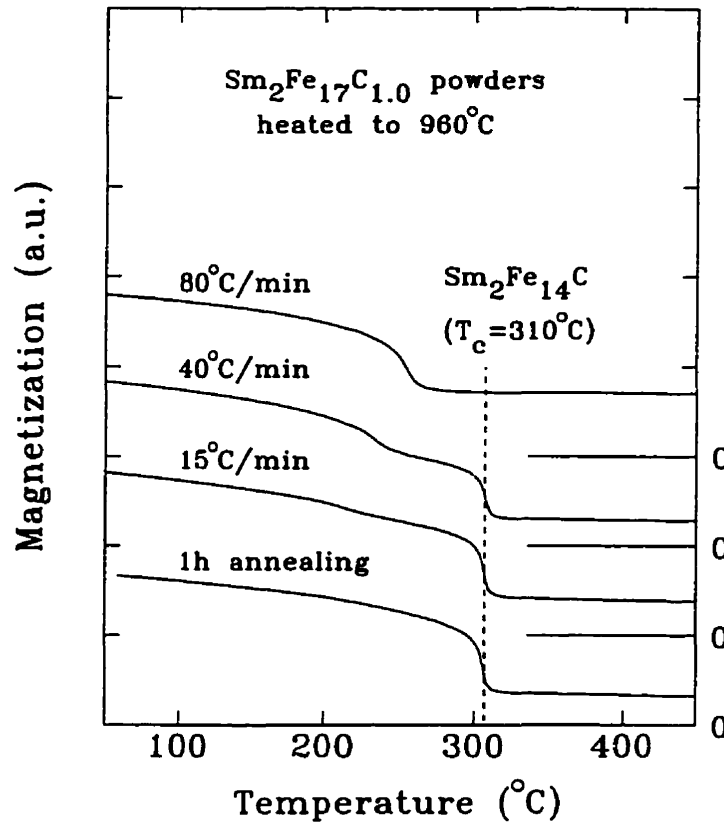


Figure 5.9: TMA scans of mechanically alloyed $\text{Sm}_2\text{Fe}_{17}\text{C}_{1.0}$ powder heated to 960 C at various heating rates. There is a higher α -Fe amount in the 80 C/min powder due to the presence of a large amount of $\text{SmC}_{0.06}$ (refer to Eq. 5.4) as detected by x-ray diffraction.

kinetics are very slow. Single phase $\text{Sm}_2\text{Fe}_{14}\text{C}$ can be formed by annealing of the $\text{Sm}_2\text{Fe}_{14}\text{C}$ powder at 650 C for long times, more than 2 days. Formation of 2-14-1 at higher temperature is of course faster. Annealing at 700 C for 3 h yields single phase $\text{Sm}_2\text{Fe}_{14}\text{C}$ compound.

It is noticed that the intermediate states of the powders during the isothermal annealing (that is, the powders annealed at 650 C for less than 2 days or at 700 C for less than 3 h) does not contain $\text{Sm}_2\text{Fe}_{17}\text{C}_{1.0}$, the phase that is kinetically favored above 750 C according to the study in Section 5.2.1. $\text{Sm}_2\text{Fe}_{14}\text{C}$ forms directly from the mixture of phases, $\text{Sm}_2\text{Fe}_{17}$, SmFeC , $\text{SmC}_{0.06}$ and α -Fe, as seen from the XRD measurements. There could be either of the following two reasons for the absence of the $\text{Sm}_2\text{Fe}_{17}\text{C}_{1.0}$ phase: (1) the $\text{Sm}_2\text{Fe}_{17}\text{C}_{1.0}$ did form from the mixture phases but the transformation rate to the thermodynamically stable phase, $\text{Sm}_2\text{Fe}_{14}\text{C}$, is much faster

than the formation rate of the $\text{Sm}_2\text{Fe}_{17}\text{C}_{1.0}$, or (2) the free energy of the $\text{Sm}_2\text{Fe}_{17}\text{C}_{1.0}$ is higher than that of the mixture of phases and therefore the $\text{Sm}_2\text{Fe}_{17}\text{C}_{1.0}$ could not be formed; to determine which of the two states has a higher free energy, we have carried out a complementary study of the transformation in samples made by melt spinning.

The melt-spun $\text{Sm}_2\text{Fe}_{17}\text{C}_{1.0}$ ribbons shown in Fig. 5.2 were used. Quantitative x-ray analysis shows that the as-spun ribbons contain 25 vol.% of the $\text{Sm}_2\text{Fe}_{17}\text{C}_{1.0}$ phase, the rest being the amorphous Sm-Fe-C. (The α -Fe content indicated in Fig. 5.2 is less than 2 vol.% and is therefore neglected.) The composition of the amorphous phase is assumed to be the same as $\text{Sm}_2\text{Fe}_{17}\text{C}_{1.0}$. Fig. 5.10 shows the DSC scan for the ribbons. A prominent exothermic peak appears around 600 C with an enthalpy of 3.0 ± 0.3 kJ/g-atom. Annealing around and above the exothermic peak, 600 C, results in the formation of almost single-phase $\text{Sm}_2\text{Fe}_{17}\text{C}_{1.0}$, as shown by the corresponding TMA measurements. The exothermic peak is therefore related to the formation of the $\text{Sm}_2\text{Fe}_{17}\text{C}_{1.0}$. This is probably formed by polymorphic crystallization of the amorphous phase, with a crystallization enthalpy of 4.0 ± 0.4 kJ/g-atom. As shown in Section 5.2.1, $\text{Sm}_2\text{Fe}_{17}\text{C}_{1.0}$ is the stable phase at high temperature. Therefore prolonged annealing must lead to the decomposition of the $\text{Sm}_2\text{Fe}_{17}\text{C}_{1.0}$ even though it is the initial crystallization product from the amorphous matrix. It was indeed observed that 4 h annealing at 600 C results in the partial decomposition of $\text{Sm}_2\text{Fe}_{17}\text{C}_{1.0}$ to form SmFe_3 , SmFe_2 , α -Fe and an unknown Sm-Fe-C phase, but *without* the $\text{Sm}_2\text{Fe}_{14}\text{C}$ phase. The decomposition confirms that the $\text{Sm}_2\text{Fe}_{17}\text{C}_{1.0}$ is unstable at low temperatures, but even though $\text{Sm}_2\text{Fe}_{14}\text{C}$ may be the thermodynamically stable phase, it is not kinetically accessible at 600 C over measurable laboratory time scales. Moreover, the decomposition suggests that the $\text{Sm}_2\text{Fe}_{17}\text{C}_{1.0}$ has a higher free energy than the mixture of phases at 600 C, although the decomposition product of the $\text{Sm}_2\text{Fe}_{17}\text{C}_{1.0}$ ribbon is different from that formed by the annealing of mechanically alloyed powder at the same temperature, implying that at 600 C phase formation is kinetically controlled.

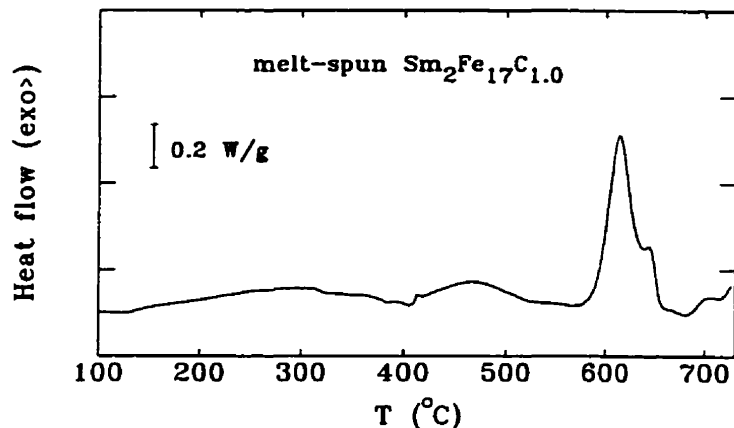


Figure 5.10: DSC heating scan at 40 C/min of the melt-spun $\text{Sm}_2\text{Fe}_{17}\text{C}_{1.0}$ ribbon shown in Fig. 5.2

5.2.3 Summary of the phase formation study

We have shown that $\text{Sm}_2\text{Fe}_{17}\text{C}_{1.0}$ is a high temperature phase, stable above a certain transition temperature ($T_t \leq 1040$ C); below this temperature $\text{Sm}_2\text{Fe}_{14}\text{C}$ is the stable phase. Although not thermodynamically favored below T_t , metastable $\text{Sm}_2\text{Fe}_{17}\text{C}_{1.0}$ may still be formed by being kinetically more favorable. The formation of metastable $\text{Sm}_2\text{Fe}_{17}\text{C}_{1.0}$ below T_t is sensitive to the details of the heat treatment.

Our results have shown the following three routes for the formation of $\text{Sm}_2\text{Fe}_{17}\text{C}_{1.0}$.

1) Below 750 C $\text{Sm}_2\text{Fe}_{17}\text{C}_{1.0}$ is thermodynamically unstable with respect to either a mixture of phases or 2-14-1. It can be formed by crystallization of the amorphous phase, possibly polymorphic, prepared by melt spinning, but cannot be formed in the mechanically alloyed powders because the mixture of phases in the mechanically alloyed powders is more stable than $\text{Sm}_2\text{Fe}_{17}\text{C}_{1.0}$.

2) Between 750 C and T_t $\text{Sm}_2\text{Fe}_{17}\text{C}_{1.0}$ is thermodynamically favored over the mixture of phases or the amorphous state. It may be formed by either the reaction among the phases in the mixture or the crystallization of the amorphous phase. However, with increasing temperature, the kinetics of formation of the equilibrium phase, $\text{Sm}_2\text{Fe}_{14}\text{C}$, becomes comparable to that of $\text{Sm}_2\text{Fe}_{17}\text{C}_{1.0}$. Short annealing and rapid heating and cooling is necessary to avoid the formation of $\text{Sm}_2\text{Fe}_{14}\text{C}$.

3) Above T_t $\text{Sm}_2\text{Fe}_{17}\text{C}_{1.0}$ is the equilibrium phase.

The above phase formation routes imply the following sequence of phases in order of decreasing free energy (*i.e.* of increasing stability); 1) below 750 C the order is

amorphous phase \rightarrow the $\text{Sm}_2\text{Fe}_{17}\text{C}_{1.0}$ \rightarrow phase mixture \rightarrow $\text{Sm}_2\text{Fe}_{14}\text{C}$; 2) between 750 C and T_t the order is amorphous phase \rightarrow phase mixture \rightarrow the $\text{Sm}_2\text{Fe}_{17}\text{C}_{1.0}$ \rightarrow $\text{Sm}_2\text{Fe}_{14}\text{C}$; and 3) above T_t $\text{Sm}_2\text{Fe}_{14}\text{C}$ \rightarrow $\text{Sm}_2\text{Fe}_{17}\text{C}_{1.0}$.

We have therefore shown that metastable $\text{Sm}_2\text{Fe}_{17}\text{C}_{1.0}$ can be prepared by mechanical alloying *without* the need for a structure stabilizer, such as Ga, Si and Al elements. It has been reported that partial substitution of Fe by those elements stabilize the interstitial carbides $\text{Sm}_2\text{Fe}_{17}\text{C}_x$ [138, 139, 144]. However, the trade-off for a more stable 2-17 carbide is the dilution of Fe with the non-magnetic substitution, which results in a reduction of the magnetization of the compound. A recent study by Cao *et al* [145] shows that mechanically alloyed $\text{Sm}_2\text{Fe}_{15}\text{Ga}_2\text{C}_2$ powder crystallizes into single-phase 2-17 carbide $\text{Sm}_2(\text{FeGa})_{17}\text{C}_2$ above 750 C and high coercivity ($\mu_0H=1.5$ T) is achieved in a powder annealed at 850 C for 1 h. As the result of the considerable amount of non-magnetic Ga, the saturation magnetization of $\text{Sm}_2\text{Fe}_{15}\text{Ga}_2\text{C}_2$ is only 80% of that for $\text{Sm}_2\text{Fe}_{17}\text{C}_2$. The smaller magnetization reduces the potential for a high energy product of a magnet.

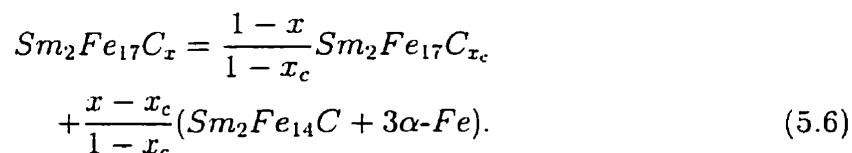
In the present study we have given an in-depth understanding of why and how the $\text{Sm}_2\text{Fe}_{17}\text{C}_x$ may be formed by the non-equilibrium processes, mechanically alloying and melt spinning, below its stable temperature region. This is a very useful result for the development of permanent magnets based on the the $\text{Sm}_2\text{Fe}_{17}\text{C}_x$.

5.3 Critical Carbon Contents in $\text{Sm}_2\text{Fe}_{17}\text{C}_x$

In the above section we have shown that the interstitial carbide $\text{Sm}_2\text{Fe}_{17}\text{C}_{1.0}$ is a high temperature phase that is metastable below the transition temperature, T_t . However, carbon is a non-stoichiometric component in the carbide. As discussed in Chapter 1 there must be a critical carbon content, x_c , for the interstitial carbides $\text{Sm}_2\text{Fe}_{17}\text{C}_x$ that divides the stable from the metastable region. Determining the critical carbon content is one of the major objectives of this thesis. In this section it will be determined from the phase formation in mechanically alloyed $\text{Sm}_2\text{Fe}_{17}\text{C}_x$ powders with a series of carbon contents, $x=0.3, 0.45, 0.85$ and 1.0, over the temperature region between 700 C and 1100 C. For this purpose isothermal annealings between 700 C and 1100 C were performed on the mechanically alloyed powders.

Fig. 5.11 shows the TMA cooling scans for the samples annealed at 800 C for 2 h. Two transitions corresponding to the 2-17 carbide ($T_c \sim 165$ C) and 2-14-1 ($T_c=310$ C), respectively, are clearly seen for $x=0.3$ and 0.45 . For $x=0.85$, the magnetic transition for the $\text{Sm}_2\text{Fe}_{17}$ carbide can only be seen from the heating scan, shown in the inset of Fig. 5.11, but not from the cooling scan¹. The residual magnetization above 310 C is from $\alpha\text{-Fe}$ ($T_c=780$ C). The TMA results are in agreement with those of the XRD measurement: the equilibrium state contains a mixture of 2-17 carbide, 2-14-1 and $\alpha\text{-Fe}$.

It is significant that $\text{Sm}_2\text{Fe}_{17}$ carbides formed by annealing of the various mechanically alloyed $\text{Sm}_2\text{Fe}_{17}\text{C}_x$ powders have the same Curie temperature, $T_c \sim 165$ C (see Fig. 5.11). This reflects that the 2-17 carbides contain the same amount of interstitial carbon atoms which may be expressed as $\text{Sm}_2\text{Fe}_{17}\text{C}_{x_c}$. From the Curie temperature increase and the lattice expansion of the carbide $\text{Sm}_2\text{Fe}_{17}\text{C}_{x_c}$ with respect to $\text{Sm}_2\text{Fe}_{17}$ it is determined that $x_c=0.2$ at 800 C. This is the critical carbon content in the $\text{Sm}_2\text{Fe}_{17}$ structure at 800 C: the carbide with $x < x_c$ is stable; while with $x > x_c$ it is unstable and decomposes into a mixture of $\text{Sm}_2\text{Fe}_{17}\text{C}_{x_c}$, $\text{Sm}_2\text{Fe}_{14}\text{C}$ and $\alpha\text{-Fe}$. The decomposition scheme for the $\text{Sm}_2\text{Fe}_{17}\text{C}_x$ ($x > x_c$) powders can be expressed as



From the above equation, it is obvious that for $x=1.0$, no 2-17 phase will coexist with the 2-14-1 in equilibrium. Decomposition of the $\text{Sm}_2\text{Fe}_{17}\text{C}_{1.0}$ yields $\text{Sm}_2\text{Fe}_{14}\text{C} + 3\alpha\text{-Fe}$.

¹This may be caused by the subtle difference in the magnetic exchange coupling between the 2-17 carbide, which has ultrafine grains and $\text{Sm}_2\text{Fe}_{14}\text{C}$. In the heating scan the magnetization in each magnetic particle is directed relatively at random under the small magnetic field (~ 60 G for the TMA measurements), the magnetic coupling among the relatively randomly oriented magnetizations is relatively weak; whereas in the cooling scan of the TMA measurement the magnetization in each $\text{Sm}_2\text{Fe}_{14}\text{C}$ particle is well aligned along the applied field when cooling through its Curie temperature (the applied field provides a preferential direction for the spontaneous magnetization), and the magnetic moment in the ultrafine 2-17 carbide may be strongly magnetically coupled to the surrounding $\text{Sm}_2\text{Fe}_{14}\text{C}$ grains leading to a smearing-out of the spontaneous magnetization in the carbide. In fact the magnetic exchange coupling between grains of the same (different) magnetic phase(s) has been reported[146, 147, 148, 149].

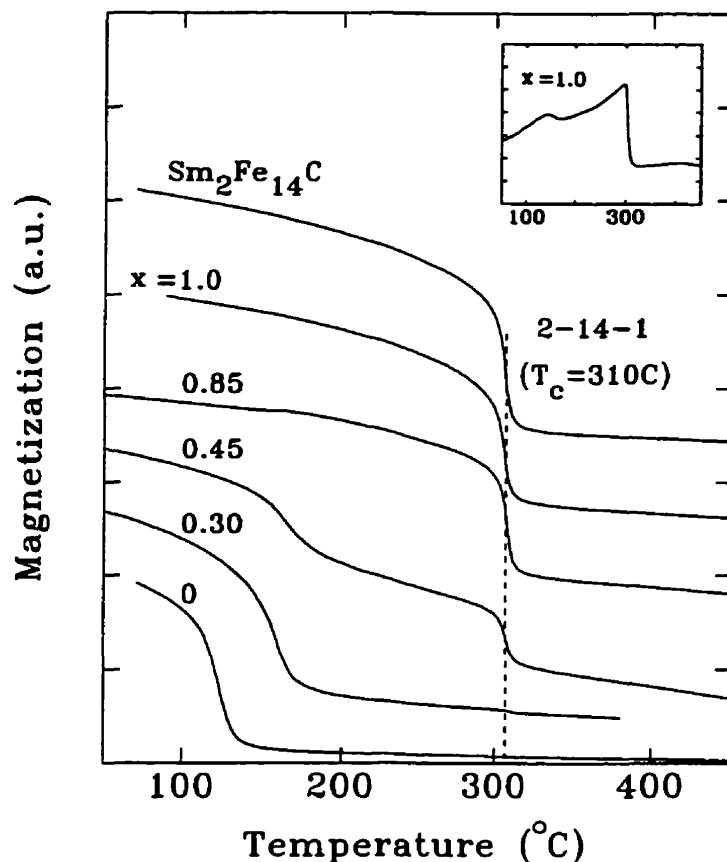


Figure 5.11: TMA cooling scans of mechanically alloyed $\text{Sm}_2\text{Fe}_{17}\text{C}_x$ ($x=0, 0.3, 0.45, 0.85$ and 1.0) and $\text{Sm}_2\text{Fe}_{14}\text{C}$ powders after annealing at 800 C for 2 h . Inset: TMA heating scan showing the magnetic transition for $\text{Sm}_2\text{Fe}_{17}\text{C}_x$ around 165 C .

This has been seen from the study of the previous section. Therefore, $\text{Sm}_2\text{Fe}_{17}\text{C}_{1.0}$ is a *true* high temperature phase that is stable only above the transition temperature T_t^1 ; below T_t , the stable phase belongs to $\text{Sm}_2\text{Fe}_{14}\text{C}$ (plus $\alpha\text{-Fe}$).

¹In 2-17 carbide, carbon is a non-stoichiometric component. It cannot be, therefore, generalized that the 2-17 carbide is a high temperature phase. $x=1.0$ is the maximum carbon content for a stable $\text{Sm}_2\text{Fe}_{17}\text{C}_x$. Even though $\text{Sm}_2\text{Fe}_{17}\text{C}_x$ with $x > 1.0$ can be prepared by low temperature reaction between $\text{Sm}_2\text{Fe}_{17}$ and carbon (graphite), it is metastable through the whole temperature range up to 1150 C ; the maximum carbon content for the stable $\text{Sm}_2\text{Fe}_{17}$ carbide occurs at around 1150 C and is 1.0 . Furthermore, it is not necessary that, for other R_2Fe_{17} compounds, the maximum carbon content for a stable R_2Fe_{17} carbide is $x=1.0$. In fact, for the rare earths heavier than Sm , the maximum values can be considerably larger than 1.0 [138, 139]. Whereas, in $\text{Nd}_2\text{Fe}_{17}$ the maximum may be $x=0.6$ [21, 150]. All those maximum x 's are for the high temperature phase, which can be obtained by high temperature annealing at around 1100 C of the cast alloys or by rapidly quenching

Table 5.2 lists the results from isothermal annealing of mechanically alloyed $\text{Sm}_2\text{Fe}_{17}\text{C}_x$ ($x=0.3, 0.45$ and 0.85) powders. The critical carbon content in the 2-17 phase, x_c , and the volume ratio of 2-14-1 to $\text{Sm}_2\text{Fe}_{17}\text{C}_{x_c}$, f_{meas} , is obtained from the TMA measurements. The value in the parentheses is calculated from Eq. 5.6,

$$f_{calc} = (x - x_c)/(1 - x). \quad (5.7)$$

Agreement between the measured and the calculated values is very good except for low x at low temperature, *i.e.* for $x=0.3$ at 700 C and 800 C and for $x=0.45$ at 700 C. This is because the annealing time was not long enough to reach equilibrium. For example, the annealing time was 3 h at 700 C and 2 h at 800 C, respectively. The annealing time was adopted in accordance with the results on the mechanically alloyed $\text{Sm}_2\text{Fe}_{14}\text{C}$ powders, which is the time required to form single phase $\text{Sm}_2\text{Fe}_{14}\text{C}$. For the $\text{Sm}_2\text{Fe}_{17}\text{C}_x$ powders of low carbon content, the formation of 2-14-1 is slow possibly because the driving force is small (see Section 5.4 for the driving force). After 12 h annealing at 700 C, f_{meas} agrees with f_{calc} .

The temperature dependence of the critical carbon content is plotted in Fig. 5.12. A critical carbon content at a certain temperature is the maximum amount of carbon atoms that can be dissolved in the interstitial sites of the 2-17 structure at equilibrium and the excess amount of carbon is expelled out from the 2-17 structure in the form of 2-14-1. The critical content may therefore be taken as the solubility of carbon in the 2-17 structure. Regarding the carbon solubility, it has been derived, using the standard method of statistical mechanics for the solid phase reaction between carbon and the $\text{Sm}_2\text{Fe}_{17}$, that[151] $x_c = x_m(1 + \exp(U_0/k_B T))^{-1}$, where x_m is the maximum solubility, U_0 is the net reaction energy and k_B is Boltzmann's constant. Least-square fit of the data in Fig. 5.12 with this expression gives $x_m = 6.6 \times 10^{2 \pm 0.3}$ and $U_0 = 72 \pm 11 \text{ kJ/mol}$. The reaction energy U_0 is a large and positive value, in sharp contrast with the reaction enthalpy between the $\text{Sm}_2\text{Fe}_{17}$ compound and graphite C, $H_C = -20 \text{ kJ/mol}$ measured by DSC[152]. The difference in the two energies reflects from the melts. It is therefore proper to use "high temperature phase" to denote the particular R_2Fe_{17} carbide which has the maximum x for the stable $\text{R}_2\text{Fe}_{17}\text{C}_x$ structure.

Table 5.2: Equilibrium balance between the 2-17 carbide and 2-14-1. T_c and f_{meas} is the Curie temperature of the 2-17 carbide and the 2-14-1 to 2-17 (volume) ratio obtained from the TMA measurements. x_c is the critical carbon content in the 2-17 carbide. f_{calc} is the value calculated from Eq. 5.7.

Temperature	x = 0.3		x = 0.45		x = 0.85	
	T_c (x_c)	f_{meas} (f_{calc})	T_c (x_c)	f_{meas} (f_{calc})	T_c (x_c)	f_{meas} (f_{calc})
700 C	165 C (0.10*)	0.03 (0.25)	176 C (0.16*)	0.22 (0.52)	184 C (0.21*)	2.7 (0.30)
800 C	161 C (0.18*)	0.02 (0.14)	168 C (0.22*)	0.48 (0.42)	168 C (0.22*)	5.0 (3.0)
900 C	173 C (0.3)	0 (0)	172 C (0.3)	0.44 (0.31)	181 C (0.32*)	2.4 (2.4)
1000 C	— —	— —	217 C (0.45)	0 (0)	230 C (0.52*)	2.1 (1.4)
1100 C	— —	— —	— —	— —	255 (0.85)	0 (0)

*The carbon content is extrapolated from the Curie temperature.

the fact that the carbon solubility measured here is relative to 2-14-1, not to pure carbon. It is also noted that the maximum solubility, $x_m \sim 660$, is much larger than the available interstitial sites for carbon atoms in the 2-17 structure ($x_m = 3$, see Section 2.1.2). To overcome the difficulties arising with the expression for the carbon solubility, we introduce a free energy sketch for the Sm-Fe-C system in the following section.

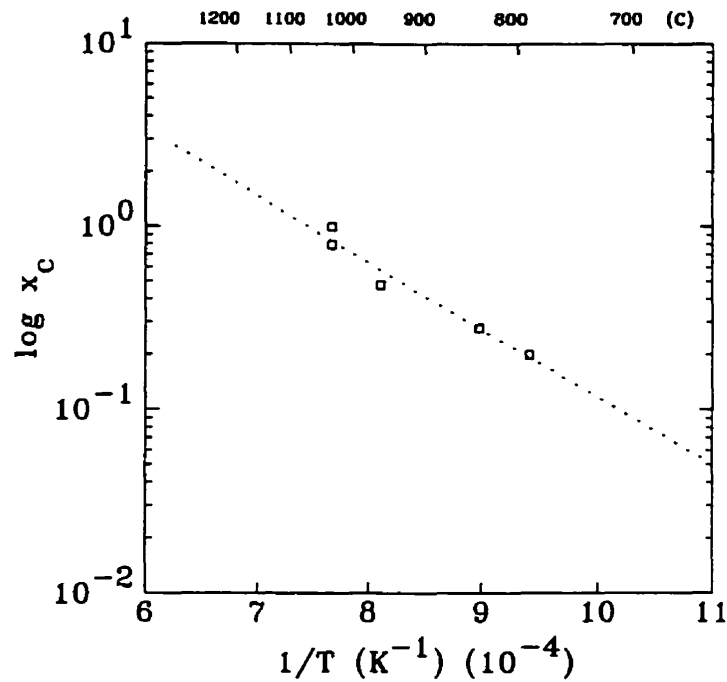


Figure 5.12: Carbon solubility (the critical carbon content), x_c , in $\text{Sm}_2\text{Fe}_{17}$ structure as a function of temperature. Dashed line shows the fitting with $x_c = x_m(1 + \exp(U_0/k_B T))^{-1}$

5.4 Thermodynamic Relation Between the 2-14-1 and 2-17 Carbide

As studied in the preceding section the balance between the two components $\text{Sm}_2\text{Fe}_{17}\text{C}_{x_c}$ and $(\text{Sm}_2\text{Fe}_{14}\text{C}+3\alpha\text{-Fe})$ obeys the lever rule expressed in Eq. 5.6. The feature of the equilibrium balance between the 2-14-1 and 2-17 is better understood using a free energy sketch in terms of a pseudo-binary system of $\text{Sm}_2\text{Fe}_{17}$ and C, as shown in Fig. 5.13. The equilibrium balance is reached by minimizing the free energy of the system, which is determined by the common tangent between the free energy curves of the $(\text{Sm}_2\text{Fe}_{14}\text{C}+3\alpha\text{-Fe})$ and $\text{Sm}_2\text{Fe}_{17}\text{C}_x$.

As a good approximation, the free energy for the $\text{Sm}_2\text{Fe}_{17}\text{C}_x$ phase can be expressed as

$$\begin{aligned}\Delta G_{2-17-C_x} &= xH_C - TS^c + \Delta G_{2-17}, \\ \Delta G_{2-17} &= \Delta G_{2-17-C_x}|_{x=0},\end{aligned}\tag{5.8}$$

where the temperature T is in Kelvin, H_C (~ 20 kJ/mol) is the reaction enthalpy

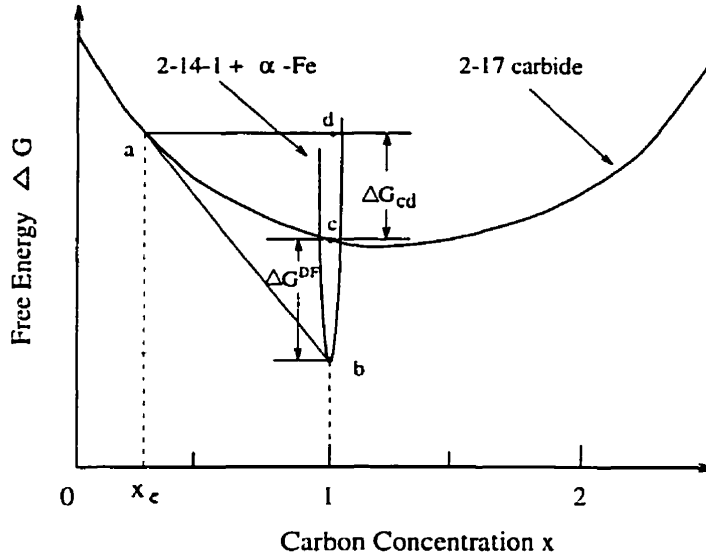


Figure 5.13: Schematic free energy for $\text{Sm}_2\text{Fe}_{17}\text{-C}$ pseudo-binary system.

between $\text{Sm}_2\text{Fe}_{17}$ and C (graphite), S^c is the configurational entropy contributed from the dissolving of interstitial carbon in the 2-17 structure and ΔG_{2-17} is the free energy of the binary $\text{Sm}_2\text{Fe}_{17}$ with respect to the elemental states of Sm and Fe. For the configurational entropy we have

$$\begin{aligned} S^c(x) &= k_B \ln w \\ &= R \left(x_m \ln \frac{x_m}{x_m - x} + x \ln \frac{x_m - x}{x} \right), \end{aligned} \quad (5.9)$$

where, $R=8.31$ J/mol-K and w is the number of configurations of distributing x number of carbon atoms in the x_m ($=3$) possible interstitial sites.

Based on Eq. 5.8, Eq. 5.9 and the free energy sketch in Fig. 5.13, the temperature dependence of the critical carbon content can be determined from (see Appendix A.1)

$$\begin{aligned} \chi &= \left(x_m \ln \frac{x_m}{x_m - x_c} + \ln \frac{x_m - x_c}{x_c} \right) \\ &= \frac{[\Delta S' + S^c(1)]}{R} - \frac{\Delta H'}{R} \frac{1}{T}, \end{aligned} \quad (5.10)$$

where $\Delta H'$ ($\Delta S'$) is the enthalpy (entropy) difference between the 2-14-1 and the $\text{Sm}_2\text{Fe}_{17}\text{C}_{1.0}$. If we plot χ as a function of T^{-1} , the slope will give $-\Delta H'/R$ and the intercept $(\Delta S' + S^c(1))/R$. The dashed line in Fig. 5.14 shows the least-squares fit with Eq. 5.10 which gives

$$\Delta H' = -(5.2 \pm 0.4) \times 10^3 R = -(43 \pm 4) \text{ kJ/mol}$$

$$\Delta S'' = \Delta S' + S^c(1) = -(2.1 \pm 0.3)R = -(17 \pm 3) \text{ J/mol-K} \quad (5.11)$$

where $S^c(1)=1.9R$ as calculated from Eq. 5.9; hence $\Delta S'=-4.0R=-33 \text{ J/mol-K}$.

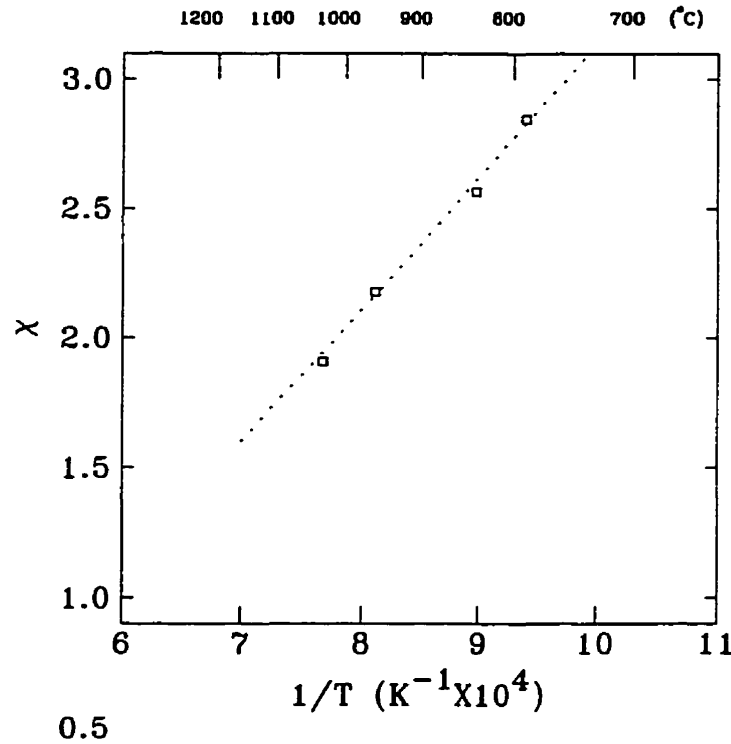


Figure 5.14: A plot of $\chi = (x_m \ln \frac{x_m}{x_m - x_c} + \ln \frac{x_m - x}{x_c})$ as a function of T^{-1}

Summary:

The present study has therefore established the temperature dependence of the critical carbon content, quantitatively described by Eq. 5.10. For a certain temperature there is a critical carbon content, x_c , which is the maximum value for a stable 2-17 carbide. Put the other way round, for a given carbon content, x , in the 2-17 structure there is a critical temperature, T_{cr} , which divides the stable from the metastable region. The critical temperature can be determined from

$$\begin{aligned} \chi &= \left(x_m \ln \frac{x_m}{x_m - x} + \ln \frac{x_m - x}{x} \right) \\ &= \frac{[\Delta S' + S^c(1)]}{R} - \frac{\Delta H'}{R} \frac{1}{T_{cr}} \end{aligned} \quad (5.12)$$

At temperatures higher than T_{cr} the 2-17 carbide is the stable phase, while at lower temperatures, 2-14-1 (plus α -Fe) is formed to reduce the carbon content in

the carbide. The stable phase state is the mixture of $\text{Sm}_2\text{Fe}_{17}\text{C}_{x_c}$, $\text{Sm}_2\text{Fe}_{14}\text{C}$ and $\alpha\text{-Fe}$. Both $\text{Sm}_2\text{Fe}_{14}\text{C}$ and $\alpha\text{-Fe}$ are soft magnetic phases and, therefore, must be avoided during the production of permanent magnets. As we have addressed in Chapter 1, $\text{Sm}_2\text{Fe}_{17}\text{C}_x$ for $x=0.5\text{--}1.0$ has suitable magnetic anisotropy to produce magnets with good grain alignment by the sintering process. From Eq. 5.12 the critical temperature for $x=0.5$ and 1.0 is 950 C and 1020 C respectively. Sintering of the carbides must therefore be carried out at temperatures above the corresponding critical temperature. These temperatures, 950 C and 1020 C , match the required ones for the sintering process and, therefore, the present results are very useful for the development of sintered magnets based on the $\text{Sm}_2\text{Fe}_{17}\text{C}_x$ precursors. It should be stressed however that Eq. 5.10 or 5.12 is only valid for low carbon concentration, $x \leq 1.0$ and may not be applied for $1.0 < x < x_m$. In fact, in $\text{Sm}_2\text{Fe}_{17}\text{C}_x$ ($x > 1.0$) powders prepared by ball milling and subsequent annealing, we have observed a Sm-rich phase, $\text{Sm}_2\text{Fe}_2\text{C}_3$ [142, 153].

The phase transformation is driven by the difference in the free energy between the initial and final states, the so-called driving force. Eq. 5.10 also allows us to determine the driving force for the phase transformation from $\text{Sm}_2\text{Fe}_{17}\text{C}_{1.0}$ to $\text{Sm}_2\text{Fe}_{14}\text{C}$. The driving force is thus calculated as

$$\begin{aligned}\Delta G^{DF} &= |\Delta G'| = |\Delta H' - T\Delta S'| \\ &= (43000 - 33T) \quad J/mol\end{aligned}\quad (5.13)$$

ΔG^{DF} is 9.2 kJ/mol (0.46 kJ/g-atom) at 750 C and decreases linearly with increasing temperature. It vanishes at 1020 C , the transition temperature between the LTP $\text{Sm}_2\text{Fe}_{14}\text{C}$ and the HTP $\text{Sm}_2\text{Fe}_{17}\text{C}_{1.0}$. This driving force is small in comparison to other transformation processes, such as the crystallization of amorphous materials. The small driving force is possibly one of the main reason that the HTP \rightarrow LTP transformation is so slow, as observed in Section 5.2. The kinetics of the transformation and its dependence on the grain size is studied in the next section.

5.5 Phase Transformation from $\text{Sm}_2\text{Fe}_{17}\text{C}_{1.0}$ to $\text{Sm}_2\text{Fe}_{14}\text{C}$

In this section the grain-size dependence of the transformation from $\text{Sm}_2\text{Fe}_{17}\text{C}_{1.0}$ to $\text{Sm}_2\text{Fe}_{14}\text{C}$ is studied. As we have seen in Section 5.2, $\text{Sm}_2\text{Fe}_{17}\text{C}_{1.0}$ below 1020 C may

be formed under certain kinetically favorable conditions even though $\text{Sm}_2\text{Fe}_{14}\text{C}$ is the true stable phase. It may then transform into $\text{Sm}_2\text{Fe}_{14}\text{C}$. However the transformation has a peculiar behavior: HTP $\text{Sm}_2\text{Fe}_{17}\text{C}_{1.0}$ formed by annealing above the transition temperature is apparently stable even when subjected to annealing below the transition temperature. This was first reported by de Mooij *et al*[21]. We have observed that $\text{Sm}_2\text{Fe}_{17}\text{C}_{1.0}$ prepared by annealing at 1150 C for 5 h was stable even after annealing between 800 C and 900 C for up to 1 day, in sharp contrast to $\text{Sm}_2\text{Fe}_{17}\text{C}_{1.0}$ formed by low temperature annealing of mechanically alloyed powders or melt-spun ribbons, which transformed readily into 2-14-1 at 800 C. For a complete understanding, the conditions related to the stability of this phase must be explained.

We believe that the difference in the stability of the two $\text{Sm}_2\text{Fe}_{17}\text{C}_{1.0}$ samples is a result of different microstructures. The most significant difference is the grain size. The grain sizes in the $\text{Sm}_2\text{Fe}_{17}\text{C}_{1.0}$ compound prepared by annealing at 1150 C for 5 h are between 50 μm and 100 μm , as determined by an optical microscope; that prepared by annealing the mechanically alloyed powders to 750 C is 50 nm as determined from the XRD peak broadening analysis (Fig. 5.6). The much smaller grain size in the low temperature sample (3 orders of magnitude smaller than that in the high temperature one) is the main reason that the HTP \rightarrow LTP transformation proceeds far more readily. In order to further elucidate the effect of grain size on this transformation, a study was therefore carried out on the kinetics of the phase transformation as a function of grain size.

5.5.1 Grain Refinement Processes

The first task was to prepare $\text{Sm}_2\text{Fe}_{17}\text{C}_{1.0}$ samples of various grain sizes. Ball milling was used as the principal process for the grain refinement. Melt spinning was also used as a supplementary method for the preparation of fine grain samples.

As seen in Section 5.2, high energy ball milling and melt spinning at high quench rates results in partial amorphization of $\text{Sm}_2\text{Fe}_{17}\text{C}_{1.0}$. The presence of the amorphous phase may strongly influence the effect of grain size on the transformation. Therefore, for the present study fine grain samples have been prepared at a moderate ball milling energy or at a moderate quench rate in order to avoid the amorphization.

A variety of $\text{Sm}_2\text{Fe}_{17}\text{C}_{1.0}$ samples with different grain sizes have been prepared

with the two methods¹. Table 5.3 is a summary of the grain sizes in the various samples.

Table 5.3: A list of the average grain sizes in the various $\text{Sm}_2\text{Fe}_{17}\text{C}_{1.0}$ samples that have been prepared in this work. The grain sizes are determined either by x-ray analysis or SEM observations.

	ball milling time				melt-spinning wheel speed	
	20 min	1 h	3 h	9 h	7 m/s	30 m/s
grain size	~500 nm	~200 nm	70 nm	40 nm	~500 nm	200-300 nm ^a

^a The grain sizes are determined by both x-ray analysis and SEM observation and the results from the two methods are consistent.

The grain sizes listed are determined either by x-ray analysis or SEM observations. In x-ray analysis the grain sizes are determined from the widths of the corresponding Bragg peaks in samples annealed at around 480 C for 10 h. At that temperature strains in the ball milled powders or melt spun ribbons are effectively annealed out while grain sizes remain the same. It must be stressed that $\text{Sm}_2\text{Fe}_{17}\text{C}_{1.0}$ is stable at low temperature; annealing at around 480 C does not lead to the transformation to $\text{Sm}_2\text{Fe}_{14}\text{C}$. The annealing is used to reduce the broadening of the Bragg peaks caused by the strains, which yields an improved accuracy in determining the grain sizes by the x-ray analysis (see Chapter 3 for the microstructure analysis from the XRD patterns). The limit for the grain size determination by the x-ray analysis is about 200 nm. For grains larger than 200 nm the broadening of the Bragg peaks related to the size effect is difficult to deconvolute from the intrinsic instrumental broadening as the x-ray diffractometer has an instrumental resolution of 0.2° .

Grain refinement process is a key for achieving high coercivity. The present method of producing fine grains of $\text{Sm}_2\text{Fe}_{17}\text{C}_{1.0}$ by ball milling could be a useful technique

¹The ball milling samples were prepared by two processing routes: (1) Ball milling of single-phase $\text{Sm}_2\text{Fe}_{17}\text{C}_{1.0}$ (for 20 min and 1 h milling), and (2) ball milling of a mixture of $\text{Sm}_2\text{Fe}_{17}$ /graphite followed by carbiding heat-treatment (for 3 h and 9 h milling). For details, see Chapter 3 and Refs. [152], [154], [155].

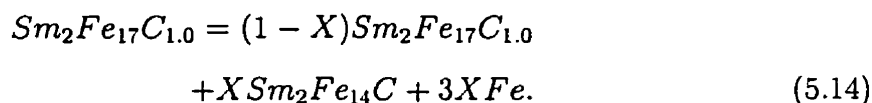
for the production of permanent magnet. In fact, after nitriding, high coercivity ($H_c=16$ kOe) has been achieved in a fine grain powder of Sm_2Fe_{17} carbide prepared by ball milling[154]. In addition, the powders prepared by this method contain highly anisotropic particles that could be aligned in a magnetic field[154, 155]. This is important for achieving a high energy product for a permanent magnet.

5.5.2 Grain Size Dependence of Volume Fraction Kinetics

To study the phase transformation, the $Sm_2Fe_{17}C_{1.0}$ samples are annealed at 800 C. Samples were put into a steel or Ta container and sealed inside a quartz tube under purified Ar. The whole handling procedure were carried out inside the glove box. For annealing, the quartz tube was then placed into a furnace at 800 C. The temperature of the sample during heating was monitored with a thermocouple. Fig. 5.15 shows the temperature variation of the sample as a function of time during the heating up. For a furnace temperature of 800 C, the sample temperature reaches 760 C in 90 s and 790 in 120 s. We usually take 100 s as the time required for the sample to reach the furnace temperature with an error of ± 30 s. After a certain annealing period the tube was quenched into water. The sample was then measured with XRD and TMA to detect any phase transformation and determine the transformed volume fraction. In this way the volume fraction kinetics at isothermal annealing was obtained.

Fig. 5.16 shows the TMA scans for a $Sm_2Fe_{17}C_{1.0}$ carbide after annealing at 800 C for various times. The $Sm_2Fe_{17}C_{1.0}$ has an average grain size of 70 nm prepared by ball milling for 3 h. From the TMA scans, it is clearly seen that, after an incubation time (≥ 1.4 min), a magnetic phase with the Curie temperature $T_c=310$ C appears. This Curie temperature indicates that the phase is $Sm_2Fe_{14}C$, as confirmed by x-ray diffraction measurements. The $Sm_2Fe_{14}C$ phase grows at the expense of the $Sm_2Fe_{17}C_{1.0}$ matrix. The TMA scans for 45 min and 2.5 h are almost identical, suggesting the transformation to $Sm_2Fe_{14}C$ is completed.

The phase transformation in the $Sm_2Fe_{17}C_{1.0}$ can be expressed by the following expression:



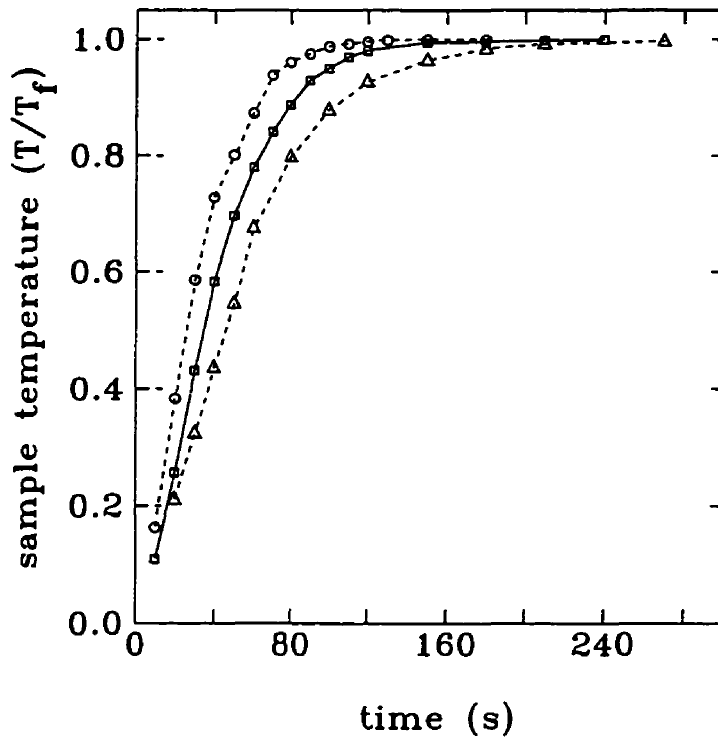


Figure 5.15: The variation of the sample temperature during the heating up in a furnace at temperature T_f (C). The sample temperature T (C) is normalized by the furnace temperature T_f . ○: $T_f=1000$ C; □: $T_f=800$ C; △: $T_f=600$ C.

Here X is the atomic fraction of the transformed $\text{Sm}_2\text{Fe}_{14}\text{C}$ which is a good approximation of the volume fraction. It can be calculated from the measured magnetizations associated with $\text{Sm}_2\text{Fe}_{17}\text{C}_{1.0}$ and $\text{Sm}_2\text{Fe}_{14}\text{C}$ by the equation

$$X = \frac{M_{2-14-1}/\mu_{2-14-1}}{M_{2-14-1}/\mu_{2-14-1} + M_{2-17/C}/\mu_{2-17/C}}. \quad (5.15)$$

Where $M_{2-17/C}$ and M_{2-14-1} are the saturation magnetizations at 0 K for $\text{Sm}_2\text{Fe}_{17}\text{C}_{1.0}$ and $\text{Sm}_2\text{Fe}_{14}\text{C}$ respectively, and $\mu_{2-17/C}(=34.0 \mu_B)$ and $\mu_{2-14-1}(=30.4 \mu_B)$ the magnetic moments per formula unit respectively. The relative saturation magnetizations determined by the TMA measurements were room temperature values. According to [156] and [157], they are 88% of $M_{2-17/C}$ and 93% of M_{2-14-1} , respectively. The temperature effect was taken into account for the determination of X using Eq. 5.15. In this method, the sensitivity is about 1% and the relative error is $\pm 10\%$ in determining X .

For $\text{Sm}_2\text{Fe}_{17}\text{C}_{1.0}$ samples of various grain sizes (listed in Table 5.3), the transformed

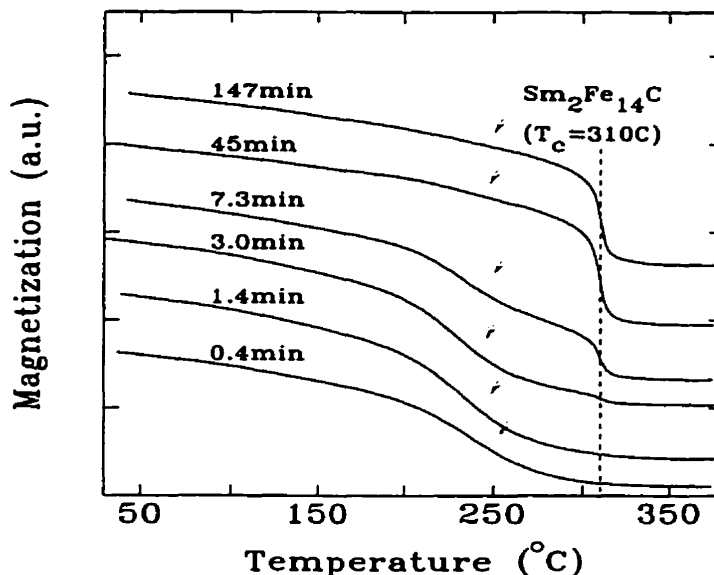


Figure 5.16: The TMA scans of a $\text{Sm}_2\text{Fe}_{17}\text{C}_{1.0}$ carbide after annealed at 800 C for various times. The $\text{Sm}_2\text{Fe}_{17}\text{C}_{1.0}$ has an average grain size of 70 nm prepared by ball milling for 3 h. $\text{Sm}_2\text{Fe}_{14}\text{C}$ has a Curie temperature of 310 C and $\text{Sm}_2\text{Fe}_{17}\text{C}_{1.0}$ has a Curie temperature of about 260 C as indicated with the arrows in the figure.

$\text{Sm}_2\text{Fe}_{14}\text{C}$ volume fraction as a function of time during the isothermal annealing at 800 C is depicted in Fig. 5.17. It is evident that the transformation proceeds faster in samples of smaller grains and the annealing time for a complete transformation varies from 15 min for the 40 nm-grain sample to longer than 28 h for the 200 nm sample.

Fig. 5.18 illustrates the annealing time, $t_{1/2}$, required to reach $X=0.5$ as a function of the grain sizes. The half-time of transformation, $t_{1/2}$, increases with the grain sizes pronouncedly. A least-squares fit with a power-law function gives

$$t_{1/2} = 0.1d^{2.0 \pm 0.5} \quad (5.16)$$

where the grain size, d , is in nanometers and that of time is in seconds. The significance of the power or the scaling factor, 2.0 ± 0.5 , will be discussed in Section 5.5.3 Using the above equation, the half-time, at a temperature of 800 C, for 1 μm -grain $\text{Sm}_2\text{Fe}_{17}\text{C}_{1.0}$ is about 30 hour and that for 10 μm -grain sample is 3 year. The 10 μm -grain $\text{Sm}_2\text{Fe}_{17}\text{C}_{1.0}$ is therefore practically stable at 800 C.

In studies of phase transformations, it is customary to describe the transformed

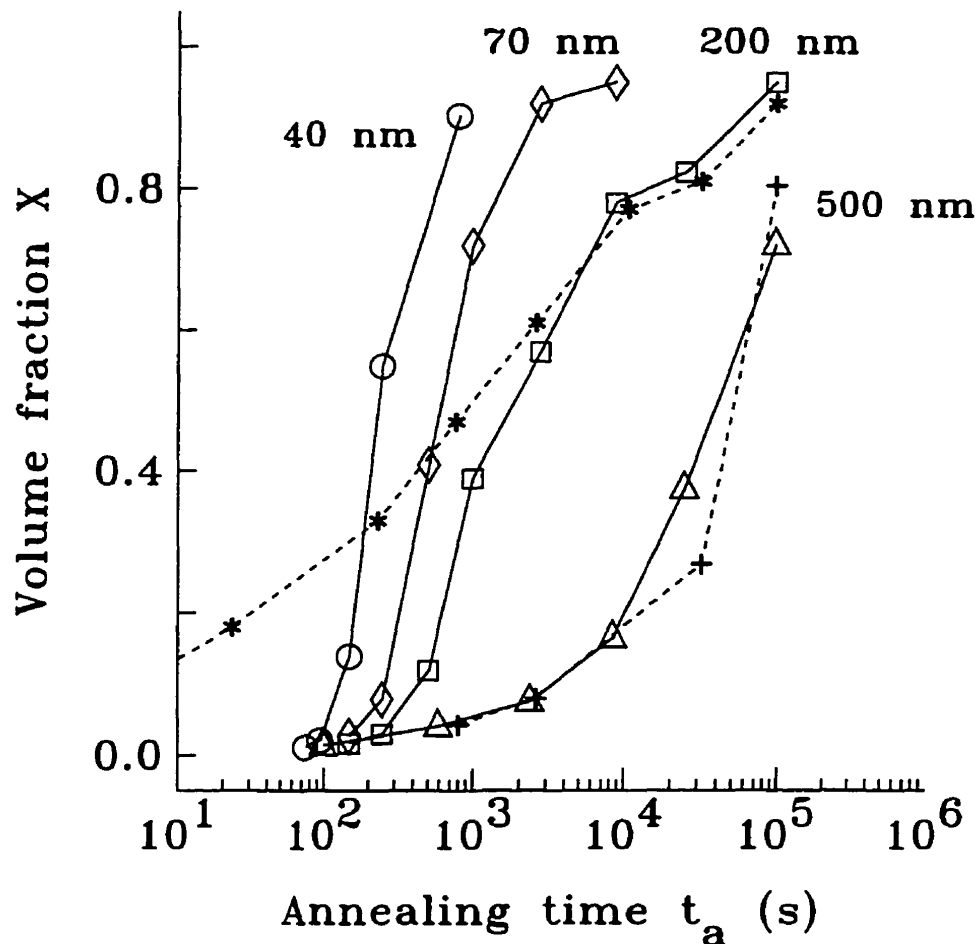


Figure 5.17: Evolution of transformed $\text{Sm}_2\text{Fe}_{14}\text{C}$ volume fraction, X , with annealing ($800\text{ }^\circ\text{C}$) time, t_a , for various $\text{Sm}_2\text{Fe}_{17}\text{C}_{1.0}$ carbides prepared by both ball milling (BM) and melt spinning (MS): \circ 9 h BM, \diamond 3 h BM, \square 1 h BM, \triangle 20 min BM, $*$ 30 m/s MS and $+$ 7 m/s MS. The corresponding grain sizes are indicated in the figure varying between 40 nm and 500 nm.

volume fraction by the well known Johnson-Mehl-Avrami (JMA) equation[158, 159]

$$X(t) = 1 - \exp[-K_T(t - \tau)^n] \quad (5.17)$$

where τ is the effective time lag or incubation time necessary for obtaining a population of critical-size nuclei¹, the constant n is the Avrami exponent and K_T is a temperature-dependent value affected by the transformation kinetics. The Avrami exponent n is characteristic of the transformation process and, therefore, is very important to the present study.

JMA equation is valid for a “discontinuous” transformation (also known as a heterogeneous transformation), namely, the transformation product ($\text{Sm}_2\text{Fe}_{14}\text{C}+3\text{Fe}$)

¹For the definition see the discussion section that follows

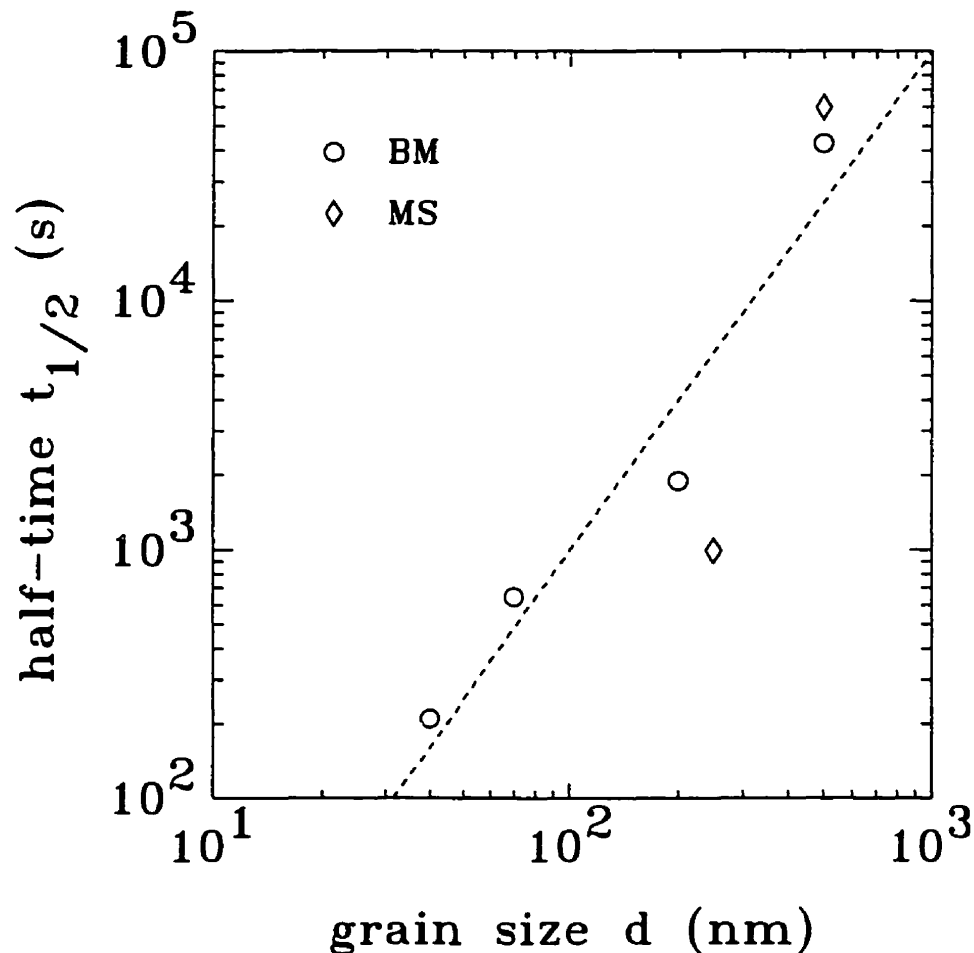


Figure 5.18: Annealing time required to reach $X=0.5$ as a function of the grain sizes in the various samples prepared by ball milling (BM) and melt spinning (MS). The dashed line illustrates the linear least-squares fit.

nucleates and grows and has the same average composition as the untransformed material ($\text{Sm}_2\text{Fe}_{17}\text{C}_{1.0}$) except for a short distance from the advancing interface. The Avrami exponent n is dependent on the nucleation rate and the type of growth process and can be determined from the slope of $\ln \ln(1/(1-X))$ vs $\ln(t-\tau)$ (the Avrami plot) in the isothermal transformation. From the data in Fig. 5.17, the Avrami plots for the samples of various grain sizes are constructed and shown in Fig. 5.19. The resulting Avrami exponents, obtained for $X \leq 0.4$ ¹ are listed in Table 5.4.

¹In the case of the transformation involving nucleation the JMA equation, hence the Avrami plot, is in principle only valid to describe the phase transformation at an early stage[160] for $X < 0.5$ because the model used in deriving the JMA equation neglects the decrease in the actual volume for nucleation during the transformation.

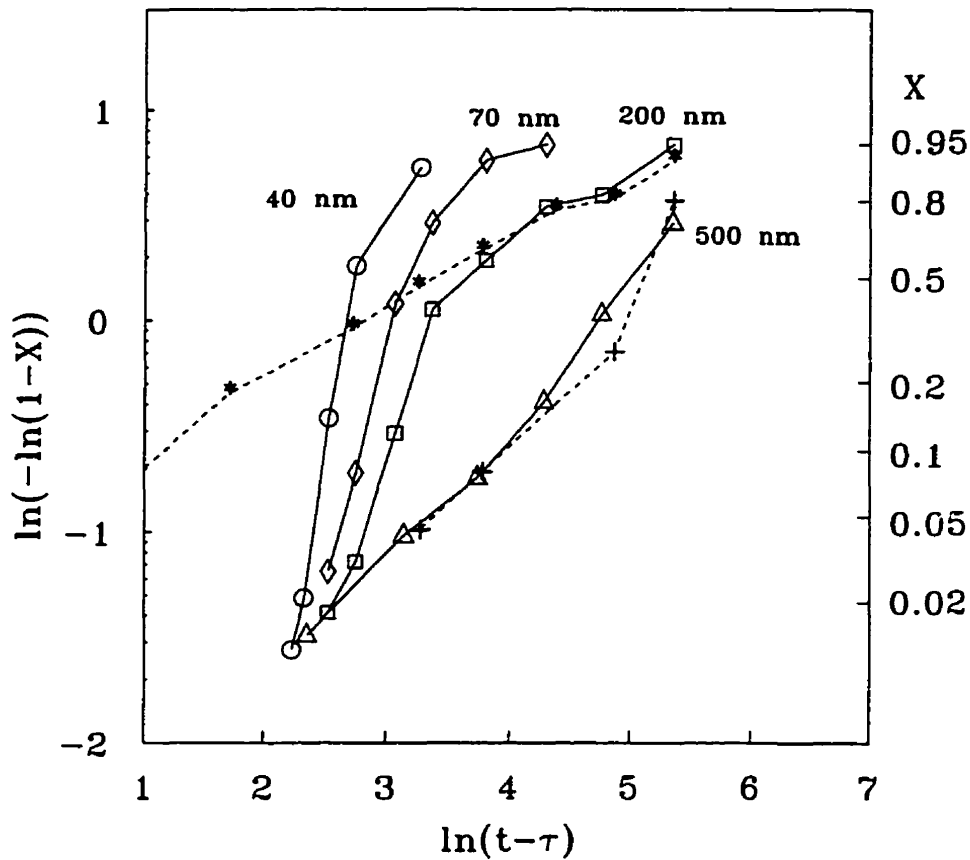


Figure 5.19: Avrami plots constructed from the data in Fig. 5.17 samples of various grain sizes. The isothermal annealing was at 800 °C. Samples were prepared by either ball milling, BM, or melt spinning, MS (see Table 5.4): ○ 9 h BM, ◇ 3 h BM, □ 1 h BM, △ 20 min BM, * 30 m/s MS and + 7 m/s MS. The corresponding grain sizes are indicated in the figure varying between 40 nm and 500 nm.

To construct the Avrami plot the incubation time (as defined in Eq. 5.17) must be determined first. In the present study, the incubation time is determined by the onset time that the transformed product $\text{Sm}_2\text{Fe}_{14}\text{C}$ appears in the TMA scan (sensitivity $\sim 1\%$). There is an uncertainty of 30 s in the determination of the incubation time resulting from the uncertainty in the time required for the sample to be in equilibrium with the furnace (see Fig. 5.15). The uncertainty results in an error in the Avrami exponent. Fast transformations have a relatively short incubation time. For example the 40 nm-grain sample has an incubation time of about 30 s which is the same as the uncertainty. As a result, the error in the Avrami exponent can be large as can be seen in Table 5.4. The transformation rate can be slowed down by decreasing the annealing temperature. For example, after annealing at 700 C for 1 h, the transformed

Table 5.4: A list of the Avrami exponent, n , determined from the Avrami plot in Fig. 5.19 for $X \leq 0.4$

	ball milling process				melt-spinning process	
	9 h	3 h	1 h	20 min	30 m/s	7 m/s
grain size	40 nm	70 nm	200 nm	500 nm	200-300 nm	500 nm
n	3.0 ± 1.0	2.1 ± 0.6	1.8 ± 0.4	0.7 ± 0.1^a	0.4 ± 0.1	0.6 ± 0.2

^aFor $X > 0.2$.

be seen in Table 5.4. The transformation rate can be slowed down by decreasing the annealing temperature. For example, after annealing at 700 C for 1 h, the transformed volume fraction X in the 40 nm-grain sample is 20%; and hence the incubation time may be determined more accurately than at 800 C. However at 700 C the other samples of larger grains have much slower transformation rates; hence the study of the transformation at this temperature is not practical. In fact, one of the reasons for carrying out the present study at 800 C is that at this temperature all the samples, with grain sizes varying between 40 nm and 500 nm, have suitable transformation rates and manageable incubation times¹.

Regarding the Avrami exponent, n , Christian[161] has summarized that, when $n > 1.5$, the nucleation process is present in the transformation and the nucleation rates are higher for larger n . Therefore for the samples ball milled for longer than 1 h, the nucleation rate increases with the milling time (see Table 5.4). Moreover, when $n < 1$ the effective dimensionality of space for the transformation is less than three and the transformation is the growth of the existing nuclei[161]. Therefore, for the large grain samples, namely the short-time (20 min) milled powders and the melt-spun ribbons, the transformation is the growth of a small amount of existing

¹Another reason for choosing 800 C is that this temperature is commonly used for hot deformation processing in the production of permanent magnets as discussed in Section 5.5.3.

$\text{Sm}_2\text{Fe}_{14}\text{C}$ without nucleation in a dimensionality lower than three.

5.5.3 Discussion

In the above section, the grain size dependence of the volume transformation kinetics has been characterized, the half-times of the transformation and the Avrami exponents being significantly affected by the grain size of the parent phase, $\text{Sm}_2\text{Fe}_{17}\text{C}_{1.0}$.

The present method of measuring the transformation volume fraction in quenched samples is not the usual method for studies of isothermal transformation kinetics. Ideally the kinetics should be studied in-situ. The frequently used in-situ methods include DSC, electric resistance and TMA. However all these methods are not suitable for the present study. The temperature for a significant transformation rate is beyond the operating temperature of the DSC setup and is also higher than the Curie temperatures of the samples and, therefore, there is no magnetization at these high temperatures for the TMA measurements. The quality of the present data is lower than those obtained by in-situ methods because there is an error of 10% in each measurement while the relative error in the in-situ data is usually much smaller. In addition, with the present method it is difficult to obtain large number of data points, resulting in a relatively poor statistics¹. However, the present results are still informative for the understanding of the feature of the transformation as discussed below.

Intuitively, the enhancement in the transformation by the reduction of grain sizes should be related to the increase in the fraction of grain boundaries.

In a polycrystalline material, nucleation or the initiation of a phase transformation is assumed to occur on grain boundaries[162, 163, 161] because the nucleus, a small region of transformed product, is relatively easy to form. For the nucleus, there is a critical size, r_c , beyond which a nucleus is stable[161]. This critical size is expressed as

$$r_c = 2\sigma/\Delta g, \quad (5.18)$$

where σ is the effective surface free energy associated with the interfaces around the

¹A set of samples for each Avrami plot must be identical, which is usually from one batch of samples prepared in one process. However, one batch of samples is only valid for 10-20 measurements.

nucleus and Δg is the specific free energy difference (known as the driving force) between the final and initial phases.

The critical size may be very large for the $\text{Sm}_2\text{Fe}_{17}\text{C}_{1.0} \rightarrow \text{Sm}_2\text{Fe}_{14}\text{C}$ transformation because it has a very small driving force. It can be calculated, from Eq. 5.13 obtained in Chapter 5, that the free energy difference ΔG is 0.38 kJ/g-atom at 800 C, a value about one order of magnitude smaller than a typical transformation process, such as the crystallization of amorphous materials. Assuming the effective surface free energy is $\sim 0.1 \text{ J/m}^2$, a typical value for metals and alloys, the critical size is 4 nm as calculated from Eq. 5.18. The simultaneous atomic rearrangement by thermal fluctuations to create such a nucleus larger than the critical size is very unlikely to happen in a perfect crystal. Therefore the catalysing of a nucleation process must depend on a reduction in the effective surface energy and, hence, in the critical size to form a nucleus. This can happen on the grain boundaries: the formation of an embryo involves the destruction of part of an existing surface, the free energy of which helps to provide the free energy needed for the new surface.

For the phase transformation with the nucleation on grain boundaries, Cahn[163] predicted a relationship between the half-time of transformation, $t_{1/2}$, and grain size, d , as¹

$$t_{1/2} = Ad^\gamma \quad (5.19)$$

where A is a constant depending on the nucleation and growth rate and the power, γ , is the characteristic of the type of the nucleation sites². The number of the available nucleation sites for the corresponding sites, N , is related to the scaling factor, γ , through the expression

$$N = Bd^{-4\gamma} \quad (5.20)$$

where d is the average grain size and B is a constant depending on the type of the sites and the shapes of the grains.

¹To my knowledge, there has been no experimental investigation of this relationship.

²There are many different type of sites on grain boundaries. Cahn[163] considered three different types of nucleation sites on grain boundaries and derived the corresponding γ values. They are (1) boundary surfaces (junctions of 2 grains) corresponding to $\gamma=1/4$, (2) the grain edges (junctions of 3 grains), $\gamma=1/2$ and (3) the grain corners (junctions of 4 grains), $\gamma=3/4$.

From Fig. 5.18 and Eq. 5.16, it has been found that $\gamma=2.0\pm 0.5$. According to Eq. 5.20 the number of the available nucleation sites is therefore proportional to d^{-8} . The nucleation sites decrease extremely fast with increasing grain size. For the well crystallized $\text{Sm}_2\text{Fe}_{17}\text{C}_{1.0}$ of 50 μm grains, which is prepared by annealing at 1100 C for 5 h, there may be effectively no nucleation sites for the transformation to initiate. Therefore, phase transformation does not occur in such samples, as confirmed by the corresponding experiments.

The population of nucleation sites decreases with increasing γ . For example, the number of the nucleation sites on the grain boundary surfaces (proportional to the total area per unit volume) is proportional to d^{-1} , the number of the nucleation sites on the grain edges (proportional to the total length per unit volume) is proportional to d^{-2} and the number of the nucleation sites on the grain corners is proportional to d^{-3} . For the present phase transformation, the large γ , corresponding to the site number proportional to d^{-8} , implies that the nucleation occurs in very rare sites. Due to the small driving force, the nucleation may only occur on particular grain boundaries of high free energy, such as high angle grain boundaries, unrelaxed grain boundaries produced by coalescence of particles (cold welding) in ball milling or by rapid quench in melt spinning. The number of those type of nucleation sites may drop very rapidly with increasing grain sizes.

The present results may provide a useful information for the processing of fine grain $\text{Sm}_2\text{Fe}_{17}\text{C}_{1.0}$ alloys over its metastable temperature range. Phase transformation of $\text{Sm}_2\text{Fe}_{17}\text{C}_{1.0} \rightarrow \text{Sm}_2\text{Fe}_{14}\text{C}$ requires an incubation time to accumulate an appreciable amount of transformation nuclei. Therefore within the incubation time the $\text{Sm}_2\text{Fe}_{17}\text{C}_{1.0}$ may be considered as stable. The hot deformation of mechanically alloyed powders[135] or melt-spun ribbons[164] between 700 C and 800 C has been used to successfully produce $\text{Nd}_2\text{Fe}_{14}\text{B}$ -type magnets with good grain alignment. Hot deformation process usually only lasts from a few seconds to a few minutes. This process may be therefore applied to the $\text{Sm}_2\text{Fe}_{17}\text{C}_{1.0}$ alloys. For example, we have found that, at 800 C, the incubation time of the 500 nm grain samples is 500 s. Moreover, our study suggests that the decrease in the free energy difference between $\text{Sm}_2\text{Fe}_{17}\text{C}_{1.0}$ and $\text{Sm}_2\text{Fe}_{14}\text{C}$ by substitution of certain elements, such as Ga, may make the nucle-

ation of $\text{Sm}_2\text{Fe}_{14}\text{C}$ more difficult, and hence may increase the incubation time¹.

¹The substitution of large amount of Ga for Fe turns the $\text{Sm}_2\text{Fe}_{17}\text{C}_{1.0}$ into a stable phase over the whole temperature range[145]. However, the substitution leads to a remarkable decrease in the magnetization (see the discussion on page 102).

CONCLUSION

In this thesis, phase formation in iron-rich binary R-Fe and ternary Sm-Fe-C systems and the structural stability of the interstitial carbides $\text{Sm}_2\text{Fe}_{17}\text{C}_x$ have been studied by using x-ray diffraction, thermomagnetometry and differential scanning calorimetry. The following conclusions can be drawn for the evaluation of the potential of the carbide for permanent magnet production.

- There is a critical carbon concentration, x_c , for a stable $\text{Sm}_2\text{Fe}_{17}\text{C}_x$ structure. When $x > x_c$, $\text{Sm}_2\text{Fe}_{17}\text{C}_x$ is metastable; the equilibrium state is the mixture of $\text{Sm}_2\text{Fe}_{17}\text{C}_{x_c}$, $\text{Sm}_2\text{Fe}_{14}\text{C}$ and $\alpha\text{-Fe}$. The temperature dependence of x_c can be well described using a free energy diagram in terms of a pseudo-binary system of $\text{Sm}_2\text{Fe}_{17}$ and C. Because $\text{Sm}_2\text{Fe}_{14}\text{C}$ and $\alpha\text{-Fe}$ are both soft magnetic phases, they must be avoided during permanent magnet production. Therefore sintering of the carbide powder must be processed over the stable temperature range.
- $\text{Sm}_2\text{Fe}_{17}\text{C}_{0.5}$ and $\text{Sm}_2\text{Fe}_{17}\text{C}_{1.0}$ is stable above 950 C and 1020 C, respectively¹. These temperature ranges are suitable for the sintering process.
- $\text{Sm}_2\text{Fe}_{17}\text{C}_{1.0}$ is a high temperature phase and metastable below 1020 C. Nevertheless the formation of $\text{Sm}_2\text{Fe}_{17}\text{C}_{1.0}$ is kinetically favored over the low temperature phase $\text{Sm}_2\text{Fe}_{14}\text{C}$. As a result of the competition between the kinetically favored and the thermodynamically favored phases, phase formation below 1020 C is very sensitive to the detail conditions of heat treatment. $\text{Sm}_2\text{Fe}_{17}\text{C}_{1.0}$ may be formed below 1020 C if conditions are right. It can be synthesized by low temperature (below 1020 C) annealing of mechanically alloyed or melt spun

¹ $\text{Sm}_2\text{Fe}_{17}\text{C}_x$ of $x=0.5-1.0$ has the suitable magnetic anisotropy to produce magnets with good grain alignment by the sintering process.

precursor, which contains a mixture of metastable phases including the amorphous phase. These results are useful for the preparation of $\text{Sm}_2\text{Fe}_{17}$ carbide with high magnetization by mechanical alloying and melt spinning¹ because the present study has demonstrated that the $\text{Sm}_2\text{Fe}_{17}\text{C}_{1.0}$ structure can be formed below 1020 C without an addition of a structure stabilizer. The addition of a structure stabilizer, such as Ga, reduces the magnetization of the carbide.

- A striking effect of the grain sizes on the stability of the $\text{Sm}_2\text{Fe}_{17}\text{C}_{1.0}$ is, for the first time, revealed by the present study. Although it is metastable below 1020 C, the $\text{Sm}_2\text{Fe}_{17}\text{C}_{1.0}$ compound of 50–100 μm grains is apparently stable over the whole temperature region *even below* 1020 C. However, if the grain sizes are reduced the phase transformation to $\text{Sm}_2\text{Fe}_{14}\text{C}$ then occurs. The smaller the grains the faster the transformation. The transformation rate is generally slow possibly due to the difficulty in nucleating $\text{Sm}_2\text{Fe}_{14}\text{C}$. This slow transformation may permit the hot deformation of $\text{Sm}_2\text{Fe}_{17}\text{C}_{1.0}$, a process usually performed between 700–800 C for a short time to generate good grain alignment in the material.

Other important research accomplishments are:

- Phase formation studies of the mechanically alloyed R_2Fe_{17} and the subsequently annealed samples have established that Sm behaves like a heavy rare earth element in the R-Fe system although it belongs to the first half of the rare earth series. This result is useful for the development of the R-Fe based compounds for new permanent magnet materials.
- A first conclusive work was done on the formation of rare earth high pressure phases (*fcc*) by high energy ball milling, suggesting the effective pressure in the ball mill is above 4.5 GPa. Many rare earth interstitial compounds, such as rare earth oxide, nitride and carbide, are derivatives of this high pressure phase.

¹A phase crystallized from mechanically alloyed or melt spun precursors is in a nanocrystalline form. This is a favorable microstructure for a permanent magnet material.

- Crystallization behavior and kinetics of amorphous Sm-Fe in the mechanically alloyed powders is significantly different from melt spun ribbons, suggesting that the two type of specimens may have different short range orders.
- Disordered R_2Fe_{17} compounds exist through the whole rare earth family as they can be synthesized by low temperature (600-800 C) annealing of the corresponding mechanically alloyed powders. The disorder in the 2-17 structure significantly increases the Curie temperature by as much as 17% (or 70 C). The disorder also changes the lattice constant ratio c/a . A relationship between the extent of the disorder, the Curie temperature and the lattice constant ratio is established.
- The formation of Pr_2Fe_{17} and Nd_2Fe_{17} is associated with an endothermic process, probably resulting from the positive enthalpy of mixing of Pr and Nd with Fe.
- Ball milling is very effective in grain refinement and thus useful to produce highly coercive magnetic powders based on Sm_2Fe_{17} .

The following subjects are suggested for future work:

- The formation of Pr_2Fe_{17} and Nd_2Fe_{17} from mechanically alloyed powders is accompanied by a pronounced endothermic peak. The physical process associated with this endothermic peak was not investigated in this study. Considering that solid state phase transformation is mostly exothermic, it is therefore very interesting to study the details of the phase transformation around the temperatures where the endotherm occurs.
- Crystallization behavior of Sm-Fe amorphous phase prepared by mechanical alloying is significantly different from that by melt spinning. It is therefore necessary to elucidate the origin of this difference. Preparation of completely amorphous samples by the two methods at the same composition is suggested. Structural and thermal analysis on those samples would be helpful for understanding of the difference.

-
- For further work on the stability of the $\text{Sm}_2\text{Fe}_{17}$ carbide, two subjects are suggested. The first is the study of the grain size dependence of the transformation kinetics. The present study was very preliminary. A better method to follow the transformed volume fraction is needed in order to improve the quality of the data so that the Avrami exponent could be determined with a better accuracy. TEM observations are necessary to determine the nucleation sites. The second subject is the enhancement of the stability by the addition of a small amount of structural stabilizer, such as Ga, Si and Al. This is necessary for a further assessment of the potential of the carbide for permanent magnet production.

APPENDICES

A.1 Carbon solubility in $\text{Sm}_2\text{Fe}_{17}\text{C}_x$

From Fig. 5.13 we have

$$\Delta G_{bd} = (1 - x_c) \frac{\partial \Delta G_{2-17-C_x}}{\partial x} \Big|_{x=x_c} \quad (\text{A.1})$$

Based on Eq. 5.8 and Eq. 5.9,

$$\begin{aligned} \frac{\partial \Delta G_{2-17-C_x}}{\partial x} \Big|_{x=x_c} &= H_C - T \frac{dS^c(x)}{dx} \\ &= H_C - RT \ln \frac{x_m - x}{x} \end{aligned} \quad (\text{A.2})$$

Whereas,

$$\begin{aligned} \Delta G_{bd} &= \Delta G_{cd} + \Delta G_{bc} \\ &= (\Delta G_{2-14-1} - \Delta G_{2-17-C_x} \Big|_{x=x_c}) \\ &= (\Delta H_{2-14-1} - \Delta H_C) - T(S_{2-14-1} - S^c(x_c)) - \Delta G_{2-17}, \end{aligned} \quad (\text{A.3})$$

where ΔG_{2-14-1} , ΔH_{2-14-1} and S_{2-14-1} are the free energy, formation enthalpy and entropy, respectively, of the $\text{Sm}_2\text{Fe}_{14}\text{C}$ phase.

Substitution of Eq. A.2 and Eq. A.3 for Eq. A.1 yields

$$\begin{aligned} &RT \left(x_m \ln \frac{x_m}{x_m - x_c} + \ln \frac{x_m - x_c}{x_c} \right) \\ &= TS_{2-14-1} - (\Delta H_{2-14-1} - H_C) + \Delta G_{2-17} \\ &= (\Delta G_{2-14-1} - \Delta G_{2-17-C_x} \Big|_{x=1}) + TS^c(1) \\ &= -\Delta G^{DF} + TS^c(1), \end{aligned} \quad (\text{A.4})$$

where $\Delta G^{DF} = -\Delta G_{bc}$ is the drive force for the phase transformation from the HTP $\text{Sm}_2\text{Fe}_{17}\text{C}_{1.0}$ to the LTP $\text{Sm}_2\text{Fe}_{14}\text{C}$. We define two quantities, $\Delta H'$ and $\Delta S'$ as

$$\Delta G_{2-14-1} - \Delta G_{2-17-C_x} \Big|_{x=1} = \Delta H' - T\Delta S' \quad (\text{A.5})$$

Eq.A.4 can thus be rewritten as

$$\begin{aligned} \chi &= \left(x_m \ln \frac{x_m}{x_m - x_c} + \ln \frac{x_m - x_c}{x_c} \right) \\ &= \frac{[\Delta S' + S^c(1)]}{R} - \frac{\Delta H'}{R} \frac{1}{T}. \end{aligned} \quad (\text{A.6})$$

The above equation is the exact form of Eq. 5.10. Moreover,

$$\Delta S'' = \Delta S' + S^c(1) = S_{2-14-1} - (S_{2-17-C} - S^c) \quad (\text{A.7})$$

is the entropy different between the 2-14-1 and the $\text{Sm}_2\text{Fe}_{17}\text{C}_{1.0}$ without the contribution from the configurational entropy of the interstitial C atoms.

BIBLIOGRAPHY

- [1] Gorham Advanced Materials Institute. *Industrial Ceramics*, page 171, 1991.
- [2] K. H. J. Buschow. New permanent magnet materials. *Materials Science Reports*, 1:1, 1986.
- [3] K. H. J. Buschow. In E. P. Wohlfarth and K. H. J. Buschow, editors, *Ferromagnetic Materials*, volume 4, page 1. North-Holland, Amsterdam, 1988.
- [4] J. F. Herbst. $R_2Fe_{14}B$ materials: Intrinsic properties and technological aspects. *Rev. Mod. Phys.*, 53:819, 1991.
- [5] K. H. J. Buschow. New developments in hard magnetic materials. *Rep. Prog. Phys.*, 54:1123, 1991.
- [6] K. H. J. Buschow. Rare earth permanent magnets. *J. Magn. Magn. Mater.*, 140:9, 1995.
- [7] K. H. J. Buschow. New permanent magnet materials. *Materials Science Reports*, 1:1, 1977.
- [8] J. M. D. Coey and H. Sun. *J. Magn. Magn. Mater.*, 87:L251, 1990.
- [9] H. Sun, J. M. D. Coey, Y. Otani and D. P. F. Hurley. *J. Phys. CM*, 2:6465, 1990.
- [10] J. M. D. Coey, H. Sun, Y. Otani and D. P. F. Hurley. *J. Magn. Magn. Mater.*, 98:76, 1991.
- [11] K. Kobayashi. Review of research and development of $Sm_2Fe_{17}N_x$ hard magnetic material. *IEEE Translation Journal on Magnetics in Japan*, 8:842, 1993.
- [12] C. Kuhrt, H. Cerva, and L. Schultz. *Appl. Phys. Lett.*, 64:6026, 1994.
- [13] J. M. D. Coey, R. Skomski, and S. Wirth. *IEEE Trans. Magn.*, MAG 28, 1992.
- [14] Chris N. Christodoulou and Takuo Takeshita. Interstitial carbonation of the Sm_2Fe_{17} phase by reaction with hydrocarbons. *J. Alloys and Compounds*, 190:41, 1992.
- [15] M. Katter. *Ph. D. Thesis*, Technische Universitat Wien, 1991.
- [16] James Colin. *Metals Reference Handbook*. Butterworths, London; Boston, 1992.

- [17] X.-P. Zhong, R. J. Radwanski, F. R. de Boer, T. H. Jacobs and K. H. J. Buschow. Magnetic and crystallographic characteristics of rare-earth ternary carbides derived from R_2Fe_{17} compounds. *J. Magn. Magn. Mater.*, 86:333, 1990.
- [18] S. Sugimoto, H. Nakamura, M. Okada, and M. Homma. *12th Int. Workshop on R.E. Magnets and their applications*. Canberra 1992, 1992.
- [19] C. Kuhrt, K. Schnitzke, and L. Schultz. *J. Appl. Phys.*, MMM'92, 73:6026, 1993.
- [20] R. Grössinger, X. C. Kou, T. H. Jacobs and K. H. J. Buschow. The anisotropy of $R_2Fe_{17}C_x$ ($R=Sm$ and Tm). *J. Appl. Phys.*, 69:5596, 1991.
- [21] D. B. de Mooij and K. H. J. Buschow. Formation and magnetic properties of the compounds $R_2Fe_{17}C$. *J. Less-Common Met.*, 142:349, 1988.
- [22] D. T. Cromer and A. C. Larson. *Acta Crystallogr.*, 12:855, 1959.
- [23] H.-S. Li, Suharyana, J. M. Cadogan, G.J. Bowden, J.-M. Xu, S. X. Dou and H. K. Liu. *J. Appl. Phys.*, 75:7120, 1994.
- [24] Neil W. Ashcroft and N. David Mermin. *Solid State Physics*. Saunders College, Philadelphia, 1975.
- [25] K. H. J. Buschow. The crystal structures of the rare earth compounds of the form R_2Ni_{17} , R_2Co_{17} and R_2Fe_{17} . *J. Less-Common Metals*, 11:204, 1966.
- [26] Chris N. Christodoulou and Takuo Takeshita. Preparation, structural and magnetic properties and stability of interstitial Sm_2Fe_{17} -carbonitrohydrides. *J. Alloys and Compounds*, 198:1, 1993.
- [27] O. Isnard, S. Miraglia, J. L. Soubeyroux, D. Fruchart and J. Pannetier. *Phys. Rev. B*, 45:2920, 1992.
- [28] R. M. Ibberson, O. Moze, T. H. Jacobs, and K. H. J. Buschow. *J. Phys., Condens. Matter*, 3:1219, 1991.
- [29] O. Isnard, J. L. Soubeyroux, D. Fruchart, T. H. Jacobs and K. H. J. Buschow. *J. Alloys Comp.*, 186:135, 1992.
- [30] R. B. Helmholtz and K. H. J. Buschow. Crystallographic and magnetic structure of ternary carbides of the type $Nd_2Fe_{17}C_x$. *J. Less-Common Metals*, 155:15, 1985.
- [31] O. Isnard, J. L. Soubeyroux, and D. Fruchart. *J. Less-Common metals*, 162:135, 1990.
- [32] Werner Ostertag and Karl J. Strnat. Rare earth compounds with the A_2B_{17} structure. *Acta Cryst.*, 21:560, 1966.

- [33] Y. Khan. The crystal structures of R_2Co_{17} intermetallic compounds. *Acta Cryst.*, B29:2502, 1973.
- [34] M. Katter, J. Wecker, and L. Schultz. Structural and hard magnetic properties of rapidly solidified Sm-Fe-N. *J. Appl. Phys.*, 70:3188, 1991.
- [35] K. H. J. Buschow and A. S. van der Goot. Composition and crystal structure of hexagonal Cu-rich rare earth-copper compounds. *Acta Cryst.*, B27:1085, 1971.
- [36] R. W. Lee. Magnetic anisotropy of single crystal $HoFe_3$. *J. Appl. Phys.*, 52:2058, 1981.
- [37] J. Wecker, M. Katter, K. Schnitzke and L. Schultz. *J. Appl. Phys.*, 69:5847, 1991.
- [38] M. Katter, J. Wecker, and L. Schultz. *Mat. Sci. Eng.*, A133:154, 1991.
- [39] N. F. Chaban, Yu. B. Kuzma, N. S. Bilonizhko, O. O. Kachmar and N. V. Petriv. *Dopv. Akad. Nauk Ukr. RSR, Ser. A*, No. 10:873, 1979.
- [40] H. H. Stadelmaier, N. A. El-Masry, and S. Cheng. *Mater. Lett.*, 2:169, 1983.
- [41] G. C. Hadjipanayis, R. C. Hazelton, and K. R. Lawless. *Appl. Phys. Lett.*, 43:797, 1983.
- [42] D. Givord, H. S. Li, and J. M. Moreau. Magnetic properties and crystal structure of $Nd_2Fe_{14}B$. *Solid State Commun.*, 50:497, 1984.
- [43] J. F. Herbst, J. J. Croat, F. E. Pinkerton and W. B. Yelon. *Phys. Rev. B*, 29:4176, 1984.
- [44] C. B. Shoemaker, D. P. Shoemaker, and R. Fruchart. *Acta Crystallr.*, C40:1665, 1984.
- [45] J. F. Herbst, R. W. Lee, and F. E. Pinkerton. *Annu. Rev. Mater. Sci.*, 16:467, 1986.
- [46] R. E. Watson, L. H. Bennett, and M. Melamud. *J. Appl. Phys.*, 63:3136, 1988.
- [47] R. Mathon. *Contemp. Phys.*, 32:143, 1991.
- [48] V. A. Gubanov, A. I. Liechtenstein and A. V Postnikov. *Magnetism and the Electronic Structure of Crystals*. Springer, Berlin, 1992.
- [49] J. B. Staunton. *Rep. Prog. Phys.*, 57:1289, 1994.
- [50] R. M. White. *Quantum Theory of Magnetism*. Springer-Verlag, Berlin, 1983.
- [51] C. D. Fuerst, J. F. Herbst, and E. A. Alson. *J. Magn. Magn. Mater.*, 54-57:567, 1986.
- [52] D. Givord and R. Lemaire. *IEEE Trans.*, MAG-10:109, 1974.

- [53] D. H. Martin. *Magnetism in Solids*. THE M.I.T. PRESS, Cambridge, Massachusetts, 1967.
- [54] P. C. M. Gubbens, A. M. van der Kraan, T. H. Jacobs and K. H. J. Buschow. *J. Magn. Magn. Mater.*, 67:255, 1987.
- [55] J. Deportes, B. Kebe, and R. Lemaire. *J. Magn. Magn. Mater.*, 54-57:1089, 1986.
- [56] Hon Sun. *Ph. D. Thesis*, University of Dublin, 1992.
- [57] K. Kobayashi, T. Iriyama, N. Imaoka, T. Suzuki, H. Kato and Y. Nakagawa. *12th Int. Workshop on R.E. Magnets and their applications*. Canberra 1992, 1992.
- [58] M. Katter, J. Wecker, L. Schultz, and R. Grössinger. *J. Magn. Magn. Mater.*, 92:L14, 1990.
- [59] M. Katter, J. Wecker, C. Kuhrt, L. Schultz, and R. Grössinger. *J. Magn. Magn. Mater.*, 117:419, 1992.
- [60] P. A. I. Smith. Recent developments in rare-earth based permanent magnet materials. *Materials Forum*, 16:285, 1992.
- [61] J. P. Gavigan and D. Givord. Intrinsic and extrinsic properties of rare earth-transition metal compounds and the permanent magnets. *J. Magn. Magn. Mater.*, 84:288, 1990.
- [62] G. C. Hadjipanayis and A. Kim. *Appl. Phys. Lett.*, 64:5559, 1988.
- [63] C. Kittel and J. K. Galt. *Solid State Physics*, 3:437, 1956.
- [64] H. Kronmuller, K. D. Durst, S. Hock, and G. Martinek. *J. Phys. (France)*, 49:C8-623, 1988.
- [65] R. K. Mishra. *J. Magn. Magn. Mater.*, 54:450, 1986.
- [66] F. E. Pinkerton and C. D. Fuerst. *J. Magn. Magn. Mater.*, 89:139, 1990.
- [67] J. S. Benjamin. *Matall. Trans.*, 1:2943, 1970.
- [68] C. C. Koch, O. B. Cavin, C. G. McKamey and J. O. Scarbrough. *Appl. Phys. Lett.*, 43:1017, 1983.
- [69] E. Gaffet and J.-P. Gaspard. *J. Phys. France*, 51:C4-205, 1990.
- [70] J. S. C. Jang and C. C. Koch. Amorphization and disordering of the Ni₃Al ordered intermetallic by mechanical milling. *J. Mater. Res.*, 5:498, 1990.
- [71] M. Oehring and R. Bormann. *J. Phys. France*, 51:C4-169, 1990.

- [72] H. J. Fecht. Synthesis and properties of nanocrystalline metals and alloys prepared by mechanically attrition. *NanoStructure Materials*, 1:125, 1992.
- [73] J. Eckert, L. Schultz, and K. Urban. Formation of quasicrystalline and amorphous phases in mechanically alloyed Al-based and Ti-Ni-based alloys. *Acta Metall. Mater.*, 39:1497, 1991.
- [74] J. Eckert, L. Schultz, E. Hellstern and K. Urban. Glass-forming range in mechanically alloyed Ni-Zr and the influence of the milling intensity. *J. Appl. Phys.*, 64:3224, 1988.
- [75] M. L. Trudeau, R. Schulz, D. Dusault and A. Van Neste. *Phys. Rev. Lett.*, 64:99, 1990.
- [76] E. Gaffet. Phase transition induced by ball milling germanium. *Mater. Sci. and Eng. A*, page 161, 1990.
- [77] A. N. Patel and S. Diamond. *Mater. Sci. Eng.*, 98:329, 1988.
- [78] G. B. Schaffer. A nanocrystalline mixture of intermetallic compounds by mechanical alloying. *Scripta Metall.*, 27:1, 1992.
- [79] P. I. Loeff, H. Bakker, and F. R. de Boer. In E. Arzt and L. Schultz, editors, *New Materials by Mechanical Alloying Techniques*, page 119. DGM informationsgesellschaft, Oberursel, 1989.
- [80] A. Calka and J. S. Williams. Synthesis of nitrides by mechanical alloying. *Materials Science Forum*, 88-90:787, 1992.
- [81] M. S. El-Eskandarany, K. Sumiyama, K. Aoki and K. Suzuki. Reactive ball milling for solid state synthesis of metal nitrides powders. *Materials Science Forum*, 88-90:801, 1992.
- [82] G. B. Schaffer and P. G. McCormick. *Appl. Phys. Lett.*, 55:45, 1989.
- [83] J. Ding, W. F. Miao, P. G. McCormick and R. Street. Mechanochemical synthesis of ultrafine Fe powder. *Appl. Phys. Lett.*, 67:3804, 1995.
- [84] C. C. Koch. Mechanical milling and alloying. In *Materials Science and Technology*, volume 15, pages 193-245. VCH, Weiheim, 1993.
- [85] C. C. Harris. On the limit of comminution. *Trans. Soc. Min. Eng.*, 238:17, 1967.
- [86] R. B. Schwarz and W. L. Johnson. *Phys. Rev. Lett.*, 51:415, 1983.
- [87] W. L. Johnson. *Prog. in Mater. Sci.*, 30:81, 1986.
- [88] L. Schultz. *Mater. Sci. Eng.*, 97:15, 1988.

- [89] R. M. Davis, B. McDermott, and C. C. Koch. Mechanical alloying of brittle materials. *Met. Trans.*, 19A:2867, 1988.
- [90] A. E. Ermakov, E. E. Yurchikov, and V. A. Bariono. *Fiz. Metal. Metalloved.*, 52:1184, 1981.
- [91] A. E. Ermakov, V. A. Bariono, and E. E. Yurchikov. *Fiz. Metal. Metalloved.*, 54:935, 1982.
- [92] Y. Seki and W. L. Johnson. Lattice stability of Cu-Ti base intermetallic compounds. In A. H. Clauer and J. J. de Barbadillo, editors, *Solid State Powder Processing*, page 287. The Mineral, Metals and Material Society, Warrendale(PA), 1990.
- [93] D. E. Luzzi and M. Meshii. *J. Less Common Metals*, 140:193, 1988.
- [94] Z. H. Yan, M. Oehring, and R. Bormann. Metastable phase formation in mechanically alloyed and ball milled Ti-Si. *J. Appl. Phys.*, 72:2478, 1992.
- [95] P. A. I. Smith and P. G. McCormick. Phase separation during mechanical milling of $\text{Sm}_2\text{Fe}_{17}$. *Scripta Metallurgica*, 26:485, 1992.
- [96] O. Mao, Z. Altounian, and J. O. Ström-Olsen. A simple method to determine the purity of an inert gas. *Rev. of Sci. Instr.* (*in press*).
- [97] G. K. Wertheim, M. A. Butler, K. W. West, and D. N. E. Buchanan. *Rev. Sci. Instrum.*, 11:1369, 1974.
- [98] A. J. C. Wilson. *X-Ray Optics*. Methuen, London, 1949.
- [99] Harold. P. Klug and Leroy E. Alexander. *X-Ray Diffraction Procedures For Polycrystalline and Amorphous Materials*. Wiley-Interscience publication, New York, 1974.
- [100] B. E. Warren. *X-Ray Diffraction*. Dover, New York, 1990.
- [101] H. E. Kissinger. *Analytical Chemistry*, 29:1702, 1957.
- [102] E. Kneller, Y. Kahn, D. Cheng, and B. Frochte. *Z. Metallkde*, 80:774, 1989.
- [103] K. Schnitzke, L. Schultz, J. Wecker and M. Katter. *Appl. Phys. Lett.*, 57:2853, 1990.
- [104] N. Murillo, J. Gonzalez, F. Cebollada, V. E. Matin, J. M. Gonzalez and L. Schultz. Phase distribution and magnetic properties of mechanically alloyed Sm-Fe. *IEEE Trans. Magn.*, 29:2857, 1992.
- [105] B. Love. *WADD Tech. Rep.*, 61-123:37, 1961.
- [106] F. H. Spedding and B. J. Beaudry. *J. Less Com. Met.*, 25:61, 1971.

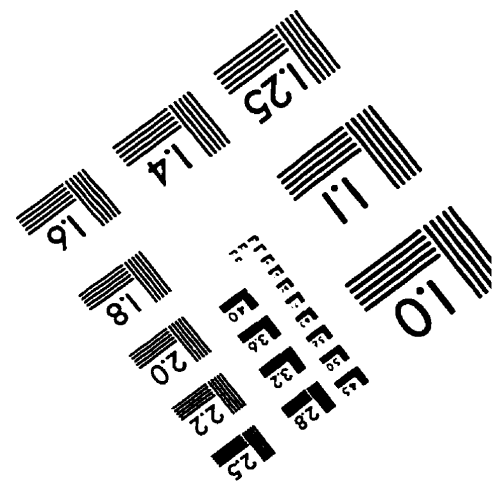
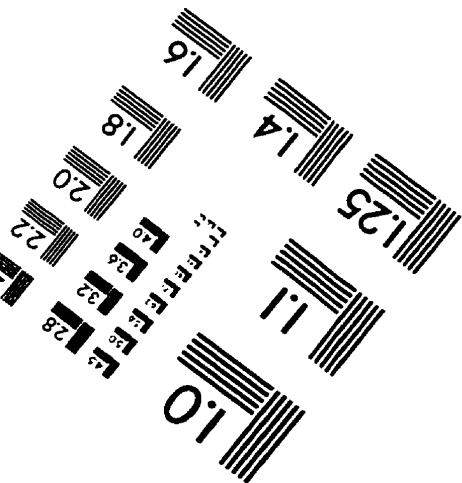
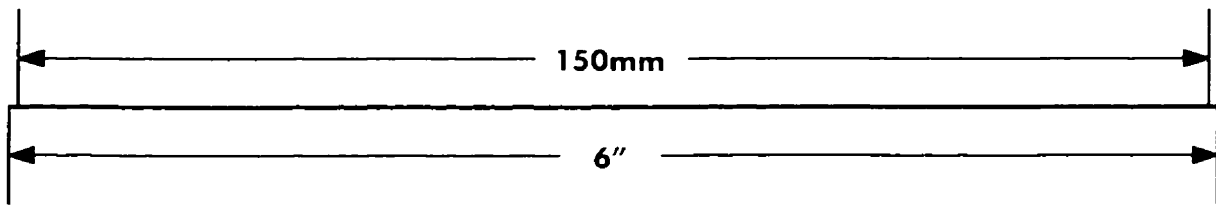
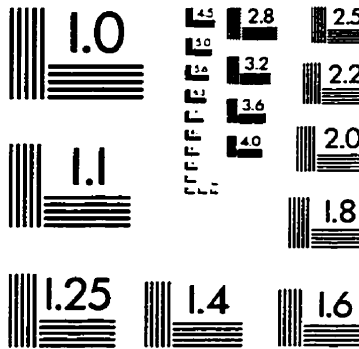
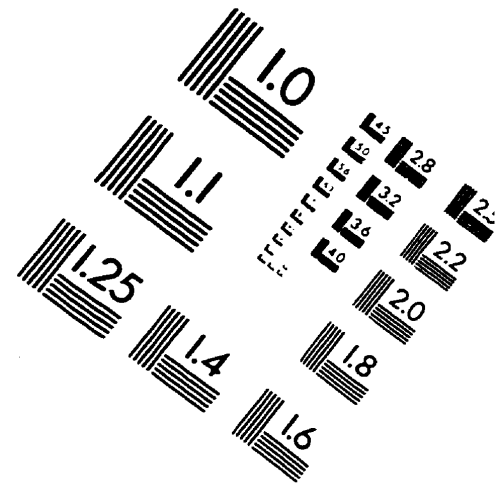
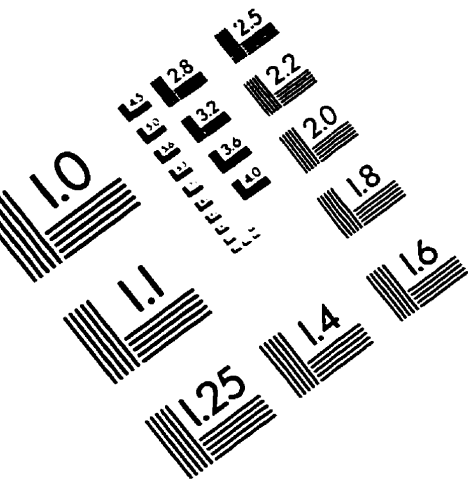
- [107] G. J. Piermaarini and C. E. Weir. *Science*, 144:69, 1964.
- [108] R. Sabet-Sharghi, Z. Altounian, and W. B. Muir. Formation, structure, and crystallization of Al-rich metallic glasses. *J. Appl. Phys.*, 75:4438, 1994.
- [109] T. Alonso, H. Yang, Y. Liu and P. G. McCormick. Demixing of $\text{Nd}_2\text{Fe}_{14}\text{B}$ during mechanical milling. *Appl. Phys. Lett.*, 60:833, 1992.
- [110] H. J. Fecht, E. Hellstern, Z. Fu and W. L. Johnson. Nanocrystalline metals prepared by high-energy ball milling. *Metall. Trans. A*, 21A:2333, 1990.
- [111] Z. Altounian, Tu Guo-Hua, and J. O. Ström-Olsen. Crystallization characteristics of Cu-Zr metallic glasses from $\text{Cu}_{70}\text{Zr}_{30}$ to $\text{Cu}_{25}\text{Zr}_{75}$. *J. Appl. Phys.*, 53:4755, 1982.
- [112] R. M. Ibberson, O. Moze, T. H. Jacobs and K. H. J. Buschow. Neutron diffraction study of lattice changes in $\text{Nd}_2\text{Fe}_{17-x}\text{Si}_x(\text{C}_y)$. *J. Appl. Phys.*, 78:7196, 1995.
- [113] A. Jayaraman. Solid-liquid and solid-solid transformation in the rare-earth metals at high pressures. *Phys. Rev.*, 139:A 690, 1965.
- [114] B. Johansson and A. Rosengren. *Phys. Rev. B*, 11:2836, 1971.
- [115] David R. Lide. *CRC Handbook of Chemistry and Physics*. CRC Press, Boston, 71st edition, 1991.
- [116] R. Ramesh, J. K. Chen, and G. Thomas. *J. Appl. Phys.*, 61:2993, 1987.
- [117] K. A. Gschneidner, Jr. and J. T. Waber. *J. Less Com. Met.*, 6:354, 1964.
- [118] T. L. Felmlee and L. Eyring. *Inorg. Chem.*, 7:660, 1968.
- [119] T. Alonso, Yinong Liu, T. C. Parks, and P. G. McCormick. Correction to 'synthesis of the high pressure fcc phase in lanthanide metals by mechanical milling'. *Scripta Met. Mat.*, 26:1931, 1992.
- [120] T. Alonso, Yinong Liu, T. C. Parks, and P. G. McCormick. synthesis of the high pressure fcc phase in lanthanide metals by mechanical milling. *Scripta Met. Mat.*, 25:1607, 1991.
- [121] D. R. Maurice and T. H. Courtney. *Met. Trans.*, 21A:289, 1990.
- [122] J. S. C. Jang and C. C. Koch. *Scripta Metall. et Mater.*, 24:1599, 1990.
- [123] W. Zhang, G. Liu, and K. Han. The Fe-Y (iron-yttrium) system. *Journal of Phase Equilibria*, 13:304, 1992.
- [124] D. E. Luzzi and M. Meshii. Crystalline to amorphous transition of intermetallic compounds under electron irradiation - a review. *Res Mechanica: International Journal of Structural Mechanics & Materials Science*, 21:207, 1987.

- [125] J. S. C. Jang and C. C. Koch. *J. Mater. Res.*, 5:325, 1990.
- [126] D. E. Luzzi. Journal of alloys and compounds. In D. E. Luzzi, editor, *Symposium on Solid State Amorphizing Transformations*, volume 194, pages 189-461. Elsevier Sequoia SA, Netherlands, 1993.
- [127] Ludwig Schultz. Preparation and properties of mechanically alloyed Nd-Fe-B magnets. In G. J. Long and F. Grandjean, editors, *Supermagnets, Hard Magnetic Materials*, page 573. Kluwer Academic Publishers, Netherlands, 1991.
- [128] T. Miyazaki, Yang Xingbo, K. Takakura, and M. Takahashi. Magnetic properties of rapidly quenched amorphous Fe-Sm alloys. *J. Magn. Magn. Mater.*, 60:211, 1986.
- [129] Chris N. Christodoulou and Takuo Takeshita. Sm₂Fe₁₇-nitride-based permanent magnets produced by rapid solidification. *J. Alloys and Compounds*, 196:1, 1993.
- [130] Z. Altounian, Tu Guo-Hua, and J. O. Ström-Olsen. *J. Appl. Phys.*, 54:3111, 1983.
- [131] R. Brüning, Z. Altounian, J. O. Ström-Olsen and L. Schultz. *Mater. Sci. Eng.*, 97:317, 1988.
- [132] P. Y. Lee and C. C. Koch. *J. Mater. Res.*, 23:2837, 1988.
- [133] Osami Haruyama, Akio Kuroda, and Nobuo Asahi. A comparison of the structure of Ni-Zr amorphous alloys obtained by mechanical alloying and melt spinning. *J. Mater. Res.*, 5:5596, 1990.
- [134] A. K. Niessen, F. R. de Boer, R. Boom, P. F. deChatel, C. W. M. Mattens and R. A. Miedema. *CALPHAD*, 7:51, 1983.
- [135] L. Schultz and J. Wecker. Hard magnetic properties of Nd-Fe-B formed by mechanical alloying and solid state reaction. *Mater. Sci. Eng.*, 99:127, 1988.
- [136] L. Schultz, J. Wecker, and E. Hellstern. *J. Appl. Phys.*, 61:3583, 1987.
- [137] Editor-in-Chief: Thaddeus B. Massalski. *Binary Alloy Phase Diagrams*. William W. Scott, Jr., Ohio, 1986.
- [138] B. G. Shen, L. S. Kong, F. W. Wang and L. Cao. *Appl. Phys. Lett.*, 63:2288, 1993.
- [139] B. G. Shen, F. W. Wang, L. S. Kong, L. Cao and W. S. Zhan. *J. Appl. Phys.*, 75:6253, 1994.
- [140] K. A. Gschneidner, Jr. and F. W. Calderwood. The carbon-rare earth systems. *Bulletin of Alloy Phase Diagrams*, 7:421, 1986.

- [141] F. H. Spedding, K. A. Gschneidner, Jr. and A. H. Daane. The crystal structure of some of the rare-earth carbides. *J. Am. Chem. Soc.*, 80:4499, 1958.
- [142] Hans H. Stadelmaier and Hee Kyun Park. The system iron-gadolinium-carbon and its ternary carbides. *Z. Metallkd*, 72:417, 1981.
- [143] K. H. J. Buschow. Structure and properties of ternary Fe-rich rare earth carbides. In G. J. Long and F. Grandjean, editors, *Supermagnets, Hard Magnetic Materials*, page 527. Kluwer Academic Publishers, Netherlands, 1991.
- [144] Z. H. Cheng, B. G. Shen, F. W. Wang, J. X. Zhang, H. Y. Gong and J. G. Zhao. *J. Phys.: Condens. Matter*, 6:L185, 1994.
- [145] L. Cao, K-H. Müller, A. Handstein, W. Grünberger, V. Neu and L. Schultz. High performance $\text{Sm}_2\text{Fe}_{15}\text{Ga}_2\text{C}_2$ permanent magnets made by mechanical alloying and hot pressing. *J. Phys. D: Appl. Phys.*, 29:271, 1996.
- [146] G. B. Clemente, J. E. Keem, and J. P. Bradley. *J. Appl. Phys.*, 64:5299, 1988.
- [147] R. Coehoorn, D. B. de Mooij, J. P. W. B. Duchateau and K. H. J. Buschow. *J. Phys. C*, 49:669, 1988.
- [148] T. Yoneyama, T. Yamamoto, and T. Hidaka. Magnetic properties of rapidly quenched high remanence Zr added Sm-Fe-N isotropic powders. *Appl. Phys. Lett.*, 67:3197, 1995.
- [149] J. Ding, Y. Liu, R. Street and P. G. McCormick. *J. Appl. Phys.*, 75:1032, 1995.
- [150] E. Girt. *private communication*.
- [151] R. Skomski, C. Murray, S. Brennan and J. M. D. Coey. Interstitial modification of rare-earth intermetallics. *J. Appl. Phys.*, 73:6940, 1993.
- [152] O. Mao, Z. Altounian, J. Yang, and J. O. Ström-Olsen. Thermal stability of nano-structured $\text{Sm}_2\text{Fe}_{17}\text{C}_x$ compounds prepared by ball milling. *J. Appl. Phys.*, 79:5536, 1996.
- [153] O. Mao, Z. Altounian, and J. O. Ström-Olsen. To be published.
- [154] O. Mao, J. O. Ström-Olsen, Z. Altounian, and J. Yang. Solid-state phase transformation in nanocrystalline $\text{R}_2\text{Fe}_{17}\text{C}_x$ compounds (R=Sm or Nd; x=0-1). *IEEE Transactions on Magnetism*, 32:4413, 1996.
- [155] O. Mao, Z. Altounian, J. O. Ström-Olsen, and J. Yang. Characteristics of $\text{Sm}_2\text{Fe}_{17}\text{C}_x$ compounds prepared from ball-milled blends of $\text{Sm}_2\text{Fe}_{17}$ and graphite. *J. Appl. Phys.*, 79:4619, 1996.
- [156] Liu Zhihui. Analysis of temperature-dependent magnetization in Sm-Fe-C compounds using a two-sublattice model. *IEEE Transaction on Magnetism*, 27:3409, 1991.

- [157] F. R. de Boer, Huang Ying-kai, Zhang Zhi-dong, D. B. Nooij and K. H. J. Buschow. Magnetic and crystallographic properties of ternary rare-earth compounds of the type $R_2Fe_{14}C$. *J. Magn. Magn. Mater.*, 72:167, 1988.
- [158] J. Burke. *Kinetics of Phase Transformations in Metals*. Pergamon, Oxford, 1965.
- [159] M. E. Fine. *Introduction to Phase Transformations in Condensed Systems*. Macmillan, London, 1964.
- [160] V. Erukhimovitch and J. Baram. Crystallization kinetics. *Physical Review B*, 50:5854, 1994.
- [161] J. W. Christian. *The Theory of Phase Transformations in Metals and Alloys*. Pergamon, Oxford, 1975.
- [162] W. A. Johnson and R. F. Mehl. *Trans. Amer. Inst. Min. Met. Eng.*, 135:416, 1939.
- [163] John W. Cahn. The kinetics of grain boundary nucleated reaction. *Acta Metallurgica*, 4:1, 1956.
- [164] C. D. Fuerst and E. G. Brewer. Die-upset Nd-Fe-B magnets from blends of dissimilar ribbons. *J. Appl. Phys.*, 76:6232, 1994.

IMAGE EVALUATION TEST TARGET (QA-3)



APPLIED IMAGE, Inc
1653 East Main Street
Rochester, NY 14609 USA
Phone: 716/482-0300
Fax: 716/288-5989

© 1993, Applied Image, Inc., All Rights Reserved